# Direct Coupling Methods for the Analysis of Open & Closed Boundaries Containing Incompressible Fluid and the Applications on Offshore Structures

**Supervisors:** Professor G.E. Hearn

Associate Professor G.D. Weymouth

**Author:** Qufeng Li

22nd April 2022

Engineering and Physical Science

**The University of Southampton**

# Summary

In engineering analysis, a variety of analytical and numerical methods have been developed for analysing the hydrodynamic response of marine vehicles or offshore structures under different sea state, including the multipole expansion & integral equation methods for rigid body analysis and hydroelastic analysis involving elastic deformation. Most of these existing procedures require the specification of the boundary conditions over the wetted surface in advance so that functions of the flow are solvable. For rigid body analysis, each degree of motion is explicit while in hydroelastic analysis, the boundary condition is assignable through modal expansions. When additional free fluids exist the problem is a little more complex, but solvable, since the principle modes for analysis is unchanged with sloshing. However, new challenge arise when an incompressible liquid fills the inside of a structure as the modes are significantly changed due to the restriction of internal volume. The boundary conditions are, therefore, unassignable through normal dry hull analysis. In this dissertation, a different approach is developed with associated software developed by the author.

The only conditions left that controls the motions in these problems will be continuity of normal velocity at the structural surface and the fundamental strain-stress relationship of the materials. These two conditions cannot provide the results directly. However, they enable us to formulate proper force-movement equations that contain the boundary conditions implicitly. In other words, the hydrodynamic forces and the structural response are directly coupled without separating the model into different orders of components.

Direct coupling method itself is not a novel concept. It has been developed for solving simple acoustic and hydroelastic cases. This dissertation focuses on alternative forms, which allow one to solve problems that are more general. The matrix operation technique utilised enables solution of fully closed boundary problems in a boundary element analysis.

The study was initially proposed for analysing the Anaconda wave energy convertor

(WEC) device, which is a highly flexible rubber tube filled with seawater. The device is submerged under the free surface and generates internal propagating bulges waves through the excitation of external ocean waves. Only 1-dimentional equations were initially proposed to solve the behaviour of the structure. The direct coupling method developed in this dissertation is the first study that treats it as a three-dimensional model.

Existing engineering packages and software are not capable to deal with the mathematical problem raised by the closed incompressible fluid domain. Hence, the hydrodynamic codes together with the coupled structural analysis are written and implemented independently. Only few packages related to matrix operation and special mathematical functions are borrowed. The configuration of the model is achieved by command flows under carefully geometric design and the results are exported in raw data to be analysed.

Chapter 1 discusses the engineering significance of the proposed novel method and presents a literature review for both existing fluid mechanic methods and Anaconda WEC. The difficulties for solving fully closed problems and the deductions of important formulations are introduced in Chapter 2. Modelling of different problems are presented in Chapter 3. Chapters 4 & 5 provide verifications of developed method and the solutions of general offshore structure and a fully filled closed structure. Chapter 6 provides analysis of Anaconda solved applying the new method. Some unfinished works and discussions are addressed in Chapter 7.

# Declaration of authorship

I, Qufeng Li declare that this thesis entitled

**Direct Coupling Methods for the Analysis of Open & Closed Boundaries Containing Incompressible Fluid and the Applications on Offshore Structures**

and the work presented in it are my own and has been generated by me as the result of my own original research. I confirm that:

- this work was done wholly or mainly while in candidature for a research degree at this University;
- where any part of this thesis has previously been submitted for a degree or any other qualification at this University or any other institution, this has been clearly stated;
- where I have consulted the published work of others, this is always clearly attributed;
- where I have quoted from the work of others, the source is always given. With the exception of such quotations, this thesis is entirely my own work;
- I have acknowledged all main sources of help;
- where the thesis is based on work done by myself jointly with others, I have made clear exactly what was done by others and what I have contributed myself;

Signed: ……

Date: ……

# Acknowledgement

I should bid my sincere thanks to my main supervisors, Professor G.E. Hearn for inviting to this programme and guiding me throughout these years. I would also bid my appreciation to Associate Professor G.D. Weymouth who took over the supervision when Emeritus Professor G.E. Hearn retired. I’m wordless to describe how much they have inspired and how great they have contributed to this work. I’m more than grateful for their patience and insistence during the COVID-19 pandemic, the hardest time in this programme and in my life.

Qufeng Li

# Contents

# List of Figures

# List of Tables

# Nomenclature

## Latin symbols

| | | |
|---|---|---|
| $\mathbf{A}$ | Transient matrix A | [-] |
| $A_s$ | Cross-sectional area | [$m^2$] |
| $A_w$ | Wave amplitude | [m] |
| $a_1$ | 1st order Rayleigh damping coefficients | [$s^{-1}$] |
| $a_2$ | 2nd order Rayleigh damping coefficients | [s] |
| $a_Y$ | Acceleration at cylinder top | [$m \cdot s^{-2}$] |
| (a, b, c) | Cartesian coordinates of source point | [-] |
| $\mathbf{B}$ | Transient matrix B | [-] |
| C | Constant | [-] |
| $c_b$ | Bulge wave velocity | [$m \cdot s^{-1}$] |
| $\mathbf{C_g}$ | Generalised fluid damping matrix | [-] |
| $\mathbf{c_g}$ | Generalised structural damping matrix | [-] |
| $C_W$ | Capture width | [m] |
| $c_w$ | Incident wave velocity | [$m \cdot s^{-1}$] |
| D | Distensibility | [$m \cdot s^2/kg$] |
| $\mathbf{D}$ | Dynamic stiffness matrix | [-] |
| d | Diameter | [m] |
| E | Elastic Young's modulus | [$kg \cdot m^{-1} \cdot s^{-2}$] |
| $\mathbf{f}$ | Transient hydrodynamic matrix | [-] |
| $\mathbf{f_s}$ | Transient hydrostatic matrix | [-] |
| G | Green function | [-] |
| $G_r$ | Regular part of Green function | [-] |
| g | Gravitational acceleration | [$m \cdot s^{-2}$] |
| $H_s$ | Structural height | [m] |
| h | Water depth | [m] |
| $h_0$ | Difference between internal and external free surface | [m] |
| i | Pure imaginary number ($i^2 = -1$) | [-] |
| J | Moment of inertia | [$kg \cdot m^2$] |
| $\mathbf{K_g}$ | Generalised fluid restoring matrix | [-] |
| $\mathbf{k_g}$ | Generalised stiffness matrix | [-] |
| $\mathbf{L}$ | Transient dynamic matrix | [-] |
| $L_0$ | Tube length | [m] |
| M | Mass | [kg] |

| | | |
|---|---|---|
| $\mathbf{M_g}$ | Generalised added inertia matrix | [-] |
| $\mathbf{m_g}$ | Generalised mass matrix | [-] |
| $\mathbf{n}$ | Normal vector | [-] |
| p | Pressure | $[kg \cdot m^{-1} \cdot s^{-2}]$ |
| $\vec{p}$ | Column vector of elemental pressure | [-] |
| $p_E$ | External pressure | $[kg \cdot m^{-1} \cdot s^{-2}]$ |
| $p_I$ | Internal pressure | $[kg \cdot m^{-1} \cdot s^{-2}]$ |
| R | Projected horizontal distance | [m] |
| $R_s$ | Structural radius | [m] |
| r | Distance in 3-dimensional space | [m] |
| $r_2$ | Distance related to image source | [m] |
| t | Time | [s] |
| T | Wave period | [s] |
| $\mathbf{T_I}$ | Transient internal dynamic matric | [-] |
| $t_s$ | Shell thickness | [m] |
| $t_w$ | Wall thickness | [m] |
| $\vec{u}$ | Column vector of generalised elemental displacement | [-] |
| $u_x$ | Horizontal velocities associated with incident wave | $[ms^{-1}]$ |
| $u_z$ | Vertical velocities associated with incident wave | $[ms^{-1}]$ |
| $\vec{v}$ | Column vector of elemental normal velocity | [-] |
| x | X-direction coordinate | [m] |
| y | Y-direction coordinate | [m] |
| Z | Impedance | $[kg \cdot m^{-4} \cdot s^{-1}]$ |
| z | Z-direction coordinate | [m] |

## Greek symbols

| | | |
|---|---|---|
| $\alpha$ | Phase shift angle | [-] |
| $\alpha_n$ | Area of the $n^{th}$ boundary element | $[m^2]$ |
| $\beta$ | Hysteresis coefficient | [s] |
| $\boldsymbol{\gamma}$ | Velocity on surface | $[m \cdot s^{-1}]$ |
| $\delta$ | Non-dimensionalised deflection | [-] |
| $\varepsilon$ | Non-dimensionalised shell stiffness | [-] |
| $\zeta_n$ | Damping coefficient of the $n^{th}$ mode | [-] |
| $\boldsymbol{\zeta}$ | Principal coordinate vector | [-] |
| H | Time-dependent wave profile | [m] |
| $\eta$ | Time-independent wave profile | [m] |
| $\theta$ | Zenith angle | [-] |

| | | |
|---|---|---|
| $\boldsymbol{\lambda}$ | Wavelength | [m] |
| $\boldsymbol{\Xi}$ | Generalised wave excitation vector | [-] |
| $\mu$ | Poisson ratio | [-] |
| $\nu$ | Wave number | [$s^{-1}$] |
| $\xi_z$ | Heave response | [m] |
| $\Pi$ | Energy flux (power) | [$kg \cdot m^2 \cdot s^{-3}$] |
| $\Pi_W$ | Energy flux of a propagating wave per meter width | [$kg \cdot m \cdot s^{-3}$] |
| $\pi$ | Mathematical constant | [-] |
| $\rho$ | Density | [$kg \cdot m^{-3}$] |
| $\rho_s$ | Structural density | [$kg \cdot m^{-3}$] |
| $\rho_w$ | Fluid density | [$kg \cdot m^{-3}$] |
| $\Phi$ | Time-dependent flow potential | [-] |
| $\phi$ | Time-independent flow potential | [-] |
| $\phi_A$ | Incident wave potential | [-] |
| $\varphi$ | Azimuth angle | [-] |
| $\omega$ | System frequency | [$s^{-1}$] |
| $\omega_1$ | $1^{st}$ order natural beam frequency | [$s^{-1}$] |
| $\omega_e$ | Encounter wave frequency | [$s^{-1}$] |

## Abbreviations & Acronyms

| | |
|---|---|
| BEA | Boundary Element Analysis |
| CFD | Computational Fluid Dynamic |
| DHI | Danish Hydraulic Institute |
| FEA | Finite Element Analysis |
| FSI | Fluid-Structure Interaction |
| PTO | Power Take-Off |
| WEC | Wave Energy Convertor |
| VLFS | Very Large Floating Structure |

## Subscripts

| | |
|---|---|
| FS, W, S & R | Free, wetted, seabed & radiation surfaces |
| I, E | Internal and external quantities |
| i, j or k & m, n | Boundary element identifiers |

# 1. Engineering Background

This chapter discusses the engineering significance of the proposed novel analysis method by reviewing the history of fluid-structure interaction (FSI) modelling. The need for analysing hydrodynamic behaviour and its coupled structural behaviour increases as more novel and excessively large structures emerge in Ship Science, Offshore Engineering and other practical activities related to hydrodynamic loads.

Existing studies of FSI problems are abundant and highly developed for common engineering application. However, the particular kind of devices studied in this work arise due to its rare demand and existing technological limitations. The amount of experience we can directly refer to are few. It is shown in later chapters that the correlation between the proposed novel method and widely applied hydroelastic analysis is too weak. So the fundamental equations have to be established anew from first principles.

The main consideration of this chapter is not only to appreciate the tremendous works undertaken by previous researchers, but also to try and 'figure out' the special merit of the suggested method studied. This is a primary study of a novel marine structure. Many more in-depth investigations are yet to be undertaken and cannot be included in this thesis. The novel technique is not developed enough to cope with all future-sophisticated engineering scenario. As with existing techniques, maturity of a procedure requires time and effort. A review is needed to direct the further research.

To avoid digression, however, the focus will be on studies highly related to the numerical analysis of linear elastic models. Being the most applied method, the hydroelastic method is addressed together with the few existing published studies of direct coupling methods. Research of the Anaconda wave energy convertor is appropriate to the engineering application of this study. The development of Green function introduces the mathematical background of free-surface hydrodynamic analysis.

## 1.1 Review of Fluid-Structure Interaction Problems

Early water wave-structure interaction studies treat the structures as rigid bodies and primarily investigate their kinematic response and dynamic loads. The problems are categorised as the manoeuvring and seakeeping of free-floating bodies. Manoeuvring refers to analysing the induced hydrodynamic response of a structure moving in calm water. Seakeeping determines the response to a ship encountering incident waves. As ships and offshore platforms becomes increasing larger, the need for analysing internal structural strain and stress arises to facilitate better design. Studies considering the structure deformation is usually called strength analysis.

### 1.1.1 Rigid Body Analysis

For stationary structures, viscous effects and associated boundary layer development is the primary interest in resistance studies, whereas in FSI, hydrodynamic force induced by the acceleration of flow potential is equivalently important. Assuming an incompressible and irrotational fluid flow means interactions with a rigid body can be determined by solving the Laplace equation with proper boundary conditions. So-called harmonic functions satisfy the Laplace equation and the fluid flow solution is usually a summation or transformation of certain fundamental solutions. Continuity of normal velocity is applied on the wetted surface for stationary or moving bodies.

In special cases with idealised body shape, the flow potential and its resulting hydrodynamic distribution can be determined analytically. McCamy & Fuchs [1] solve the diffraction field of a vertical cylinder in regular propagating wave with an infinite series of cylindrical harmonics. The origin of each cylindrical harmonic term is located at the centroid of the cylinder and is singular through the associated second kind Bessel functions. However, the result converges everywhere in the flow domain since the singularity occurs inside the rigid boundary.

Dean [2] provided a two-dimensional model for the diffraction over a submerged horizontal cylinder through a semi-analytical method. The result suggests zero reflection over a fully submerged cylinder under a beam-sea condition, confirmed by Ursell & Dean [3] applying another analytical approach.

Sources of varies orders (such as a sink or a dipole) are classic tool for the simulation of potential flow, as they are harmonic and bounded everywhere in space except at the origins. The mathematical essence of the fluid singularities are the spherical harmonics solved, appealing to the Laplace equation, through the method of separation of variables. One can add additional harmonic terms to satisfy boundary conditions for more general use.

For models under sinusoidal excitation and oscillating periodically about an initial equilibrium state, the sources pulsate at the constant frequency of an incident wave. Again, one can determine the proper hydrodynamic solution from a series of pulsating sources of different magnitude, phase shifts and origin subject to satisfaction of continuity of normal velocity on the wetted surface. According to the summary of Ogilvie [4] this method can be further divided into two distinctive approaches, that is, the multipole expansion method and the integral equation method.

Multipole expansions consider the fluid solution to be a uniformly converged through superposition of wave potentials that satisfy the Laplace equation and other boundary conditions in the external fluid. This method, proposed by Ursell [5] in 1949, solved a 2-dimensional heaving oscillation of a circular cylinder. It was stream function based rather than expressed in terms of potential functions. For a defined motion like heaving, the streamline on the boundary can be determined explicitly and the stream function of external fluid is assumed to be a superposition of infinite orders of multipole sources of magnitudes determined to satisfy normal velocity at a selected number of points on the cylinder boundary. The final result is derived as a collocation problem.

Further research by Ursell [6] extended this method to a rolling ellipse. Tasai [7] extended the method to bodies of arbitrary shape, such as the analysis of ship model 2D sections. The technique was studied by Havelock [8] for 3-dimensional problems. The hydrodynamic force on a sphere was obtained by Hulme [9] & Wang [10] for the floating and submerged conditions.

Rather than place sources inside the body, Frank [11] proposed the procedure of distributing sources on the body wetted-surface and solving the simultaneous sets of integral equations formulated according to the locations of sources. The controlling

equation for this method is usually the second identity of Green, as the external fluid potential satisfies the Laplace equation. The numerical solution is obtain by partitioning the wetted surface into panels. The results by Chen [12] coincide well with those derived through the multipole expansion method. The detailed mathematical formulation of this method will be introduced in Chapter 2.

The coupled response of an inertia-dominated rigid body starts from an equilibrium state, and requires one to determine the hydrodynamic forces for different degrees of freedom, specified a priori, from using the aforementioned procedure. In the linearized dynamic motion equation, inertial reactive forces induced by unit acceleration and velocity for different degrees of motion are assembled and represented as added mass and fluid damping matrices. A structural mass matrix and stiffness matrix arising from buoyancy considerations are combined with the fluid reactive matrices to form the coupled dynamic equations and these are directly solved in the frequency domain. The detailed process for archiving such dynamic relationship are presented in many fundamental works [13, 14]. Results given by Newman [13] suggest heaving resonance occurs for a floating structure when the incident wave frequency is close to the natural oscillating frequency. Such example is introduced and compared in Chapter 4 for verification of the novel method.

### 1.1.2 Flexible Structure Analysis

Precise solutions for general fluid-structure interaction problems require the analysis of Navier-Stokes equation (or Euler equation for inviscid flow), which is usually a time domain analysis difficult to manipulate. However, for engineering application, one can usually simplify the dynamic model into linearized frequency domain analysis when the system is under sinusoidal excitation. This is especially true for wave-body interaction problems studied here.

According to the coupling steps between fluid and structure, the analysis procedure can be distinguished as a monolithic approach and a partitioned approach [15]. The former approach treats the fluid and structure dynamic as a holistic and single system. The solutions are solved simultaneously under a unified mathematical framework. The interfacial conditions are included implicitly in the solution procedure, so data transfer

is not required across the interface. Contrarily, the partitioned approach computes fluid and structure dynamics in separate fields. Thus requiring interfacial communication with proper boundary conditions to obtain physical solutions under different algorithm frameworks.

Generally, monolithic approaches may achieve better accuracy due to closely coupled formulation. However, the corresponding code may be more specialised, requiring more resources to develop and maintain. In contrast, modelling problems with a partitioned approach may take less expertise coding, but requires careful modification on the interface for consistency of the physics. The directly coupled method developed here, together with widely applied hydroelastic analysis, are typical monolithic approaches. The dynamics are formulated under a single force-displacement equation. Codes developed for this study are independent of any other existing engineering software or package, including hydroelastic analysis tools.

Most nonlinear analysis for fluid-structure interaction problems apply the generalised Gauss-Seidel approach [16], where the dynamic response of fluid and structure are calculated sequentially in the time domain. Computational fluid dynamics (CFD) is introduced for such generalised nonlinear problems. Extensional problems involving sloshing and structural acoustics were presented by Morand & Ohayon [17] with linear simplifications. Dowell & Hall [18] presented in-depth discussions for modelling nonlinear fluid-structure interaction problems under multidisciplinary conditions. Reduced-order models, based on computational fluid dynamical methods, are specifically addressed in this study. Numerical works focused on ocean engineering are given by Chakrabarti [19], covering a wide range of linear & nonlinear offshore structures.

The well-known hydroelastic theory was proposed in 1950s [20]. It recognised the fact that marine structures, including ships, barges and platforms were becoming ‘flexible’ in engineering practice with the growth of their scale. The particular terminology was proposed by Heller & Abramson [21], indicating hydroelasticity is a naval counterpart to aeroelasticity and recognises that a significant difference exist between hydrodynamic, inertia and elastic stress for a floating marine structure interacting with

external loads at 'hydro' level [22].

For most linear hydroelastic theories, the structural responses to wave excitation are expressed as a summation of distortions in the principal modes of the structural vibration in vacuum. Each mode of distortion, together with its corresponding natural frequency, can be determined through dry hull analysis, in the absence of any external actions. The fluid is inviscid and incompressible in the hydrodynamic analysis. The amplitude of excitation is assumed small.

Upon selecting the necessary order of modes (normally $n \leq 6$), the dynamic equation of a floating or travelling beam like structure can be written as,

$$[\mathbf{M_g} + \mathbf{m_g}]\ddot{\boldsymbol{\zeta}} + [\mathbf{C_g} + \mathbf{c_g}]\dot{\boldsymbol{\zeta}} + [\mathbf{K_g} + \mathbf{k_g}]\boldsymbol{\zeta} = \boldsymbol{\Xi} \tag{1.1.1}$$

In Equation 1.1.1, $\mathbf{m_g}$, $\mathbf{c_g}$ and $\mathbf{k_g}$ denote the n × n generalised mass, structural damping and stiffness matrices. Normally, $\mathbf{m_g}$ and $\mathbf{k_g}$ are obtained through dry hull analysis, with the structure considered to vibrate in vacuum as a free-free beam. The structure is usually treated as a non-uniform Timoshenko beam in 2-dimensional analysis or modelled with finite element analysis in 3-dimensional cases. $\mathbf{M_g}$, $\mathbf{C_g}$ and $\mathbf{K_g}$ are the n × n generalised added mass, fluid damping, and fluid restoring matrices respectively. $\boldsymbol{\Xi}$ denotes the n × 1 generalised wave excitation vector, containing both incident and diffraction wave contributions. The determination of these terms requires the procedure of wet hull analysis, where the simplified beam in 2-dimensional analysis is divided into a number of strips to subsequently obtain their hydrodynamic coefficients and hydrodynamic loads. For 3-dimensional model, the hydrodynamic coefficients are determined through the pulsating source method introduced in the previous section with the defined principal modes already obtained. Principal coordinate vector $\boldsymbol{\zeta}$ is solved to provide the modes amplitude, which has the form,

$$\zeta(t) = \zeta \exp(-i\omega_e t) \tag{1.1.2}$$

where $\omega_e$ is the encounter wave frequency. The solution of structural response and stress can be determined linearly by summing all principal solution together multiplied by the derived modal amplitude.

This system of motion equations is unified in the sense that it allows the analysis for

both rigid-body motions (heave & pitch) and distortions that are coupled through the effects of the fluid actions. However, it should be noted that symmetric (in vertical plane) and anti-symmetric motions should be calculated separately within a two-dimensional analysis.

Early 2-dimensional hydroelastic was recognised in 1970s through the work of Bishop & Price [23]. The physical accuracy of fluid-structure interaction modelling was significantly improved. Analysis of antisymmetric and asymmetric distortion were enabled within the assumption of 2-dimensional potential analysis through later works [24, 25]. Further researches by Belik & Price [26] and Belik et al. [27] provided the means of evaluating global wave-induced load caused by transient bottom impact (slamming) through a convolution integral technique under regular or irregular wave conditions. Comparisons of available full-scale engineering examples, like tankers, bulk carriers and container ship were carried out by Bishop et al. [28] and Aksu et al. [29] with the application of 2-dimensional hydroelastic theory.

To meet the application requirement of non-beamlike marine structures and multi-hulled vessels, a 3-dimensional form of unified hydroelastic theory was developed in 1980s by Bishop [30]. Detailed evaluation on response of local configurations is enabled through 3-dimentional finite element modelling. This improvement provided the numerical access to manifold type of engineering applications, such as the transportation of dry dock and jack-up rigs [31, 32]. Further advancement by Du et al [33] introduced translating pulsating source distributions over the mean wetted surface of a ship hull for better wet hull analysis. Ergin & Temarel [34] investigated a partially filled cylindrical container with a boundary integral method and the method of images to include internal free surface boundary conditions within the analysis of 3-dimensional modal analysis. Large amounts of recent hydroelastic research has focused on very large floating structures (VLFS) [35] with engineering application to floating airports with extensive progress emerged. Wu et al [36] proposed a double composite singularity distribution method, taking advantage of symmetry conditions. Bai et al [37] applied a subdomain approach in the fluid analysis for investigating a floating runway located in a half-confined harbour.

Nonlinearity of the hydroelastic problems are also of special consideration when structures experience large motion at sea. Jensen [38] developed a nonlinear quadratic strip theory in the frequency domain for predicting wave loads and ship responses in moderate seas. Wu et al. [39] formulated the generalized second order hydrodynamic forces for 3-dimensional modelling. Chen et al [40] investigated a moored plate with both large structural deflection and nonlinear time-dependent exciting wave load.

Detailed review for hydroelastic analysis in ship science and offshore engineer can be referred from the work of Chen et al [41].

Software and packages developed from either CFD or hydroelastic analysis are abundant, including widely used ANSYS FLUENT & CFX, Flow 3D, Star CCM+ and Open FOAM. G-Hydroflex, which is the prototype of a web-enabled software developed by Harding et al [42], is also available for one to utilise the grid-based computational resources for modelling interaction between fluid and flexible structures.

Among all currently available tools, only a CFD based procedure is potentially able to solve the hydrodynamic behaviour of an incompressible flow within a fully closed domain. The mathematical problem, which occurs in frequency domain analysis, is not noticed in existing research. To solve such problem, and avoid the expensiveness of CFD modelling, an independent code with a novel algorithm is necessary.

### 1.1.3 Existing Direct Coupling Methods

Direct coupling methods was first proposed in the acoustic field [43 – 45] in 1970s and developed independently by Kim et al [46, 47] for 3-dimensional offshore engineering study.

Early acoustic analysis considers the structure to be fully closed and vibrating at high frequency. Finite shell elements and the interpolation of acoustic load are of high order in the modelling. In contrast, the first direct coupling work by Kim [46] investigated an opened floating ship free from any internal load. The next study [47] applies liquid cargo inside the ship, however, still opened with free surface. The models are subjected to normal wave frequency and the element interpolation is of unit order. Finite Element Analysis (FEA) is applied here for internal fluid analysis, which is relatively cumbersome for a directly coupled method.

The major difference for acoustic analysis is that the fluid is compressible. The Green function, or pulsating source, introduced here satisfies the linear acoustic function. Compressibility would actually facilitate the formulation of direct coupling mathematically; however, we cannot apply such procedure for studying an incompressible fluid due to the non-uniqueness issue discussed later.

Generally, the method treats the overall structural response as an unknown and constructs its relationship with external periodical loading through FEA. Unknown components of loading induced by structural motion are in turn presented as a linear function of the overall response through Boundary Element Analysis (BEA). One can, thereafter, solve the only unknown with only one equation. Unlike hydroelastic analysis, with only a few modal amplitude to be solved, the response on each elemental node are the unknowns in the WEC problem. The realisation of this method, therefore, requires massive computational power to deal with matrices of thousands by thousands. This has become is feasible in the last decade with the progress of hardware and algorithms.

## 1.2 Anaconda Wave Energy Device

Figure 1.1 An imaginary impression of Anaconda wave energy convertor (provided by Checkmate SeaEnergy Ltd [48])

The Anaconda wave energy converter concept was first put forward by Professor R.C.T. Rainey and Professor F.J.C. Farley in 2005. It is a device completely dependent upon the distensibility of a tube made of a highly elastic and flexible material such as rubber.

Figure 1.1 provides an artist's impression of an Anaconda working under sea conditions.

The numerical method to be adopted for solving the highly flexible Anaconda-like structure is a rather innovative concept, therefore, few directly pertinent references on its numerical analysis can be cited from previous published research. However, several experiments have been recently conducted on pressurised rubber tube models, therefore, we will focus on the experimental analysis in this section.

### 1.2.1 Principles of Operation

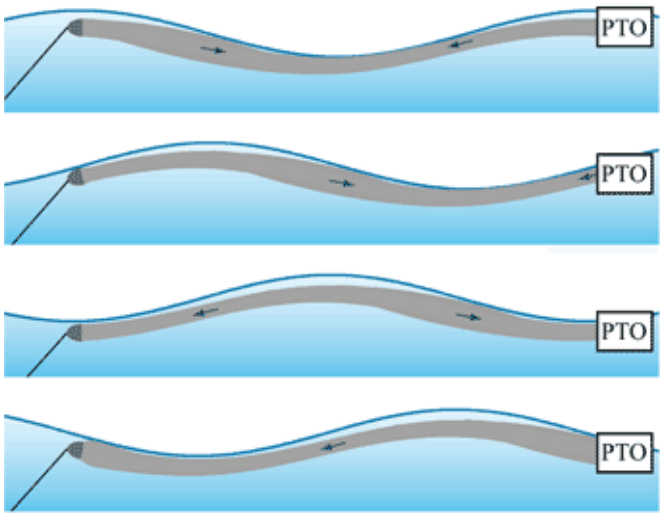


Figure 1.2 Principle of bulge wave generation when the wave is travelling from left to right. Arrows indicate the direction of the oscillatory internal flow [48]

Briefly speaking, Anaconda is a long rubber tube located perpendicularly to the propagating incident wave and floats just beneath the sea free surface. The body of the tube is pressurised with internal sea water, sealed at either end and anchored to the seabed. The variation of pressure along the length of the structure will squeeze or enlarge the size of the tube, resulting in a running bulge wave inside the distensible body. The bulges carry high pressure fluid and will continuously do work to the generator in the power take off (PTO) system if we rectify the flow by adding a pair of one-way valves. The sketch in Figure 1.2 illustrates the four phases of bulge wave along with the shape of water profile.

Normally, the bulge wave travels at a speed determined by the dimension of the tube

and the properties of the material. According to the linear theory proposed by Green and quoted in Lighthill's book [49], when the tube is considered to be uniform with negligible losses from hysteresis, the bulge wave velocity $c_b$ is a function of fluid density ρ and tube distensibility D, namely,

$$c_b = \sqrt{\frac{1}{\rho D}} \tag{1.2.1}$$

The distensibility represents the increase rate of tube cross-sectional area $A_s$ per unit excess pressure p, that is,

$$D = \frac{1}{A_s}\frac{\partial A_s}{\partial p} \tag{1.2.2}$$

If the thickness of tube wall $t_w$ is small, distensibility can be approximately determined from Young's modulus E, tube diameter d and $t_w$ from,

$$D = \frac{d}{E t_w} \tag{1.2.3}$$

More generally, when hysteresis β (stress analogous to structural damping) is considered, one can determine the of 1-dimentional bulge wave equation,

$$\frac{\partial^2 p_I}{\partial t^2} - \beta\frac{\partial^3 p_I}{\partial t^3} = \frac{1}{D\rho}\frac{\partial^2}{\partial x^2}(p_I + p_E) \tag{1.2.4}$$

Where subscript I & E refer to the internal bulge pressure and external excitation pressure. Most of the existing numerical analysis of Anaconda are based on this equation.

The determination of free bulge wave speed is essential for the design of Anaconda since the power generation reaches its maximum when the bulge wave speed is close to the external incident wave speed. Theoretically, under resonance conditions, the amplitude of the bulge wave grows linearly along the tube while the energy transported by the bulge grows as the square of the distance [50]. Off resonance, the bulge behaves analogous to a forced oscillation. It travels at the speed of external wave, however, it does not grow continuously along the tube, which may, therefore, lead to an undesirable power output [51].

According to the study of Chaplin et al. [52], the fluid motion inside the tube can be

separated into three distinct bulge wave components. One following with the same speed and direction of the external water wave with a + 90° phase shift relative to the maximum pressure, the other two travelling towards either ends of the tube at its free bulge wave speed. The backward-travelling bulge wave is a result of structural property and, sometimes, reflection of the rigid stern. However, it is much smaller in comparison to the other wave.

### 1.2.2 Experimental Testing

Several tests have been conducted on the scaled-down rubber tube in order to verify the theory of bulge wave in still water or under the excitation of an external wave. All of them suggest good agreements when the tube is straight and horizontal.

The very first experiment undertaken by Farley & Rainey [51] verified the progressive growth of the bulge wave along the structure. A rubber tube of 12 cm in diameter and 2.2 m in length was tested with manometers implemented at each end. Under waves of 1 cm amplitude and 2.0 s period, the stern experienced pressure amplification 5 times larger than measured pressure at the bow. Further testing showed that the pressure was even doubled by reflection when the stern end was closed. The results were extrapolated to suggest 1 MW power extraction for a single Anaconda of 7 m diameter and of length 150 m subject to North Sea wave conditions.

The following research by Heller et al. [53], in 2010, at the Danish Hydraulic Institute (DHI), assigned an ad hoc PTO system to the 1:25 scaled model with each end of the tube being attached to fixed box-like containers (see Figure 1.3). This experiment aimed to provide well defined initial and boundary conditions for numerical simulations and to compare the measured data with theoretical predictions. The results verified the Lighthill's theory [49] that the measured bulge wave speed agreed well with the prediction of Equation 1.2.1, both in still water and under external wave excitation. The DHI experiment also captured the radiated wave field of the model and suggested a feature of distribution that enhanced the energy capture efficiency.

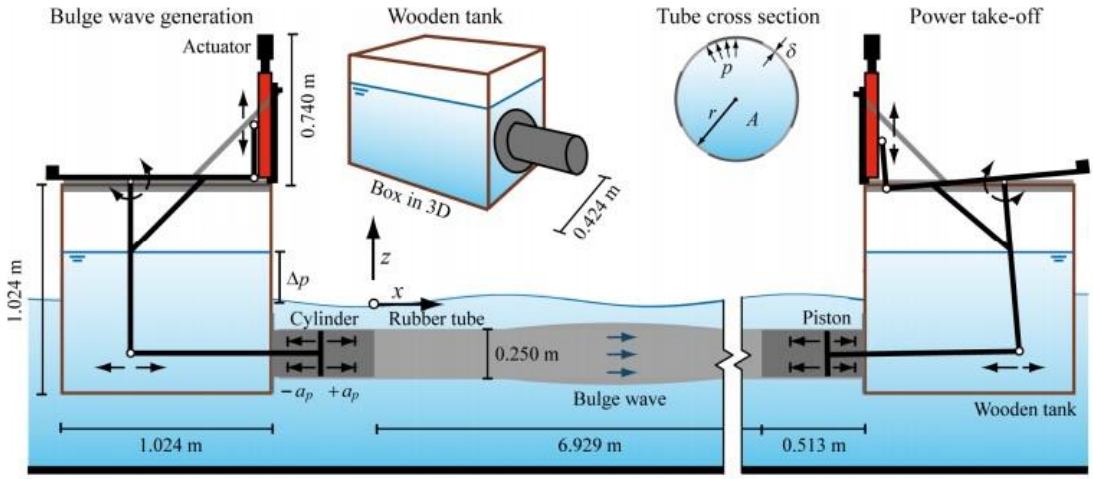


Figure 1.3 Test set-up of DHI testing. The bulge waves were generated artificially by piston in still water or by external wave excitation. The level of still water in the wooden boxes was filled higher than the external wave profile in order to pressurise the tube [53].

A more comprehensive research was conducted by Chaplin et al [52] (2011), trying to study the influence of PTO system. The set-up of this experiment was similar with DHI, however, the tube bow was no longer linked to still water. As is shown in Figure 1.4, bulge waves are totally induced by external waves and will lead to a pneumatic oscillation in the vertical rigid tube attached at the stern. The power generated is interpreted as a change of the air column pressure whilst PTO impedance is controlled by a series of parallel capillary tubes.

This result, again, verified the theoretical prediction both for the behaviour of material and bulge wave, including the decay of progressive bulge waves when external wave frequency was not at system resonant frequency. It is concluded that a higher impedance of the PTO will lead to high pressure flux into the PTO and low amplitude bulge motion. A resulting change in the measured energy extraction is also estimated in this study.

All experiments previously discussed suggest a high power take off efficiency, from a capture width of 3 tube diameters to 6 tube diameters when working under resonance. However, no research has ever focused on the full scaled model or relevant electric generator. Like most of wave energy convertors, the preliminary designs [54] suggests that Anaconda will smooth the oscillating flow through a pair of high and low pressure

accumulators to deliver steady high pressure flux to the turbine.

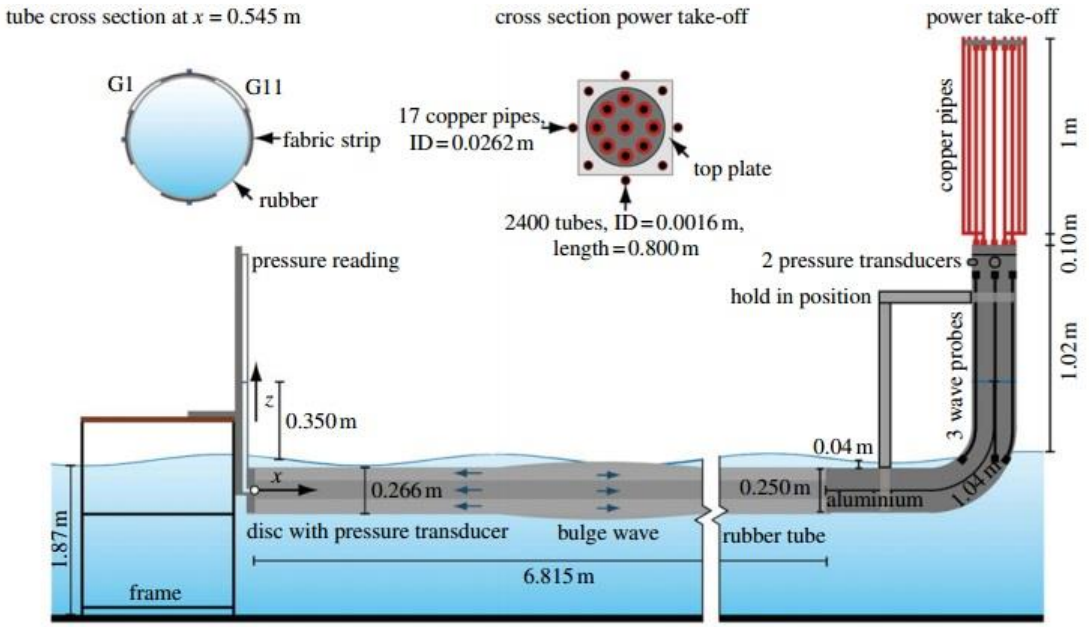


Figure 1.4 The experimental arrangement of Chaplin's research. The bulge wave from left to right will result in an oscillation of air column in the rigid tube. While the impedance of PTO system is controlled by the number of opening capillary pipes [52].

An outstanding problem is that none of the reported research really seek to simulate the motion of Anaconda under a free or anchored condition, since the tube is forced to be straight and horizontal in the wave tank. Bending of the tube is not simulated and the influence of longitudinal tension is not included.

### 1.2.3 Numerical Analysis

Few researchers have tried to analyse Anaconda in a numerical way, however, their models cannot solve the problem completely or deal only with the structural problem.

Linear analysis of the rubber tube is summarised in the work of Farley [55], where the analytical deduction of the bulge wave behaviour is presented. The PTO system is modelled with impedance Z defined by,

$$Z = \frac{\rho c_b}{A_s} \tag{1.2.5}$$

which represents the total resistance of the bulge fluid per unit flux.

A nonlinear numerical model was investigated by Mei [56] with friction force considered. The results verify the evolution of harmonic amplitude bulge waves and predict the maximum available energy flux as a function of the tube length and other structural parameters. However, the controlling functions in his model are one-dimensional partial derivative equations that describe the unforced propagating waves along a straight tube, which means bending and heaving motion of the structure is neglected and the asymmetry around the circular cross-section is not considered. The diffraction effect is also not taken into consideration in the study and the excitation force in the model is highly simplified.

Another numerical analysis by Bucchi & Hearn [57] is focused on aneurysm, which is a phenomenon for flexible tubes swelling asymmetrically out of its centreline, leading to the reduction of energy transmission or even structural failure. By applying FEA method, they concluded that aneurysm can be effectively prevented if inextensible reinforcement material is combined with the rubber tube in the form of external longitudinal strips. More studies on structural response of Anaconda are also given in their papers [58, 59].

Except the stationary studies (ref. [57 – 59]), all the dynamic analysis of the rubber tube models are 1-dimensional. Longitudinal effects of the tube is neglected and the pressure acting over the circumference is assumed to be same. This is obviously nonphysical since the wave pressure is distributed exponentially along the depth. The method developed here is able to generate a more comprehensive result.

## 1.3 Green Function Formulation

Green functions are the key mathematical tool to be used in our method, therefore, many related papers are reviewed for understanding the essence of this function. Alternative expressions of the free surface dependent Green function are also studied for the implementation of our computational programme.

The concept of a Green function is not very recondite and we can find its detail in almost every textbook introducing elliptic partial differential equations [60]. The function provides an analytic solution of the Laplace equation or Poison equation

through the theorems of Green. For 3-dimensional problems, the function always consist of a principal solution term, 1/r, added to a harmonic function determined from the boundary conditions of the problem. In a free surface wave study, such as expression happens to be the same as a free surface multipole source of the lowest order.

As we are in fact solving a problem with a Neumann boundary condition for the wave-body interaction study, the application of a Green function in this numerical method is slightly different from its original definition. A full explanation of the adopted approach is explained in Chapter 2.

The original expressions of free surface Green functions can be found in the summary of Wehausen & Laitone [61]. However, their mathematical expressions are not quite applicable for engineering use as they involve infinite range integration over wave number with a singular integrand. To make the calculation regular enough for computer operations, Hearn [62] derived a mathematically equivalent expression involving only a finite integration range and Newman [63, 64] modifies the function into a series of expansions. Another numerical evaluation by Noblesse [65] suggests a separation of the Green function and only the near-field component contains the singularity that needs modification.

Beside constant oscillation, the Green function has been developed in the time domain for analysing transient motions [64]. Alternative mathematical expressions are given by Newman [66] for channel problems.

# 2 Methodology

## 2.1 Fluid Theories

### 2.1.1 Basic Assumptions & Definitions

The amplitudes of the water wave and body boundary oscillation are assumed to be relatively small compare to the wavelength ($A_w/\lambda < 1/7$), hence, Stokes effect under this model is negligibly small and the overall solution will be a linear superposition of incident, diffraction and radiation wave potentials. The fluid is considered to be inviscid, incompressible and subjected to irrotational flow so simple potential theory is to be addressed. Meanwhile, the whole model is assumed to be in a steady state, which means the motion has already converged to a harmonic oscillation with constant amplitude and period, hence, we can analyse the problem in the frequency domain.

Consequently, the fluid can be characterised by a summation of incident, diffraction and radiation flow potential, each the form,

$$\Phi(x, y, z, t) = \phi(x, y, z)\exp(-i\omega t) \tag{2.1.1}$$

Lower-case $\phi$ denotes the time independent velocity potential, $\omega$ the incident wave frequency and the negative sign in the exponential term indicates the direction of propagating wave. For example, if the wave is travelling along the positive direction of x, the phase function inside the exponential term should be in a form of,

$$\exp[i(\nu x - \omega t)] \tag{2.1.2}$$

Here $\nu$ is the wave number. We take the sign of the frequency term as negative in this study to keep the position term positive.

The fluid is only bounded by the free surface at z = 0 ($S_F$) and an impermeable uniform horizontal seabed located at z = -h ($S_B$). The fluid domain expands horizontally to infinity in the three-dimensional space. Normally, we may treat the water depth as infinite when the ratio between h and wavelength $\lambda$ is larger than 1/2 (Reference [13], page 246). The difference between infinite depth and finite depth calculations would be negligible.

Two particular cases are going to be studied here, the definitions of the structural boundaries are presented in Figures 2.1 & 2.2.

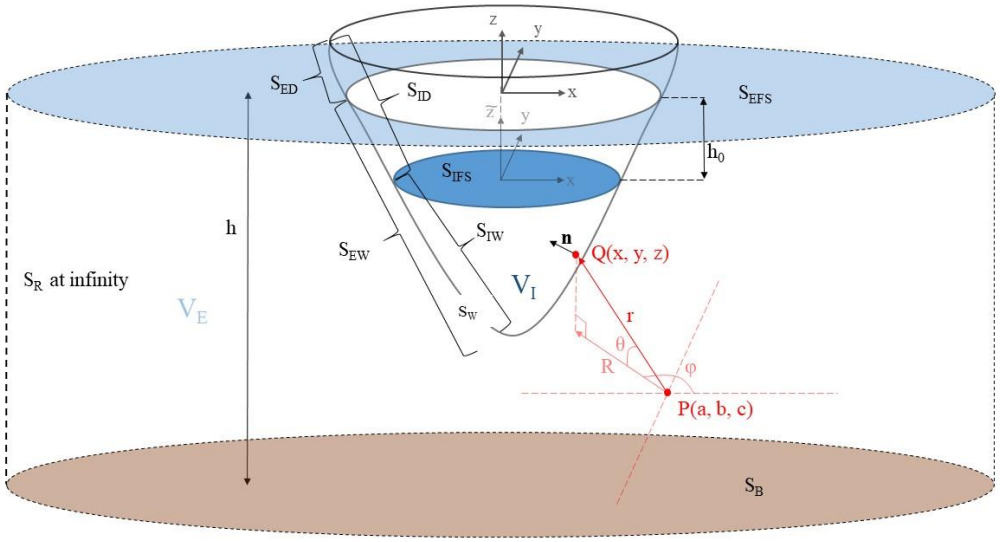


Figure 2.1 The definitions of the objects and the spatial variables for the problem with internal free surface

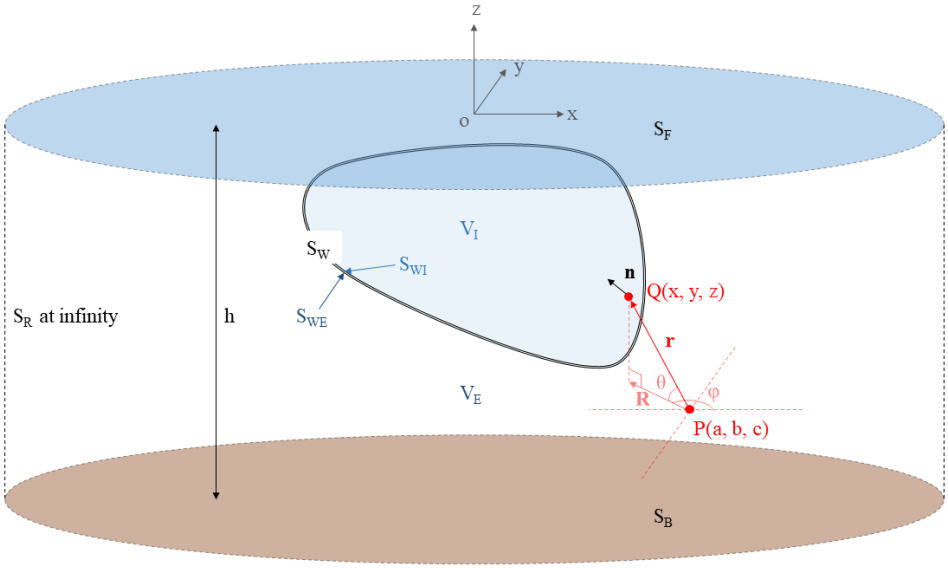


Figure 2.2 The definitions of the objects and the spatial variables in the fully-filled problem

An auxiliary Cartesian coordinate system is located on the calm water free surface within the container in Figure 2.1. This is convenient for modelling. Free surface based origins will be different when the internal and external free surfaces are not at the same level. In this case let $\bar{z} = z - h_0$ be the vertical variable for the internal problem.

When the 'container' wall is very thin, we degenerate the internal and external so that,

$$S_W = S_{EW} \cap S_{IW} . \tag{2.1.3}$$

Continuity requires the internal and external fluid normal velocities over $S_W$ to be the same.

### 2.1.2 Controlling Functions

Since the fluid is incompressible and irrotational, its velocity potential, whether time dependent or not, satisfies the Laplace equation that is,

$$\nabla^2 \Phi = 0 \tag{2.1.4}$$

and

$$\nabla^2 \phi = 0 \tag{2.1.5}$$

On the free surface z = 0, we denote the elevation of wave profile as $H = \eta e^{-i\omega t}$ and determine the linearized kinematic and dynamic free surface conditions in the forms,

$$\frac{\partial \Phi}{\partial t} = -gH \tag{2.1.6}$$

$$\frac{\partial H}{\partial t} = \frac{\partial \Phi}{\partial z} \tag{2.1.7}$$

Substituting for H of the first equation into the second equation yields the composite free surface condition,

$$g\frac{\partial \Phi}{\partial z} + \frac{\partial^2 \Phi}{\partial t^2} = 0 \tag{2.1.8}$$

Thus the time independent velocity potential satisfies,

$$\frac{\partial \phi}{\partial z} - \frac{\omega^2}{g}\phi = 0 \qquad (2.1.9)$$

By solving the Laplace equation through the application of separable variable method, one may establish that the $\omega^2/g$ must satisfy the dispersion relationship,

$$\frac{\omega^2}{g} = \nu \tanh(\nu h) \qquad (2.1.10)$$

As h tends to $+\infty$, tanh(υh) tends to 1 and, therefore, the infinite water depth free surface condition reduce to,

$$\frac{\partial \phi}{\partial z} - \nu\phi = 0 \qquad (2.1.11)$$

The impermeable seabed implies,

$$\left.\frac{\partial \phi}{\partial z}\right|_{z=-h} = 0 \qquad (2.1.12)$$

If the water depth is infinite, this condition is often expressed as,

$$\lim_{z\to-\infty} \frac{\partial \phi}{\partial z} = 0 \qquad (2.1.13)$$

For a radiation or diffraction wave problem, the solution must satisfy the real physic that the waves travels outwards and in reality their energy must be dissipated at large distances from the fluid structure interaction.

Sommerfeld [67] gave the first mathematically rigorous expression that controls the wave field at an infinite distance in the form,

$$\lim_{R\to\infty} R^{(n-1)/2}\left(\frac{\partial \phi}{\partial R} - i\nu\phi\right) = 0 \qquad (2.1.14)$$

The superscript n is the dimension of the wave field and R is the horizontal distance from the source of oscillation. This condition will not ensure waves damp out at far distance, but will regulate the direction of travelling waves. It can be proved that the 3-dimensional potential wave problem is mathematically controlled by a 2-dimensional wave equation (Helmholtz equation) and the value of n this study should be 2.

### 2.1.3 Wave Properties

Suppose the Cartesian spatial variables are denoted as Q(x, y, z) (see Figure 2.1 & 2.2)

and the free surface plane is located at z = 0. For incident waves, there should be no objects inside the fluid domain and, hence, no singularities exists in the expression. The behaviour of incoming water waves are usually 1-dimensional and will not dissipate compare to the scale of the body. Next, assume the incident wave is dominated by excitation of unique direction and the positive x-direction is the direction of propagation.

Through solving Equation 2.1.5, 2.1.7 and 2.1.10, one may determine the potential of incident wave in the following expression,

$$\phi_A = \frac{gA_w}{\omega} \frac{\cosh[\nu(z+h)]}{\cosh(\nu h)} e^{i\nu(x+\alpha)} \tag{2.1.15}$$

where $A_w$ is the wave amplitude and α is the phase shift of the wave shape, which is usually taken as 0. If the depth of h is very large, this expression will reduce to infinite water depth form.

$$\phi = \frac{gA_w}{\omega} e^{\nu z} \cdot e^{i(\nu x+\alpha_1)} \tag{2.1.16}$$

The general solution of the 3-dimensional problem according to the above governing equations and the Sommerfeld condition is of the general form,

$$\phi = \frac{\cosh[\nu(z+h)]}{\cosh(\nu h)} \cos[n(\varphi+\alpha_2)] H_n^{(1)}(\nu R) \tag{2.1.17}$$

where φ is the angular variable under polar coordinate system, α is a constant shift of angle, $H_n^{(1)}$(x) is the Hankel of the first kind and $n^{th}$ integer order, which can be expressed in terms of first and second kind Bessel functions ($J_n$(x) & $Y_n$(x)) as,

$$H_n^{(1)}(x) = J_n(x) + iY_n(x) \tag{2.1.18}$$

The second kind Bessel function is singular at the origin, hence, the solution is physical only when the singularities are excluded from fluid domain. This suggests that propagating waves will not exist independently and constantly if the fluid domain is unbounded or without an oscillating body. The overall result would be a superposition of principles solutions once the boundary condition on the wetted surface is given and this mathematical technique is applied by McCamy and Fuchs [1] to determine the analytical solution of diffraction problem over a vertical cylinder.

However, the Hankel function is insufficient to describe all situations as it requires the domain to be excluded throughout the depth of the singularities. The principle solutions applied for arbitrary shapes and locations are free surface multipoles, where the function is singular only at the source point. Suppose the source of the multipole is located at a fixed point P(a, b, c), then one can determine a series of functions that satisfy all boundary conditions except at the origin through transformation of spherical harmonics and asymptotic analysis. The solution under a finite depth condition is,

$$\phi = \frac{P_l^n(\cos\theta)}{r^{n+1}}\cos n\varphi + (-1)^{l+n}\frac{P_l^n(\cos\theta')}{r_2^{n+1}}\cos n\varphi + \frac{\cos n\varphi}{(l-n)!}\times$$
$$PV\int_0^\infty \frac{e^{-kh}k^l(k+\frac{\omega^2}{g})[e^{k(h+c)}+(-1)^{l+n}e^{-k(h+c)}]}{k\sinh(kh)-\frac{\omega^2}{g}\cosh(kh)}\cosh[k(z+h)]J_n(kR)dk \qquad (2.1.19)$$
$$+i\frac{2\pi\nu^{l+1}\cos n\varphi}{(l-n)!}\frac{[e^{k(h+c)}+(-1)^{l+n}e^{-k(h+c)}]}{2\nu h+\sinh(2\nu h)}\cosh[\nu(z+h)]J_n(\nu R)$$

where $P_l^n(x)$, for integers l & n and $l \geq n$, is called the associated Legendre polynomials of $l^{th}$ degree and $n^{th}$ order, r is the distance between source point P and the generic fluid point Q defined as,

$$r = \sqrt{(x-a)^2+(y-b)^2+(z-c)^2} \qquad (2.1.20)$$

Its horizontal projection on the *x-o-y* plane is,

$$R = \sqrt{(x-a)^2+(y-b)^2} \qquad (2.1.21)$$

$r_2$ is the distance between Q and the image source point of P'(a, b, -2h-c) above the seabed,

$$r_2 = \sqrt{(x-a)^2+(y+b)^2+(z+2h+c)^2} \qquad (2.1.22)$$

φ is the azimuth angle while θ and θ' are the zenith angle from point P and P' it follows that,

$$\cos\varphi = \frac{x-a}{R} \qquad (2.1.23)$$

$$\cos\theta = \frac{z-c}{r} \qquad (2.1.24)$$

$$\cos\theta' = \frac{z+2h+c}{r_2} \tag{2.1.25}$$

For infinite water depth Equation 2.1.19 reduces to,

$$\begin{aligned}\phi = & \frac{P_l^n(\cos\theta)}{r^{n+1}}\cos n\varphi \\ & + \frac{\cos n\varphi}{(l-n)!} PV\int_0^\infty \frac{k+\nu}{k-\nu} k^l e^{k(z+c)} J_n(kR)dk \\ & + i\frac{2\pi\cos n\varphi}{(l-n)!}\nu^{l+1}e^{\nu(z+c)}J_n(\nu R)\end{aligned} \tag{2.1.26}$$

Under multipole expansion method, the overall diffraction or radiation potential is considered to be a linear superposition of infinite orders of multipole sources. The magnitudes of primary orders of multipole are determined through solving a truncated set of linear equations subject to the known boundary conditions at selected representative points on the wetted surface.

From Equation 2.1.19 & 2.1.26, one can derive that the multipole sources dissipate at the following rate for 3-dimensional problem at far field,

$$\phi = \frac{A(\varphi)\cosh[\nu(z+h)]}{\sqrt{\nu R}} + o(R^{-1}) \quad \text{as} \quad R \to +\infty \tag{2.1.27}$$

for finite water depth and for infinite water depth the corresponding behaviour is,

$$\phi = \frac{A(\varphi)e^{\nu z}}{\sqrt{\nu R}} + o(R^{-1}) \quad \text{as} \quad R \to +\infty \tag{2.1.28}$$

where A(φ) is a regular function of φ.

This asymptotic expression is important for the formulation of the integral equation method. All diffraction and radiation waves should satisfy this relationship since the potential in the fluid domain should be a bounded superposition of multipole sources.

Free surface multipole under more conditions can be found in Thorne's work [68], including a 2-dimensional case and the corresponding fluid singularity ln(r).

## 2.2 Boundary Analysis

In this study, we deal with fluid potential force only as the influence of viscosity is considered to be negligible. The method applied is basically a boundary element

analysis controlled by an integral equation related to harmonic functions. The so-called Green function is important to this method and an explanation of its role in determining hydrodynamic loads is explained. The principle of the direct coupling method is introduced in detail from the logic of the integral equation method and the deduction of important steps and objectives are explained.

### 2.2.1 Green Theorem

A function can be called a Green function G if it satisfies the following condition throughout the whole space, namely,

$$\nabla^2 G(Q,P) = \delta(P) \tag{2.2.1}$$

where Q & P satisfy the space coordinate definition of the previous section and δ(P) is the delta function. However, Q & P do not necessarily correspond to 3-dimensional space. By definition δ(P) = +∞ at the point P and δ(x) = 0 over the rest of the definition domain.

From the definition of Green function, it follows that,

$$\iiint_R \nabla^2 G(Q,P)\phi(Q)dV = \iiint_R \delta(P)\phi(Q)dV = \phi(P) \tag{2.2.2}$$

G has different solutions in spaces of different dimensions. In 2-dimensional space, the strict solution of Equation 2.2.1 is.

$$G = \frac{1}{2\pi R} + C \tag{2.2.3}$$

In 3-dimensional space,

$$G = -\frac{1}{4\pi r} + C \tag{2.2.4}$$

in which C can be a constant or any other regular harmonic functions that will facilitate the properly formulated solution process.

In practice, we generally omit the 1/2π & -1/4π coefficient and use the Green function in the form of,

$$G = \frac{1}{R} + C \quad \text{or} \quad G = \frac{1}{r} + C \tag{2.2.5}$$

For free surface problems, we know the expression of the simplest multipole source

with l, n = 0 will include the principal term of 1/r. So we take that function as our free surface Green function. For infinite water depth,

$$G=\frac{1}{r}+PV\int_0^\infty \frac{k+\nu}{k-\nu}e^{k(z+c)}J_0(kR)dk+i2\pi\nu e^{\nu(z+c)}J_0(\nu R) \tag{2.2.6}$$

In the case of 3-dimensional finite water depth,

$$\begin{aligned} G=&\frac{1}{r}+\frac{1}{r_2}\\ &+PV\int_0^\infty \frac{2e^{-kh}(k+\frac{\omega^2}{g})\cosh[k(c+h)]}{k\sinh(kh)-\frac{\omega^2}{g}\cosh(kh)}\cosh[k(z+h)]J_0(kR)dk\\ &+i\frac{4\pi\nu\cosh[\nu(c+h)]\cosh[\nu(z+h)]}{2\nu h+\sinh(2\nu h)}J_0(\nu R) \end{aligned} \tag{2.2.7}$$

Suppose the singularity of the free surface Green function is covered within the body boundary, then both G and fluid potential $\phi$ should satisfy the Laplace equation in the fluid domain and from Green second identity it follows that,

$$\iiint_{V_F}(\phi\nabla^2G-G\nabla^2\phi)dV=\iint_S(\phi\frac{\partial G}{\partial n}-G\frac{\partial\phi}{\partial n})dS=0 \tag{2.2.8}$$

where $V_F$ is the domain of external fluid and S is the boundary surface that encloses $V_F$, $\vec{n}$ is the normal vector point outward of the integration space. The boundary can be viewed as the union of distinct identifiable surfaces, that is,

$$S=S_{FS}\bigcup S_W\bigcup S_S\bigcup S_R \tag{2.2.9}$$

in which $S_{FS}$ is the free surface of the fluid and $S_W$ is the wetted surface of the body. For finite depth problem, $S_S$ is the seabed. A vertical cylindrical boundary $S_R$ of infinite radius $R_c$ provides closure of the fluid domain between free surface and seabed.

On $S_{FS}$, we can have the following relationship from Condition 2.1.9,

$$\frac{\partial\phi}{\partial n}=\frac{\partial\phi}{\partial z}=\omega^2\phi \quad \& \quad \frac{\partial G}{\partial n}=\frac{\partial G}{\partial z}=\omega^2G \tag{2.2.10}$$

Thus it follows that,

$$\iint_{S_{FS}} (\phi \frac{\partial G}{\partial n} - G \frac{\partial \phi}{\partial n}) dS = 0 \tag{2.2.11}$$

While from the Sommerfeld radiation condition (Equation 2.1.14) we have as $R_c \rightarrow \infty$,

$$\frac{\partial \phi}{\partial n} = i\nu\phi + o(R_c^{-1/2}) \quad \& \quad \frac{\partial G}{\partial n} = i\nu G + o(R_c^{-1/2}) \tag{2.2.12}$$

Then integration over $S_R$ reduce to,

$$\iint_{S_R} (\phi - G) o(R_c^{-1/2}) dS \tag{2.2.13}$$

For finite depth problem, we know both $\phi$ & G satisfy Condition 2.1.27, therefore the integration on $S_R$ takes the form,

$$\begin{aligned} &\iint_{S_R} \frac{A(\varphi)\cosh[\nu(z+h)]}{\sqrt{\nu R}} o(R_c^{-1/2}) dS \\ &= \int_0^{2\pi} \frac{A(\varphi)}{\sqrt{\nu}} d\varphi \int_{-z}^{0} \cosh[\nu(z+h)] dz \cdot R_c \cdot o(R_c^{-1}) \end{aligned} \tag{2.2.14}$$

Since the integrations over z and $\varphi$ are bounded, we have,

$$\iint_{S_R} (\phi \frac{\partial G}{\partial n} - G \frac{\partial \phi}{\partial n}) dS = 0 \tag{2.2.15}$$

Similarly, we take Condition 2.1.28 into $S_R$ integration for the infinite depth problem,

$$\begin{aligned} &\iint_{S_R} \frac{A(\varphi) e^{\nu z}}{\sqrt{\nu R}} o(R_c^{-1/2}) dS \\ &= \int_0^{2\pi} \frac{A(\varphi)}{\sqrt{\nu}} d\varphi \int_{-R_c}^{0} e^{\nu z} dz \cdot R_c \cdot o(R_c^{-1}) \\ &= \int_0^{2\pi} \frac{A(\varphi)}{\nu\sqrt{\nu}} d\varphi (1 - e^{-\nu R_c}) \cdot R_c \cdot o(R_c^{-1}) \end{aligned} \tag{2.2.16}$$

This equation tends to 0 as $R_c \rightarrow \infty$.

On finite depth $S_S$, we know $\phi$ & G satisfy the impermeability condition and thus,

$$\frac{\partial \phi}{\partial n} = \frac{\partial \phi}{\partial z} \equiv 0 \quad \& \quad \frac{\partial G}{\partial n} = \frac{\partial G}{\partial z} \equiv 0 \tag{2.2.17}$$

Hence Equation 2.2.6 reduces to,

$$\iint_{S_S}(\phi\frac{\partial G}{\partial n}-G\frac{\partial \phi}{\partial n})dS=0 \tag{2.2.18}$$

While for the boundary $S_S$ in the finite water depth problem,

$$\begin{aligned}&\iint_{S_S}\frac{A(\varphi)e^{\nu z}}{\sqrt{\nu R}}dS\\&=\int_0^{2\pi}\frac{A(\varphi)}{\sqrt{\nu}}d\varphi\int_0^{R_c}\frac{R}{\sqrt{R}}dR\cdot e^{-\nu R_c}\\&=\frac{2}{3}\int_0^{2\pi}\frac{A(\varphi)}{\sqrt{\nu}}d\varphi R_c^{3/2}e^{-\nu R_c}\end{aligned} \tag{2.2.19}$$

As the exponential term converges to 0 much faster than the power function, the integration of $S_S$ also tends to 0 as $R_c \to \infty$ according to the external boundary we defined.

Now only $S_W$ is left in the surface integration. Having demonstrate what happens on the other constituent surfaces, it is clear from Equation 2.2.8 that,

$$\iint_{S_W}(\phi\frac{\partial G}{\partial n}-G\frac{\partial \phi}{\partial n})dS=0 \tag{2.2.20}$$

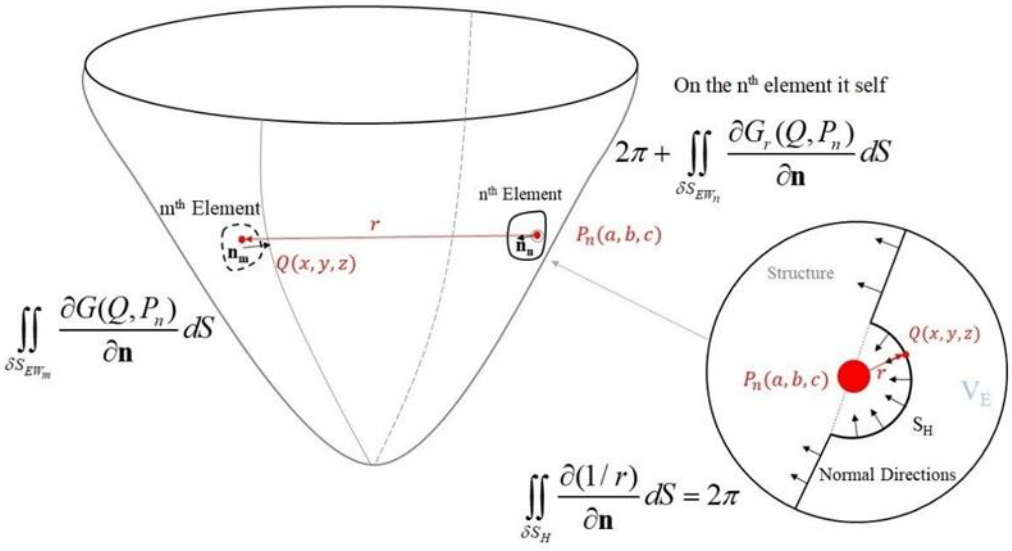


Figure 2.3 External problem integration of $\partial G/\partial \mathbf{n}$ over the m^th element when the fluid source is located at the n^th element centroid

Next, we consider what happens if the fluid singularity is located on the surface of

SW. To keep the singularity out of the fluid domain, we imagine it is covered with an infinite small hemisphere as indicated in Figure 2.3.

We denote the covering hemispherical surface by $S_h$ and the resulting wetted surface is still $S_W$. The normal vector is pointing outward of the fluid and thus inward on $S_W$, so we may write Equation 2.2.20 in the new equivalent form,

$$\iint_{S_W - S_h} (\phi \frac{\partial G}{\partial n} - G \frac{\partial \phi}{\partial n}) dS + \iint_{S_h} (\phi \frac{\partial G}{\partial n} - G \frac{\partial \phi}{\partial n}) dS = 0 \qquad (2.2.21)$$

If we denote the regular part of G by $G_r$ then the integration over $S_h$ becomes,

$$\begin{aligned} &\iint_{S_h} (\phi \frac{\partial G}{\partial n} - G \frac{\partial \phi}{\partial n}) dS \\ &= \iint_{S_h} [\phi(P)(\frac{1}{r^2} + \frac{\partial G_r(Q,P)}{\partial n}) - (\frac{1}{r} + G_r) \frac{\partial \phi(P)}{\partial n}] r^2 d\Omega \end{aligned} \qquad (2.2.22)$$

Here $d\Omega$ is the solid angle of the covering hemisphere. When P is located on the smooth surface, we have $d\Omega = 2\pi$.

Since all other terms are bounded to $o(1/r)$, only the $1/r^2$ term will remain as $r \to 0$, that is,

$$\iint_{S_h} (\phi \frac{\partial G}{\partial n} - G \frac{\partial \phi}{\partial n}) dS = 2\pi\phi(P) \qquad (2.2.23)$$

By partitioning the surface $S_W$ into a number of boundary elements, for which the values of $\phi$ and its derivative are assumed to vary negligibly over any particular individual elementary surface, and taking the corresponding value at the element centroid to be its representative value over the whole boundary element, the integral equation can be approximated into the summation form,

$$(2\pi + \iint_{\delta S_{W_i}} \frac{\partial G_r}{\partial n} ds)\phi_i + \sum_{\substack{n=1 \\ n \neq i}}^{N} \phi_n [\iint_{\delta S_{W_n}} \frac{\partial G}{\partial n} dS] - \sum_{n=1}^{N} (\frac{\partial \phi}{\partial n})_i [\iint_{\delta S_{W_n}} G dS] = 0 \qquad (2.2.24)$$

where N is the number of boundary elements covering $S_W$ and subscript $W_n$ refers to the $n^{th}$ wetted surface boundary element. The integration of regular $G_r$ is undertaken for the $i^{th}$ element that hosts the singularity.

Equation 2.2.24 for one element has N unknowns. By formulating equations for different host $i^{th}$ elements using Equation 2.2.24, a set of N equations with N unknowns

is generated. The equivalent matrix formulation can be solved by undertaking matrix inversion. The matrix form of the N equations is essentially,

$$\mathbf{A}\vec{\phi} = \mathbf{B}\vec{v} \tag{2.2.25}$$

with matrix elements defined by,

$$\mathbf{A_{ii}} = 2\pi + \iint_{\delta S_{W_i}} \frac{\partial (G_r)^i}{\partial n} ds \,, \quad \mathbf{A_{ij}} = \iint_{\delta S_{W_j}} \frac{\partial G^i}{\partial n} dS \tag{2.2.25a}$$

$$\mathbf{B_{ij}} = \iint_{\delta S_{W_j}} G^i dS \tag{2.2.25b}$$

The subscript i denotes the location of the fluid source whereas j indicates the integration of the influence of the i$^{th}$ fluid source upon the j$^{th}$ element.

The velocity potential and normal velocity column vectors are respectively,

$$\vec{\phi} = [\phi_1, \phi_2, \phi_3, ..., \phi_N]^T \tag{2.2.25c}$$

$$\vec{v} = [(\frac{\partial \phi}{\partial n})_1, (\frac{\partial \phi}{\partial n})_2, (\frac{\partial \phi}{\partial n})_3, ..., (\frac{\partial \phi}{\partial n})_N]^T \tag{2.2.25d}$$

Hydrodynamic pressure can be determined from the fluid velocity potential through the linearized Bernoulli's equation, namely,

$$\frac{\partial \Phi}{\partial t} + \frac{P}{\rho} = (-i\omega\phi + \frac{1}{\rho} p) e^{-i\omega t} = 0 \tag{2.2.26}$$

Whilst Equation 2.2.25c contains each boundary element velocity-potential value, Equation 2.2.25d contains the normal boundary motion velocity for each boundary element. Combining Equation 2.2.25c with Equation 2.2.26 yields a simple algebraic expression for the external hydrodynamic pressure as a function of $\partial\phi/\partial\mathbf{n}$ on $S_{WE}$, namely,

$$\vec{p} = i\omega\rho\vec{\phi} = i\omega\rho\mathbf{A}^{-1}\mathbf{B}\vec{v} \quad . \tag{2.2.27}$$

For analysing external hydrodynamic problems this relationship is expressible as,

$$\overrightarrow{p_E} \quad = \quad \mathbf{f_E}\overrightarrow{v_E} \tag{2.2.28}$$

with $\mathbf{f_E} = i\omega\rho\mathbf{A}^{-1}\mathbf{B}$.

### 2.2.2 Formulations of Internal Domain

The relationship between flow potential and its normal derivatives on the selected boundary can be analysed similarly for $V_I$ in Figures 2.1 & 2.2. A key difference with the normal external fluid formulation is that the covering of the fluid singularities on the structure boundary requires a change in sign of integration over $S_h$, (See Figure 2.4).

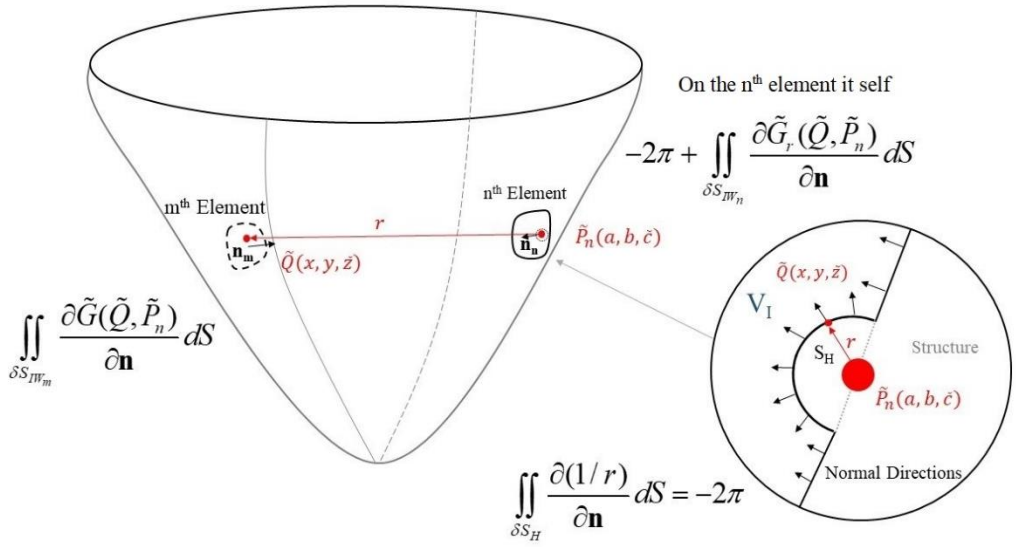


Figure 2.4 Internal problem integration of $\partial\tilde{G}/\partial\mathbf{n}$ over the m^th element when the fluid source is located at the n^th element centroid

or an internal problem with a free surface, the Laplace equation (Equation 2.1.5) and the free surface condition (Equation 2.1.9) govern the flow provided the assumption of small amplitude holds. (To distinguish the internal fluid from the external fluid, variables related to vertical direction change from z to $\bar{z}$ in all functions and their associated derivatives).

The boundary of volume $V_I$ now comprises,

$$S' = S_{IFS} \bigcup S_{IW} \ . \tag{2.2.29}$$

With the definitions of r and R unchanged, the second identity of Green becomes:

$$\iiint_{V_I} (\phi_I \nabla^2 \tilde{G} - \tilde{G} \nabla^2 \phi_I) dV = \iint_{S'} (\phi_I \frac{\partial \tilde{G}}{\partial \mathbf{n}} - \tilde{G} \frac{\partial \phi_I}{\partial \mathbf{n}}) dS = 0 . \tag{2.2.30}$$

Satisfaction of Equation 2.1.9 by $\phi_I$ and $\tilde{G}$ implies

$$\iint_{S_{IFS}} (\phi_I \frac{\partial \tilde{G}}{\partial \tilde{z}} - \tilde{G} \frac{\partial \phi_I}{\partial \tilde{z}}) dS = 0 \tag{2.2.31}$$

This suggests that $\Phi_I$ on the internal free surface does not need consideration. The Green's function $\tilde{G}$ can correspond to either finite or infinite water depth, provided no singularity is included within $V_I$.

Applying a boundary element discretisation to the remaining internal wetted surface integrals yields,

$$\begin{aligned} &(-2\pi + \iint_{\delta S_{IW_n}} \frac{\partial \tilde{G}_r(\tilde{Q}, \tilde{P}_n)}{\partial \mathbf{n}} ds)\, {}^n\phi_I \\ &+ \sum_{\substack{m=1 \\ m \neq n}}^{N} {}^m\phi_I [\iint_{\delta S_{IWm}} \frac{\partial \tilde{G}(\tilde{Q}, \tilde{P}_n)}{\partial \mathbf{n}} dS] - \sum_{m=1}^{N} {}^m(\frac{\partial \phi_I}{\partial \mathbf{n}}) [\iint_{\delta S_{IW_m}} \tilde{G}(\tilde{Q}, \tilde{P}_n) dS] = 0 \end{aligned} \tag{2.2.32}$$

As already noted, the integration of $\partial(1/r)/\partial(\mathbf{n})$ over the host element yields $-2\pi$, since the internal fluid domain $V_I$ excludes P.

The resulting matrix equation for the internal hydrodynamic problem, consistent with Equation 2.2.25, is:

$$\tilde{\mathbf{A}} \overrightarrow{\phi_I} = \tilde{\mathbf{B}} \overrightarrow{v_I} \tag{2.2.33}$$

with,

$$\tilde{\mathbf{A}}_{nn} = -2\pi + \iint_{\delta S_{IWn}} \frac{\partial \tilde{G}_r(\tilde{Q}, \tilde{P}_n)}{\partial \mathbf{n}} ds , \quad \tilde{\mathbf{A}}_{nm} = \iint_{\delta S_{IWm}} \frac{\partial \tilde{G}(\tilde{Q}, \tilde{P}_n)}{\partial \mathbf{n}} dS \tag{2.2.33a}$$

$$\tilde{\mathbf{B}}_{nm} = \iint_{\delta S_{IWm}} \tilde{G}(\tilde{Q}, \tilde{P}_n) dS \tag{2.2.33b}$$

$$\overrightarrow{\phi_I} = [{}^1\phi_I, {}^2\phi_I, {}^3\phi_I, ..., {}^N\phi_I]^T \tag{2.2.33c}$$

$$\overrightarrow{v_I} = [{}^1(\frac{\partial \phi_I}{\partial \mathbf{n}}), {}^2(\frac{\partial \phi_I}{\partial \mathbf{n}}), {}^3(\frac{\partial \phi_I}{\partial \mathbf{n}}), ..., {}^N(\frac{\partial \phi_I}{\partial \mathbf{n}})]^T \tag{2.2.33d}$$

Arguments analogous to those justifying Equation 2.2.28 lead to the relationships

$$\begin{aligned} \overline{p_I} &= \mathbf{f_I}\overline{v_I} \\ \mathbf{f_I} &= i\omega\rho_I \tilde{\mathbf{A}}^{-1}\tilde{\mathbf{B}} \end{aligned} \tag{2.2.34}$$

for the internal hydrodynamic pressure function of normal velocity on the internal wetted surface. Furthermore, when the internal wetted surface boundary motion is $\bar{v}_I = 0$, solutions still exist for the internal dynamic behaviour if $\mathbf{f_I}$ is singular. The corresponding ω is the small amplitude natural resonant frequency of the fluid containing structure determined from $det(\mathbf{f_I}) = 0$. However, higher order methods are required to solve the internal fluid response near resonance since the linear assumption is no longer valid; the physics being akin to container sloshing.

For a fully closed fluid domain, 1/r is enough to formulate the relationships we need. Theoretically, it does not matter if we add to it an arbitrary harmonic function as long as no singularity is included. One may directly minus a -4π on the trace of matrix **A** in Equation 2.2.25 to obtain the operator needed. However, non-uniqueness occurs with this characteristic for closed boundary problem.

### 2.2.3 Hydrodynamic Force

The above deduction gives the basic concept of the source method commonly used to solve the wave-body interactions of rigid structures. Consider the radiation problem. If a rigid body is oscillating at a constant frequency in still water in the r$^{th}$ direction $\vec{n}_r$, we can specify the associated boundary condition as,

$$\begin{aligned} \vec{v}_r &= [(\frac{\partial \phi_r}{\partial n})_1, (\frac{\partial \phi_r}{\partial n})_2, (\frac{\partial \phi_r}{\partial n})_3, ..., (\frac{\partial \phi_r}{\partial n})_N]^T \\ &= [\vec{n}_r \cdot \vec{n}^1, \vec{n}_r \cdot \vec{n}^2, ..., \vec{n}_r \cdot \vec{n}^j, ..., \vec{n}_r \cdot \vec{n}^N]^T \end{aligned} \tag{2.2.35}$$

where $\vec{n}^j$ is the normal vector on the j$^{th}$ boundary element. Then the value of fluid potential and, hence, hydrodynamic pressure acting on each element (induced by radiation) are determined through the matrix operations,

$$\vec{\phi}_r = \mathbf{A}^{-1}\mathbf{B}\vec{v}_r \tag{2.2.36}$$

$$\vec{p}_r = i\omega\rho\vec{\phi}_r = \mathbf{f_E}\vec{v}_r \tag{2.2.37}$$

For the diffraction problem, where the rigid body is fixed, we know the normal

velocity at the wetted surface should be 0. Therefore, since the incident wave velocity vector at the j$^{th}$ element is known then,

$$\vec{n}_A^j = [-i\omega\frac{\partial\phi_A}{\partial x}, -i\omega\frac{\partial\phi_A}{\partial y}, -i\omega\frac{\partial\phi_A}{\partial z}]^T \Big|_{(x,y,z)=(x_j,y_j,z_j)} \tag{2.2.38}$$

Continuity of the boundary motion and fluid motion over the wetted surface of the structure requires (given a subscript 'A' for incident wave is consistent with Equation 2.1.15,

$$\vec{v}_D = -\vec{v}_A = [-\vec{n}_A^1 \cdot \vec{n}^1, -\vec{n}_A^2 \cdot \vec{n}^2, ..., -\vec{n}_A^j \cdot \vec{n}^j, ..., -\vec{n}_A^N \cdot \vec{n}^N]^T \tag{2.2.39}$$

The resulting diffraction potential and pressure at the boundary is,

$$\vec{\phi}_D = \mathbf{A}^{-1}\mathbf{B}\vec{v}_D \tag{2.2.40}$$

$$\vec{p}_D = i\omega\rho\vec{\phi}_D = -\mathbf{f}_\mathbf{E}\vec{v}_A \tag{2.2.41}$$

The total solution will be its linear summation with the incident potential wave.

For an oscillating body under excitation, at the wave frequency, the boundary condition must satisfy,

$$\begin{aligned} \vec{v}_C + \vec{v}_A &= \vec{v}_r \\ \vec{v}_C = \vec{v}_r - \vec{v}_A &= \vec{v}_r + \vec{v}_D \end{aligned} \tag{2.2.42}$$

This means the resulting hydrodynamic response of a moving body under an incoming wave can be taken as a linear superposition of the radiation solution in still water and the diffraction solution generated supposing the structure is fixed.

For any wave-body interaction problem, if we want to determine the motion of single or multibody structures, due to excitation waves, we need to couple the resulting hydrodynamic force with the structural response. Proper mathematical formulations for the structural behaviour is necessary and addressed next.

## 2.3 Structural Analysis

Equation 2.2.27 & 2.2.33 have revealed the relationship between normal boundary velocity and the inducing hydrodynamic pressure acting on the structural surface. Complete physical formulation is required to capture the proper dynamic of the whole

system. For a direct coupling method under linear assumption, it usually means deriving a structural matrix **U** such that,

$$\vec{v} = \mathbf{U}\vec{p} \tag{2.3.1}$$

where the n$^{th}$ row, m$^{th}$ column element of **U** is the resulting normal velocity of the n$^{th}$ element when unit pressure is acting on the m$^{th}$ boundary element. (Hearn, who described the concept in terms of 'Poke Functions', suggested this approach.)

### 2.3.1 Finite Element Analysis

For linear elastic structures, the relationship **U** of Equation 2.3.1 can be determined through finite element analysis, which is a numerical method based on Lagrangian dynamic theory. Normally, the matrix equation for a dynamic problem in the frequency domain analysis written as:

$$(-\omega^2\mathbf{M} - i\omega\mathbf{C} + \mathbf{K})\vec{u} = \mathbf{D}\vec{u} = \vec{f}\ . \tag{2.3.2}$$

Here $\vec{u}$ is a list vector containing the general displacement of element nodes to each degree of freedom, $\vec{f}$ is the general forces acting on the corresponding finite element nodes, **M** is the mass matrix, **C** is the damping matrix, **K** is the stiffness matrix and **D** derived from **M**, **C** & **K** is the dynamic stiffness matrix. Figure 2.5 illustrates the quantities addressed at each node of a typical finite element.

Proper interpolation function is required to distribute the uniform load onto the element nodes. In this study, the order of interpolation is the lowest (See Figure 2.5). The nodes of the finite elements coincide with the centroids of simple constant value based boundary elements of the hydrodynamic analysis with $\vec{u}$ corresponding to the normal displacement of the boundary motion. Therefore, noting $\bar{v} = -i\omega\bar{u}$ for the external problem it follows that

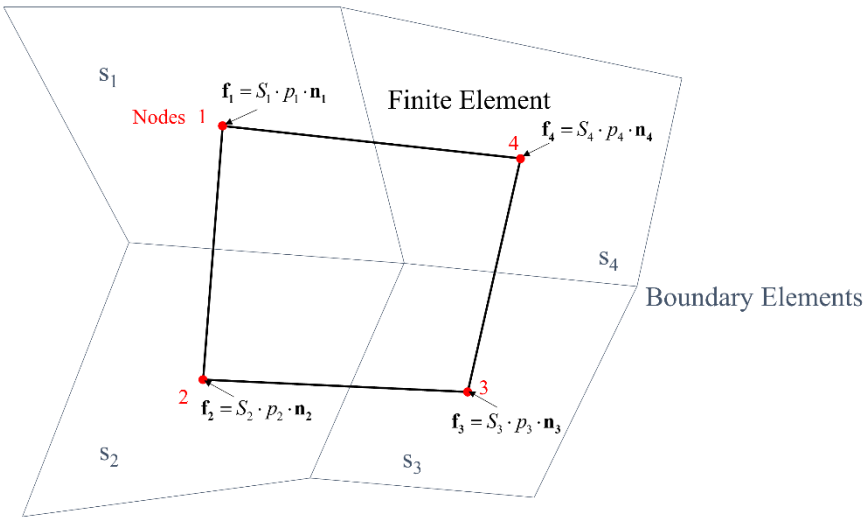


Figure 2.5 A sketch of force interpolation on an individual finite element. The pressure $p_n$ acting on the $n^{th}$ element is assumed uniform in the BEA formulation and the force acting on the $n^{th}$ centroid, which is the corresponding finite element node, is pressure multiplied by its area $s_n$

Proper interpolation function is required to distribute the uniform load onto the element nodes. In this study, the order of interpolation is the lowest (See Figure 2.5). The nodes of the finite elements coincide with the centroids of simple constant value based boundary elements of the hydrodynamic analysis with $\vec{u}$ corresponding to the normal displacement of the boundary motion. Therefore, noting $\vec{v} = -i\omega\vec{u}$ for the external problem it follows that

$$\frac{i}{\omega}\mathbf{D}\vec{v} = \vec{f}\,. \tag{2.3.3}$$

On the right hand side of the Equation 2.3.3 we modify the force vector to reflect the pressure we are studying, that is,

$$\frac{i}{\omega}\mathbf{D}\vec{v} = \mathbf{S}\overrightarrow{p_{net}}\,. \tag{2.3.4}$$

Matrix **S** is diagonal and expressible as,

$$\mathbf{S} = diag(s_1, s_2, s_3, \ldots, s_N)\,. \tag{2.3.5}$$

It is better to utilise the inverse of matrix S in real practice. It is a trivial operation, but also matrix **D** would become singular when natural vibration frequencies are reached for the structure in vacuum.

General finite element monographs [69, 70] provide specification of **M**, **C** & **K** for plate, shell or solid finite elements. Usually, the nodal variables determined directly are not exactly the normal displacements and, hence, local coordinate transformations are required to correct the directions. Static condensation is required to collapse the unnecessary rows and columns of the matrices.

### 2.3.2 Rigid Body Dynamic

For regular structures, linear superimposition provides required dynamic responses. This is equivalent to determining **U** through dynamic procedures. This observation is particularly important when a finite element analysis fails for a rigid structure. It enables the development of a direct coupling method for more general models.

For a free rigid body or container, unit pressure acting on the $n^{th}$ element in the internal direction will result in a translational and rotational response over the mass centroid O. Figure 2.6 indicates the spatial variables involved.

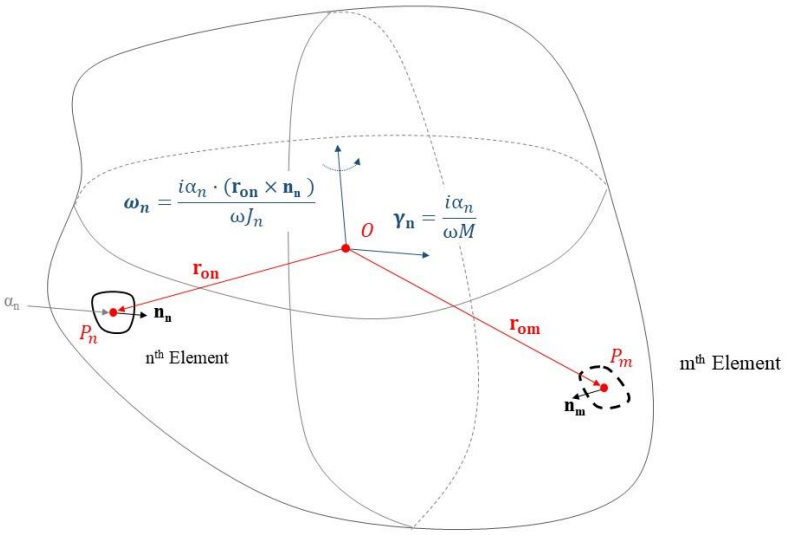


Figure 2.6 Definitions of variables for rigid boundary analysis

Considering unit pressure, the translation force $f_n$ is simply equal to the facet area $\alpha_n$ and since local acceleration satisfies $a_n = -i\omega\gamma_n = f_n/M$, the induced centroid velocity $\gamma_n$ satisfies

$$\boldsymbol{\gamma}_{\mathbf{n}} = \frac{i\alpha_n \mathbf{n}_n}{\omega M} \tag{2.3.6}$$

For a total body mass M. Similarly, with $J_n$ being the body moment of inertia around the rotation axis vector $\boldsymbol{\omega}_{\mathbf{n}}$, the angular velocity of the rigid body satisfies,

$$\omega_{\mathbf{n}} = \frac{i\alpha_n (\mathbf{r}_{on} \times \mathbf{n}_n)}{\omega J_n} \tag{2.3.7}$$

The normal velocity response of the $m^{th}$ boundary, which corresponds to the $n^{th}$ row, $m^{th}$ column element of matrix **U** is

$$\mathbf{U}_{nm} = \mathbf{n}_{\mathbf{m}} \cdot (\boldsymbol{\gamma}_{\mathbf{n}} + \boldsymbol{\omega}_{\mathbf{n}} \times \mathbf{r}_{\mathbf{om}}) . \tag{2.3.8}$$

It is not necessary to determine another response matrix for internal action on a thin walled container as net pressure is the acting force.

**U** is similarly derivable for rigid models with more complex structure, provided a proper rigid body reaction can be determined. Examples include a hinged Cockerell raft or an anchored buoy.

### 2.3.3 Mixed 1-Dimensional Analysis

The structural analysis logic developed above can equally address a 3-dimensional hydrodynamic analysis when the elastic structure is of lower dimensions. A special structure is to be analysed with this mixture of formulation.

In Figure 2.7, we present a 1-dimensional elastic cylindrical beam. The hydrodynamic force acting on the beam is 3-dimensional over its wetted surface. The beam side surface boundary element mesh centroid coincide with the same cross-sectional areas of the corresponding beam nodes.

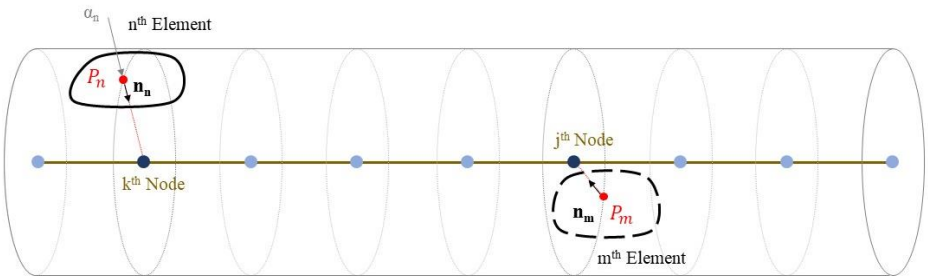


Figure 2.7 A 1-dimensional elastic cylindrical beam model coupled with a 3-dimensiontial hydrodynamic analysis. The dots are the node points of the beam.

When a unit pressure is acting on the $n^{th}$ point of the boundary element, it is equivalent to a force of magnitude $\alpha_n$ acting on the $k^{th}$ node of the beam. If the dynamic stiffness of the beam is $\mathbf{D_B}$, the resulting velocity response of the $j^{th}$ node is:

$$\mathbf{u_j} = -i\omega[\mathbf{D_B^{-1}}]_{k'j'}\mathbf{n}_n \tag{2.3.9}$$

j' and k' indicate the selected element of inverse matrix $\boldsymbol{D_B^{-1}}$ with respect to the transverse displacement of the nodes; other nodal degrees of freedom (rotations) have no contribution to the boundary normal displacement. The elements in matrix **U** are thus

$$\mathbf{U}_{nm} = \mathbf{u_j} \cdot \mathbf{n_m} = -i\omega(\mathbf{D_B^{-1}})_{k'j'}\mathbf{n_n} \cdot \mathbf{n_m}\,. \tag{2.3.10}$$

For other beams, or, when the boundary elements at the ends need inclusion, a unit force acting on the boundary element could result in torsion, axial tension and bending moment over certain nodes. For problems that are more general the rule for the determination of **U** is unaltered, since only normal velocity responses are required

## 2.4 Direct Coupling Procedures

Combining Equation 2.2.28, 2.2.34 & 2.3.1 will immediately give,

$$\vec{v} = \mathbf{U}(\overrightarrow{p_0} + \mathbf{f_E}\vec{v} - \mathbf{f_I}\vec{v}) \tag{2.4.1}$$

This assumes velocity continuity on $S_W$ and $\overrightarrow{p_0}$ is the wave excitation force determined from incident and diffraction wave pressure. The boundary normal velocity is thus,

$$\vec{v} = [\mathbf{I} - \mathbf{U}\mathbf{f_E} + \mathbf{U}\mathbf{f_I}]^{-1}\mathbf{U}\overrightarrow{p_0} \tag{2.4.2}$$

For solid bodies or structures without internal fluid, the internal term $f_I$ is zero. Flexibility is provided by the direct coupling method when considering velocity as a function of loading, since the determination of dynamic matrices in Section 3.1.1 is not always feasible.

Some verification and examples of this primary procedure will be demonstrated. However, it is challenging to introduce a fully filled model into the formulation. Alternative forms are to be discussed for more special and general cases.

### 2.4.1 Non-uniqueness Problem

The standard form of the linearized Bernoulli equation in the frequency domain is,

$$-p + i\omega\rho\phi \quad = \quad c\,. \tag{2.4.3}$$

Here, c is a spatially independent constant. It can be understand as a universal pressure acting throughout the space, but has no influence on the flow variation and, hence, zero is a default for most hydrodynamic problems. For regular wave-body interaction problems, it must be treated as zero for continuity of pressure at the fluid-atmosphere interface.

For the fully filled model discussed here, c is a separated harmonic variable in the form similar to Equation 2.1.1, since external excitation and the resulting internal response are both harmonic. More strictly, one may consider another constant pressure term $C_0$ in the Bernoulli's equation,

$$(-p + i\omega\phi)e^{-i\omega t} \quad = \quad C_0 + ce^{-i\omega t} \tag{2.4.4}$$

where $C_0$ represents a pre-pressurised term acting on $S_{WI}$. However, within linear analysis, $C_0$ only contributes to the equilibrium state of the structure at rest.

For regular wave analysis, the solution of the Laplace Equation 2.1.5 is solved with a Robin boundary condition, that is, the free surface boundary condition in Equation 3.1.9. This condition ensures that the solution of $\phi$ is unique when $\partial\phi/\partial\mathbf{n}$ is known on the oscillating structural boundary. Parameter c is zero when applying Bernoulli equation for hydrodynamic loading here as zero pressure of the atmosphere is included in the free surface boundary implicitly. Therefore, a unique hydrodynamic solution is always obtainable for an open free surface fluid.

However, for a fully filled container described previously, the free surface and free surface condition of Equation 2.1.9 is removed. The boundary condition is now a Neumann condition with $\partial\phi/\partial\mathbf{n}$ on $S_{WI}$. The internal solution of $\phi_I$ is now non-unique, since an arbitrary constant is a solution to $\partial\phi/\partial\mathbf{n} = 0$ and can be added to an appropriate solution. Meanwhile, the Bernoulli pressure constant c can no longer be treated as zero for an isolated fluid volume. Furthermore, its resultant loading is not negligible in terms of the deformation of the flexible shell.

If $\partial\phi/\partial\mathbf{n}$ is the input variable, as introduced in the existing direct coupling method, these two facts mean it is not possible to provide a proper motion-dynamic relationship. What we would observe is that the inverse of matrix **A** in Equation 2.2.23 with G = 1/r is impossible. The non-unique nature of the Neumann problem suggests matrix **A** must be singular (ill conditioned in numerical practice) as 0 must be its eigenvalue, with a corresponding constant eigenvector.

By invoking the reverse problem of Neumann problem, that is, a Dirichlet problem a unique solution is possible. Thus the internal hydrodynamic pressure $p_I$ is a good replacement of $\partial\phi/\partial\mathbf{n}$ to establish the dynamic-response relationship.

Since matrix $\tilde{\boldsymbol{B}}$ is always non-singular we replace the step implied by Equation 2.2.34 with,

$$\overrightarrow{v_I} = \tilde{\mathbf{B}}^{-1}\tilde{\mathbf{A}}\overrightarrow{\phi_I} \tag{2.4.5}$$

Establishing that the constant c in Equation 2.4.3 is ignorable requires substitution of

$$\phi_I = \frac{ic}{\omega} - \frac{ip_I}{\omega\rho_I} \tag{2.4.6}$$

into Equation 2.4.5, after expressing Equation 2.4.6 in list vector form, to give

$$\overrightarrow{v_I} = \tilde{\mathbf{B}}^{-1}\tilde{\mathbf{A}}\frac{i\vec{c}}{\omega} - \tilde{\mathbf{B}}^{-1}\tilde{\mathbf{A}}\frac{i\overrightarrow{p_I}}{\omega\rho_I} \tag{2.4.7}$$

The solution of $\partial\phi/\partial\mathbf{n}$ for a constant c on the boundary is 0, hence, the first right hand term of Equation 2.4.7 is redundant. Therefore, c is an unnecessary unknown when analysing the internal fluid velocity. The numerical tests suggest that one would obtain a solution of $o(10^{-3})$ error when taking unit constant c into the calculation.

Next, instead of having a matrix formulation solving hydrodynamic pressure from normal boundary velocity, an inverse function is required when the internal domain is fully closed. That is, reducing Equation 3.4.7 to the form

$$\overrightarrow{v_I} = \mathbf{T_I}\overrightarrow{p_I} \tag{2.4.8a}$$

requires

$$\mathbf{T_I} = -\frac{i\tilde{\mathbf{B}}^{-1}\tilde{\mathbf{A}}}{\omega\rho_I} \tag{2.4.8b}$$

The unknown directly solved is $p_I$.

### 2.4.2 Alternative Formulation

With the fundamental relationship in Equation 2.4.1 unchanged, we have,

$$\tilde{\mathbf{D}}\vec{v} = \overrightarrow{p_E} + \overrightarrow{p_0} - \overrightarrow{p_I}\,. \tag{2.4.9}$$

where $\tilde{\boldsymbol{D}} = \mathrm{i}\boldsymbol{D}\boldsymbol{S}^{-1}/\omega$ is the corrected dynamic matrix

Combining Equations 2.2.28, 2.2.34 & 2.4.9 yields,

$$(\tilde{\mathbf{D}}\mathbf{T}_\mathbf{I} - \mathbf{f}_\mathbf{E}\mathbf{T}_\mathbf{I} + \mathbf{I})\overrightarrow{p_I} = \overrightarrow{p_0} \tag{2.4.10}$$

Let

$$\mathbf{L} = \tilde{\mathbf{D}}\mathbf{T}_\mathbf{I} - \mathbf{f}_\mathbf{E}\mathbf{T}_\mathbf{I} + \mathbf{I} \tag{2.4.11}$$

We can solve the induced internal pressure with,

$$\overrightarrow{p_I} = \mathbf{L}^{-1}\overrightarrow{p_0}\,. \tag{2.4.12}$$

and determine the dynamic response of the structure with Equation 2.4.8.

### 2.4.3 Half-Closed Boundary

The technique developed for solving a closed internal boundary can be for a domain that is not actually closed.

Figure 2.8 presents a hollow shell model, with an open elastic $S_W$ submerged under the free surface. An imaginary opened boundary $S_0$ provides closure to the internal fluid domain $V_I$.

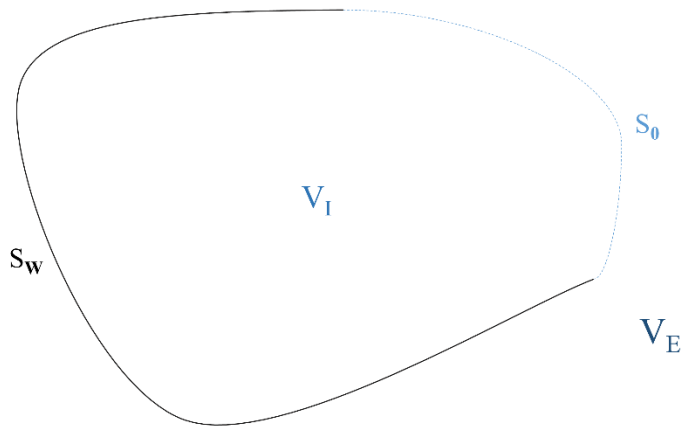


Figure 2.8 An opened container for analysis, the internal fluid domain is wrapped by elastic boundary $S_W$ and imaginary surface $S_0$.

We assume that the elements on $S_W$ are numbered from 0 to N – M while elements on the imaginary boundary is numbered form N – M to N. the matrix Equation 2.4.9 can be partitioned as,

$$\begin{bmatrix} \mathbf{D_{WW}} & \mathbf{0} \\ \mathbf{0} & \mathbf{0} \end{bmatrix} \begin{bmatrix} \vec{v}_W \\ \vec{v}_0 \end{bmatrix} = \begin{bmatrix} \vec{p}_{0W} \\ \vec{p}_{00} \end{bmatrix} + \begin{bmatrix} \mathbf{f_{EWW}} & \mathbf{f_{EW0}} \\ \mathbf{f_{E0W}} & \mathbf{f_{E00}} \end{bmatrix} \begin{bmatrix} \vec{v}_W \\ \vec{v}_0 \end{bmatrix} - \begin{bmatrix} \vec{p}_{IW} \\ \vec{p}_{I0} \end{bmatrix} \tag{2.4.13}$$

Elements in the dynamic matrix out of $S_W$ are assigned with a 0 since physically there is no stiffness.

The lower row of the equation suggests,

$$\vec{p}_{I0} = \vec{p}_{00} + \mathbf{f_{E0s}}\vec{v}_W + \mathbf{f_{E00}}\vec{v}_0 \tag{2.4.14}$$

The term on the left hand side is the internal hydrodynamic pressure. The first term on the right hand side is the excitation force, while the second and third terms are the radiation pressure acting on $S_0$ due to the motion and flux over $S_W$ & $S_0$. The equation indicates a continuity of pressure over the imaginary surface. Hence, a procedure developed for solving a closed structure is directly applicable to an open structure. More extremely, we can let $S_W$ to be a plane while $S_0$ is an arbitrary boundary to model behaviour.

### 2.4.4 Multi-Domain Analysis

In order to demonstrate the developed method is capable of addressing complex cases, rather than just a monocular container, the example has a double internal fluid domain.

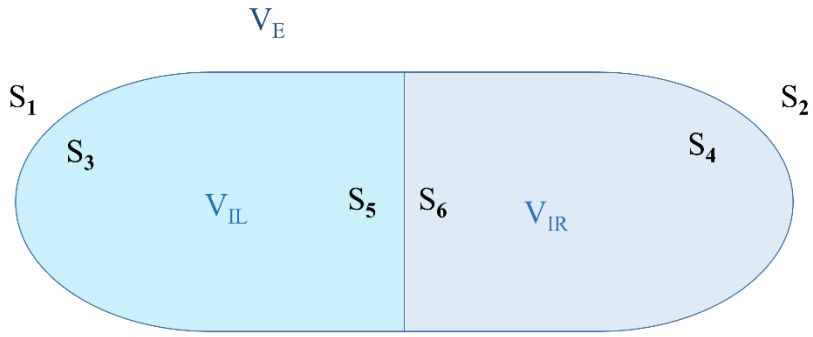


Figure 2.9 The Sketch of a container with two adjacent closed domains. Subscripts with odd numbers indicates the surfaces covering the left domain while surfaces of even number bound right domain. $S_{3\sim6}$ are the internal surfaces.

Continuity of normal velocity is not only satisfied over each internal and external boundary, but also applies across $S_5$ & $S_6$. We cannot make further simplification here as there is pressure action on $S_5$ & $S_6$ and these are essentially independent unknowns. One must study the internal pressure as discussed in Sections 2.4.1 & 2.4.2 to formulate the proper hydrodynamic relationship.

The equation for the external problem is,

$$\begin{bmatrix} \vec{p}_{E1} \\ \vec{p}_{E2} \end{bmatrix} = \begin{bmatrix} \mathbf{f}_{\mathbf{EWW}} & \mathbf{f}_{\mathbf{EW0}} \\ \mathbf{f}_{\mathbf{E0W}} & \mathbf{f}_{\mathbf{E00}} \end{bmatrix} \begin{bmatrix} \vec{v}_1 \\ \vec{v}_2 \end{bmatrix} \tag{2.4.14}$$

whereas for the two internal domains we have,

$$\begin{bmatrix} \vec{v}_1 \\ \vec{v}_5 \end{bmatrix} = \begin{bmatrix} \mathbf{f}_{\mathbf{I11}} & \mathbf{f}_{\mathbf{I15}} \\ \mathbf{f}_{\mathbf{I51}} & \mathbf{f}_{\mathbf{I55}} \end{bmatrix} \begin{bmatrix} \vec{p}_{I1} \\ \vec{p}_{I5} \end{bmatrix} \tag{2.4.15}$$

$$\begin{bmatrix} \vec{v}_2 \\ \vec{v}_6 \end{bmatrix} = \begin{bmatrix} \mathbf{f}_{\mathbf{I22}} & \mathbf{f}_{\mathbf{I26}} \\ \mathbf{f}_{\mathbf{I62}} & \mathbf{f}_{\mathbf{I66}} \end{bmatrix} \begin{bmatrix} \vec{p}_{I2} \\ \vec{p}_{I6} \end{bmatrix} \tag{2.4.16}$$

The overall dynamic equation is,

$$\mathbf{D} \begin{bmatrix} \vec{v}_1 \\ \vec{v}_2 \\ \vec{v}_5 \\ \vec{v}_6 \end{bmatrix} = \vec{p}_0 + \begin{bmatrix} \vec{p}_{E1} \\ \vec{p}_{E2} \\ 0 \\ 0 \end{bmatrix} - \begin{bmatrix} \vec{p}_{I1} \\ \vec{p}_{I2} \\ \vec{p}_{I5} - \vec{p}_{I6} \\ \vec{p}_{I6} - \vec{p}_{I5} \end{bmatrix} \tag{2.4.17}$$

It should be noted that elements in matrix **D** corresponding to the nodes on $S_5$ & $S_6$ are anti-symmetric due to continuity and, hence, the continuity of normal velocity is implicitly satisfied with such a formulation.

Velocities and external pressure can be expressed with internal pressures by combining Equations 2.4.15 ~ 2.4.17, that is.

$$\mathbf{D} \begin{bmatrix} \mathbf{f}_{\mathbf{I11}} \vec{p}_{I1} + \mathbf{f}_{\mathbf{I15}} \vec{p}_{I5} \\ \mathbf{f}_{\mathbf{I22}} \vec{p}_{I2} + \mathbf{f}_{\mathbf{I26}} \vec{p}_{I6} \\ \mathbf{f}_{\mathbf{I51}} \vec{p}_{I1} + \mathbf{f}_{\mathbf{I55}} \vec{p}_{I5} \\ \mathbf{f}_{\mathbf{I62}} \vec{p}_{I2} + \mathbf{f}_{\mathbf{I66}} \vec{p}_{I6} \end{bmatrix} = \tag{2.4.18}$$

$$\vec{p}_0 + \begin{bmatrix} \mathbf{f}_{\mathbf{EWW}}(\mathbf{f}_{\mathbf{I11}}\vec{p}_{I1} + \mathbf{f}_{\mathbf{I15}}\vec{p}_{I5}) + \mathbf{f}_{\mathbf{EW0}}(\mathbf{f}_{\mathbf{I22}}\vec{p}_{I2} + \mathbf{f}_{\mathbf{I26}}\vec{p}_{I6}) \\ \mathbf{f}_{\mathbf{E0W}}(\mathbf{f}_{\mathbf{I11}}\vec{p}_{I1} + \mathbf{f}_{\mathbf{I15}}\vec{p}_{I5}) + \mathbf{f}_{\mathbf{E00}}(\mathbf{f}_{\mathbf{I22}}\vec{p}_{I2} + \mathbf{f}_{\mathbf{I26}}\vec{p}_{I6}) \\ 0 \\ 0 \end{bmatrix} - \begin{bmatrix} \vec{p}_{I1} \\ \vec{p}_{I2} \\ \vec{p}_{I5} - \vec{p}_{I6} \\ \vec{p}_{I6} - \vec{p}_{I5} \end{bmatrix}$$

The solution for the internal pressures is,

$$\begin{bmatrix} \vec{p}_{I1} \\ \vec{p}_{I2} \\ \vec{p}_{I5} \\ \vec{p}_{I6} \end{bmatrix} = [\mathbf{DM_1} - \mathbf{M_2} + \mathbf{M_3}]^{-1}\vec{p}_0 \tag{2.4.19}$$

with,

$$M_1 = \begin{bmatrix} \mathbf{f}_{\mathbf{I11}} & 0 & \mathbf{f}_{\mathbf{I15}} & 0 \\ 0 & \mathbf{f}_{\mathbf{I22}} & 0 & \mathbf{f}_{\mathbf{I26}} \\ \mathbf{f}_{\mathbf{I51}} & 0 & \mathbf{f}_{\mathbf{I55}} & 0 \\ 0 & \mathbf{f}_{\mathbf{I62}} & 0 & \mathbf{f}_{\mathbf{I66}} \end{bmatrix} \tag{2.4.19a}$$

$$M_2 = \begin{bmatrix} \mathbf{f}_{\mathbf{EWW}}\mathbf{f}_{\mathbf{I11}} & \mathbf{f}_{\mathbf{EW0}}\mathbf{f}_{\mathbf{I22}} & \mathbf{f}_{\mathbf{EWW}}\mathbf{f}_{\mathbf{I15}} & \mathbf{f}_{\mathbf{EW0}}\mathbf{f}_{\mathbf{I26}} \\ \mathbf{f}_{\mathbf{E0W}}\mathbf{f}_{\mathbf{I11}} & \mathbf{f}_{\mathbf{E00}}\mathbf{f}_{\mathbf{I22}} & \mathbf{f}_{\mathbf{E0W}}\mathbf{f}_{\mathbf{I15}} & \mathbf{f}_{\mathbf{E00}}\mathbf{f}_{\mathbf{I26}} \\ 0 & 0 & 0 & 0 \\ 0 & 0 & 0 & 0 \end{bmatrix} \tag{2.4.19b}$$

$$M_3 = \begin{bmatrix} \mathbf{I} & 0 & 0 & 0 \\ 0 & \mathbf{I} & 0 & 0 \\ 0 & 0 & \mathbf{I} & -\mathbf{I} \\ 0 & 0 & -\mathbf{I} & \mathbf{I} \end{bmatrix} \tag{2.4.19c}$$

A multi-domain solution raises new challenges of topology when discretising and numbering the elements of the structure.

### 2.4.5 Coupling of Hydrostatic Loads

Hydrostatic pressure is ignorable for analysing a fully submerged structure since the buoyancy does not contribute to the structural dynamic when the total displacement is fixed. However, it is still significant for floating structures and it is necessary to develop a direct coupling procedure including the variation of hydrostatic pressure.

For direct coupling of the hydrostatic restoration force into the body motion, it is necessary to introduce a vertical displacement shift variable. For a steady state, oscillating body the hydrostatic pressure $P_S$ acting on the wetted surface satisfies,

$$P_S = -\rho g(Z_0 + \Delta z e^{-i\omega t}) \tag{2.4.20}$$

where the z-coordinate is $Z_0$ in the equilibrium state and $\Delta z$ is the vertical oscillation amplitude. Since the term $\rho g Z_0$ already contributes to the equilibrium of the structure, only $\rho g \Delta z e^{-i\omega t}$ is responsible for the oscillation. Clearly, we can cancel the harmonic component in the frequency domain analysis.

Assuming an invariant hydrostatic force over the $m^{th}$ element is ${}^{m}P_{SE}$, the (external) hydrostatic pressure function for the displacement $\overrightarrow{z_E}$, which is independent of $\overrightarrow{v_E}$, is

$$\overrightarrow{P_{SE}} = \mathbf{f_{SE}}\overrightarrow{z_E} \tag{2.4.21}$$

$$\overrightarrow{P_{SE}} = [{}^{1}p_{SE}, {}^{2}p_{SE}, {}^{3}p_{SE}, ..., {}^{N}p_{SE}]^T \tag{2.4.21a}$$

$$\mathbf{f_{SE}} = diag(\rho_E g, \rho_E g, \rho_E g, \ldots, \rho_E g) \quad \text{of size N} \tag{2.4.21b}$$

$$\overrightarrow{z_E} = [{}^{1}\Delta z_E, {}^{2}\Delta z_E, {}^{3}\Delta z_E, ..., {}^{N}\Delta z_E]^T . \tag{2.4.21c}$$

The above equations are analogous in form to Equation 2.2.27. The internal hydrostatic analysis follows the same procedure; however, one does not have to change the z-direction variable, as $\Delta z$ is a relative value. The hydrostatic analysis is necessary for a floating container model. However, we ignore hydrostatic pressure influences when the structure is balanced. For example, a submerged rigid body with coincident centres of gravity and buoyance or a floating container with $\rho_E = \rho_I$ and $h_0 = 0$.

When the hydrostatic force is not negligible Equations 2.4.2 for $\overrightarrow{v_E}$ become:

$$\overrightarrow{v_E} = \mathbf{U}(\mathbf{f_E}\overrightarrow{v_E} + \mathbf{f_{SE}}\overrightarrow{z_E} + \overrightarrow{p_0}) \tag{2.4.22a}$$

or,

$$\overrightarrow{v_E} = \mathbf{U}[(\mathbf{f_E} - \mathbf{f_I})\overrightarrow{v_E} + (\mathbf{f_{SE}} - \mathbf{f_{SI}})\overrightarrow{z_E} + \overrightarrow{p_0}]. \tag{2.4.22b}$$

It is clear, on appealing to Equation 2.4.20, that we require the additional relationships:

$$\overrightarrow{z_E} = \mathbf{U_z}(\mathbf{f_E}\overrightarrow{v_E} + \mathbf{f_{SE}}\overrightarrow{z_E} + \overrightarrow{p_0}) \tag{2.4.23a}$$

$$\overrightarrow{z_E} = \mathbf{U_z}[(\mathbf{f_E} - \mathbf{f_I})\overrightarrow{v_E} + (\mathbf{f_{SE}} - \mathbf{f_{SI}})\overrightarrow{z_E} + \overrightarrow{p_0}] \tag{2.4.23b}$$

where $\mathbf{U_z}$ is the matrix of boundary element displacements in the z-direction. We can determine this matrix simultaneously with $\mathbf{U}$, by replacing $\mathbf{n_m}$ with a unit z-direction

vector as described in Chapter 3. An i/ω multiplier of the solution converts velocities into displacements.

Combining Equations 2.4.22 & 2.4.23 yields:

$$\overrightarrow{v_E} = (\mathbf{I} - \mathbf{U}'\mathbf{f_E})^{-1}\mathbf{U}'\overrightarrow{p_0} \qquad (2.4.24a)$$

$$\mathbf{U}' = \mathbf{U}[\mathbf{I} + \mathbf{f_{SE}}(\mathbf{I} - \mathbf{U_z}\mathbf{f_{SE}})^{-1}\mathbf{U_z}] \qquad (2.4.24a')$$

and

$$\overrightarrow{v_E} = [\mathbf{I} - \mathbf{U}'(\mathbf{f_E} - \mathbf{f_I})]^{-1}\mathbf{U}'\overrightarrow{p_0} \qquad (2.4.25b)$$

$$\mathbf{U}' = \mathbf{U}\{\mathbf{I} + (\mathbf{f_{SE}} - \mathbf{f_{SI}})[\mathbf{I} - \mathbf{U_z}(\mathbf{f_{SE}} - \mathbf{f_{SI}})]^{-1}\mathbf{U_z}\}. \qquad (2.4.25b')$$

It should be noted that elements in $\mathbf{f_E}$ should be assigned zero, similar to the situation in Equation 2.4.13, when one side of the surface is dry and free from hydrodynamic or hydrostatic force.

# 3 Modelling

This chapter identifies boundary element and or finite element discretisation for a selected set of geometries and indicates the solution approach to be adopted. Chapter 4 presents the generated analysis results.

## 3.1 Models

### 3.1.1 Spherical Shell

We select a spherical shell for testing since it is the simplest geometry with many existing analytical or numerical studies. It is also a highly symmetric body, where modal analysis should fail.

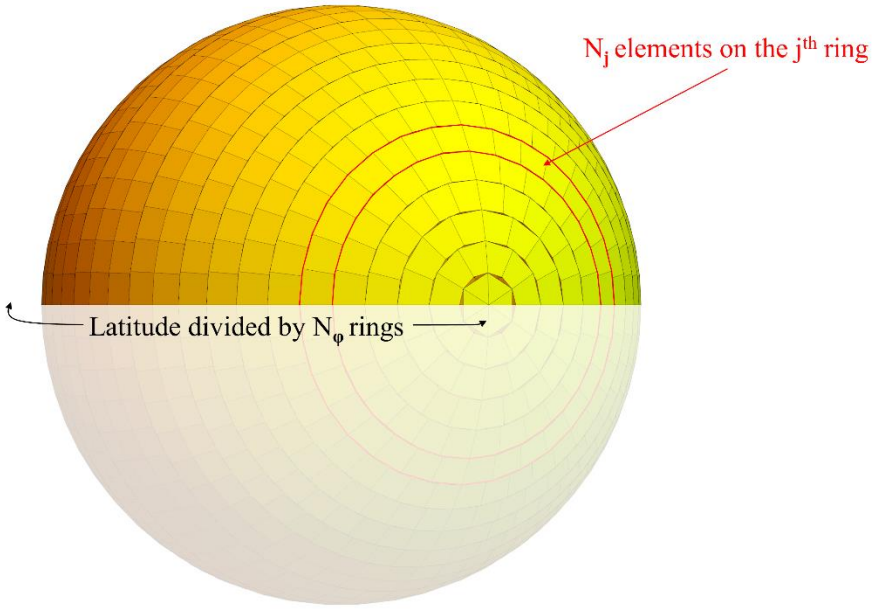


Figure 3.1 The boundary element mesh of a spherical geometry consists of $N_\varphi = 32$ rings of uniform latitude from pole to pole. Division of each ring ensures a boundary element geometric aspect ratio is evenly close to one. Gaps between the elements have negligible influence upon the overall calculation.

The boundary elements and finite elements are meshed differently according to the interpolation we introduced. Generally, the sphere is evenly meshed in latitude first,

and then each ring is divided uniformly. The vertices of the same element are on the same plane under this discretisation. Aspect ratio of the elements are close to 1 when discretised to avoid irregular geometry. The meshed models of Figures 3.1 & 3.2 consist of 1314 of boundary elements and 1372 finite elements. Each model comprises a mixture of triangular and quadrilateral elements.

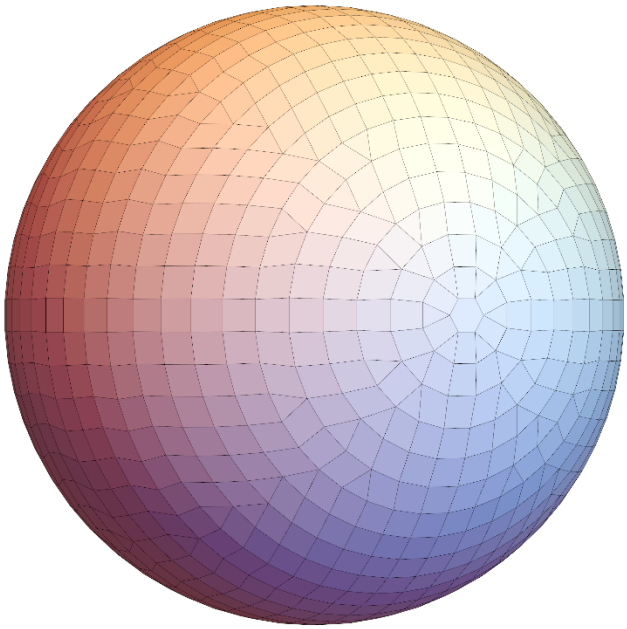

Figure 3.2 The finite element mesh of a spherical shell. The nodes of each element are the centroids of the corresponding boundary elements. No gap exists under this mesh.

We introduce MITC3 [71] and MITC4+ [72] elements for structural analysis, where shear locking and membrane locking is avoided.

### 3.1.2 Container & Natural Oscillation Analysis

In Section 2.2.2, the linear function set up for a resonant internal fluid oscillation problem indicated that natural resonant frequencies for a container required solution of $\det(\mathbf{f}_1) = 0$, or equivalently $\det(\widetilde{\mathbf{A}}) = 0$. For a vertical cylindrical container of radius $R_0$, there exists analytical solutions, which are the roots of (see Appendix A),

$$\frac{\partial J_n(\nu R)}{\partial R} = 0 \quad \text{on} \quad R = R_0 , \tag{3.1.1}$$

and ν is the variable of interest. In the equation, $R_0$ is the radius of the cylinder. The

solution of resonant wavelength is independent of container depth. The natural frequencies, though, are different according to dispersion relationship in Equation 2.1.10.

Table 3.1 The first five resonant frequencies of a vertical fluid filled cylindrical container of radius $R_0$ = 5m and the corresponding wavenumbers.

| Order | n | 1 | 2 | 3 | 4 | 5 |
|---|---|---|---|---|---|---|
| Resonant Wavenumbers | $\nu_n R_0$ | 1.841 | 3.054 | 3.832 | 4.201 | 5.331 |
| Wavelength | $\lambda$ (m) | 17.06 | 10.27 | 8.199 | 7.477 | 5.893 |

The singular value decomposition method identities the singularity of a matrix **M**. Here $\mathbf{M} \equiv \tilde{\mathbf{A}}$ for $\tilde{\mathbf{A}}$ defined by Equation 2.2.33. The matrix **M** is decomposed into three matrices **W, Σ** & **V*** multiplied to yield **M** = **WΣV***. **W** & **V*** are unitary matrices with determinants equal to one and multiplication of the trace of the diagonal matrix **Σ** provides det(**M**). Elements on the diagonal of **Σ** are designated singular values of **M.** If any of their value is zero then **M** is singular and the resonant frequencies are identified. Usually, the minimum singular value is close to rather than exactly zero, since **M** is determined numerically.

The two selected depths of the numerical container model are h = 7.5 m & 15 m. The analysis for two container depths should establish that $\nu_n$ for a vertical cylindrical container is not a function of cylinder depth. The container wall is meshed with N = 544 & 800 elements respectively. Figure 3.3 illustrates the discretization for the 7.5m depth container.

To address the resonance of a fully filled cylindrical container the appropriate solution method is the alternative formulation of described in Section 2.4.2. That is, applying the singular value decomposition method for matrix **L**. Natural vibration modes of the structure with incompressible fluid can be determined through eigenvalue decomposition. However, it still requires the manipulation of matrix $\mathbf{T_I}$ of Equation

2.4.8.

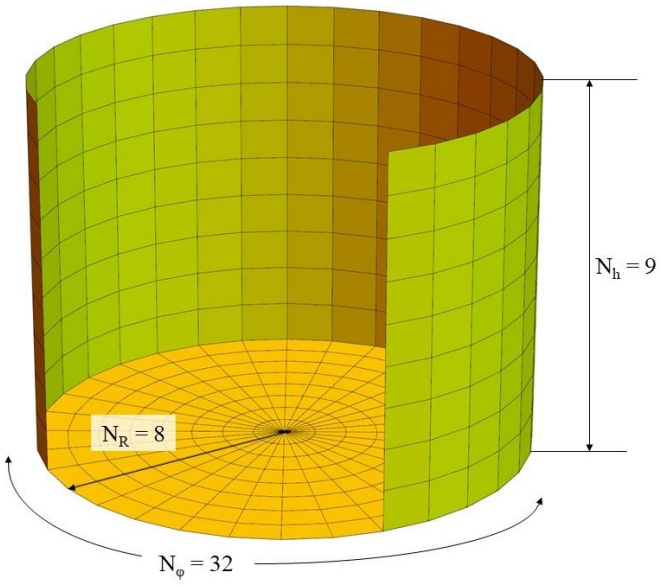


Figure 3.3 Discretization mesh for a vertical cylindrical container. Each parameter $N_S$ denotes the number of elements along container height, radius and circumference.

### 3.1.3 Forced Oscillation Model

The direct coupling method is very flexible. The fluid-structure interaction of a forced vibration problem can be appropriately formulated. Here an 'earthquake' model investigates the base of a cylindrical tower undergoing fixed amplitude vibration whilst surrounded by water with a free surface.

When part of the structure is under fixed oscillation, the normal velocity is known over the corresponding wetted surface. Let $\overrightarrow{v_k}$ and $\overrightarrow{v_u}$ denote the known and unknown motions in Equation 2.3.2 Next partition matrix $\mathbf{D}$ and $\vec{p}$ into portions associated with known and unknown motions, that is, Equation 2.3.2 becomes:

$$\begin{bmatrix} \mathbf{D_k} & \mathbf{X_D} \\ \mathbf{X_D^T} & \mathbf{D_u} \end{bmatrix} \begin{bmatrix} \vec{v}_k \\ \vec{v}_u \end{bmatrix} = \begin{bmatrix} \vec{p}_k \\ \vec{p}_u \end{bmatrix}. \tag{3.1.2}$$

Hence, $\overrightarrow{p_k}$ and $\overrightarrow{p_u}$ respectively represent the forces acting on the forced oscillating part and the reacting forces acting on the free nodes. The second row of this equation implies

$$\mathbf{X_D}^{\mathbf{T}}\vec{v}_k + \mathbf{D_u}\vec{v}_u = \vec{p}_u\,. \tag{3.1.3}$$

Hence $\overrightarrow{v_u}$ satisfies

$$\vec{v}_u = \mathbf{D_u^{-1}}\vec{p}_u - \mathbf{D_u^{-1}X_D}^{\mathbf{T}}\vec{v}_k \,. \tag{3.1.4}$$

When there is no known forced motions, only the first term on the right hand side of Equation 3.1.4 remains, which is the structural dynamic response when certain degrees of freedom are fixed. Similarly, the second term represents the boundary normal velocity due to forced vibration of the structure in vacuum, that is

$$\vec{v}_0 = -\mathbf{D_u^{-1}X_D^T}\vec{v}_k \,. \tag{3.1.5}$$

The excitation pressure $\overrightarrow{p_0}$ has been neglected since incident wave and other excitation forces are neglected in this problem (one may readily include them if necessary).

For rigid body motion, $\overrightarrow{v_0}$ can be determined through the kinematic analysis procedure of Section 2.2.2. The determination of matrix **U** is unchanged provided the forced part of the structure is fixed.

Matrix $\mathbf{f_E}$ is distinct for specified forced normal velocities on certain boundary elements. Let $\overrightarrow{v_k}$ be the known boundary motions then partitioning matrices in Equation 2.3.28, as in Equation 3.1.2 implies:

$$\begin{bmatrix} \overrightarrow{p_{Ek}} \\ \overrightarrow{p_{Eu}} \end{bmatrix} = \begin{bmatrix} \mathbf{f_{Ek}} & \mathbf{X_{FE}} \\ \mathbf{X_{FE}^T} & \mathbf{f_{Eu}} \end{bmatrix} \begin{bmatrix} \overrightarrow{v_{Ek}} \\ \overrightarrow{v_{Eu}} \end{bmatrix} \tag{3.1.6}$$

Thus, the functions relating unknown pressure and normal velocities becomes:

$$\overrightarrow{p_{Eu}} = \mathbf{f_{Eu}}\overrightarrow{v_{Eu}} + \mathbf{X_{FE}^T}\overrightarrow{v_{Ek}} \tag{3.1.7}$$

So the dynamic equation eventually become:

$$\overrightarrow{v_E} = \mathbf{U_u}(\mathbf{f_{Eu}}\overrightarrow{v_{Eu}} + \mathbf{X_{FE}^T}\overrightarrow{v_{Ek}}) + \overrightarrow{v_0} \tag{3.1.8}$$

The solutions are respectively,

$$\overrightarrow{v_E} = (\mathbf{I} - \mathbf{U_u f_{Eu}})^{-1}(\mathbf{U_u X_{FE}^T}\overrightarrow{v_{Ek}} + \overrightarrow{v_0}) \tag{3.1.9}$$

To verify this procedure, model a vertical cylindrical beam the same as used in the study of Liaw [73]. The determination of Matrix **U** uses the logic introduced in Section 2.3.3.

In the Liaw's study, the beam is of height 30.48 m, the fluid depth assumed. The ratio of tower radius to tower height is $R_s/H_s = 0.05$ and the wall thickness to radius ratio is

$t_s/R_s$ = 0.2. The tower material is concrete of density $\rho_s$ = 2483 kg/m$^3$ and Young's Modulus E = 34.47 GPa. The surrounding fresh water is of density $\rho_w$ = 1000 kg/m$^3$.

Vibration modes of the first two orders were analysed. The two structural modal damping ratio are the same and equal to 0.05 for both modes. The Rayleigh definition of structural damping ratio is based, that is,

$$C = a_1 M + a_2 K \tag{3.1.10}$$

in which the coefficients $a_1$ and $a_2$ are introduced to determine the damping coefficient of n$^{th}$ vibration modes according to,

$$\varsigma_n = \frac{a_1}{2\omega_n} + \frac{a_2 \omega_n}{2} \tag{3.1.11}$$

Here $\varsigma_n$ is the damping coefficient for n$^{th}$ order vibration and $\omega_n$ is the n$^{th}$ order natural frequency.

The structural response of interest is the acceleration at the top of the cylindrical tower, designated $a_Y$.

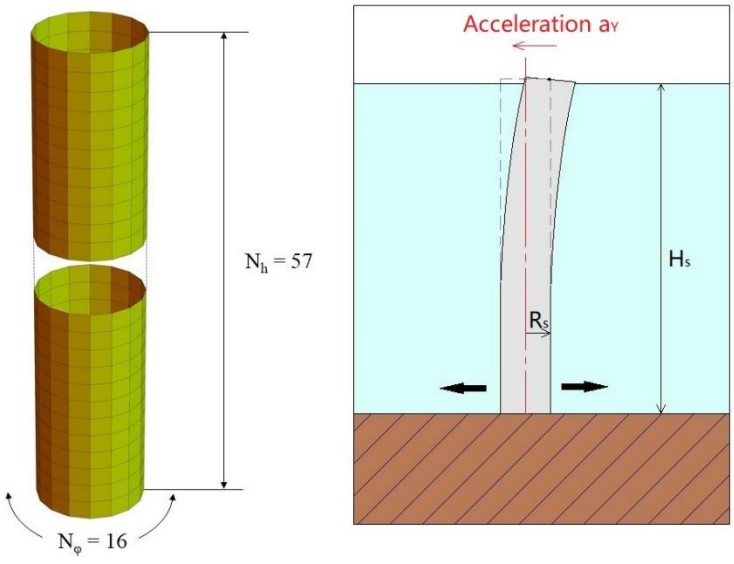


Figure 3.4 The mesh and earthquake model for a vertical cylindrical beam surrounded by water and shaken transversely at constant amplitude at its base. The number of radial and transverse boundary elements are 16 & 57 respectively.

Figure 3.4 indicates the number of cylindrical and vertical boundary elements the

wetted wall and defines various quoted dimensional parameters. Since the tower base and top are not in contact with the water, no boundary elements are necessary at these locations.

### 3.1.4 Anaconda model

The tube modelled here is a combination of circular cylinder and hemispherical caps. In real practice, the ends of the Anaconda are supposed to be stiff compared to the rubber to hold the power take-off system. Since it is not feasible to model such a complex system and the rigid ends may result in zero flux at the terminal cross section, the material is uniform throughout the boundary.

A measuring plane is selected at the end section of the cylinder to calculate the pressure and the flux striking the power take off system, (See Figure 3.5).

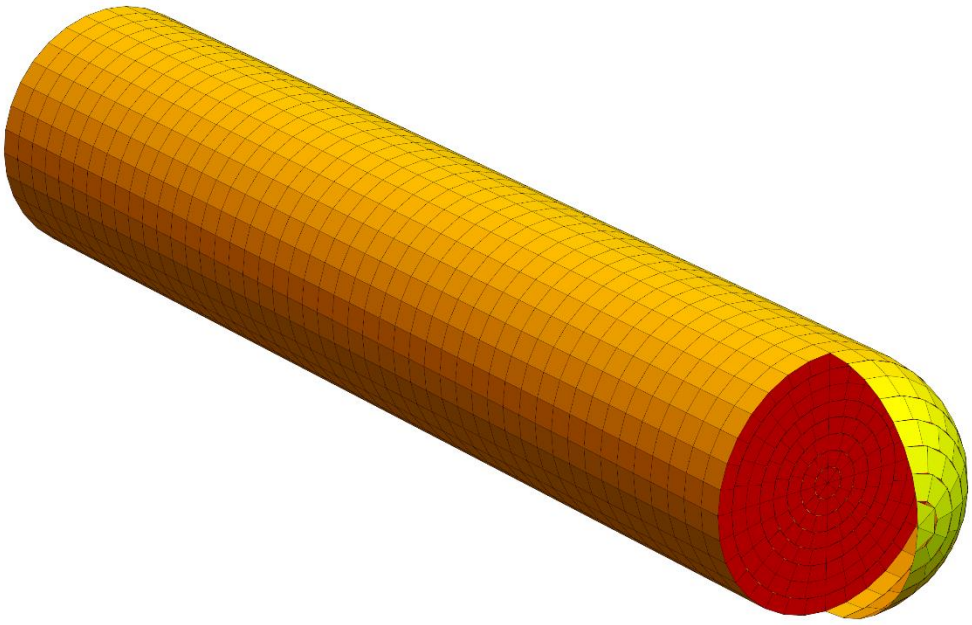

Figure 3.5 The boundary elements at the ends of the Anaconda model (yellow). Red plane is the cross section for calculation pressure and flux at the end of the tube. There are 4748 boundary elements in a single model of diameter d = 7 m and length $L_0$ = 94.2 m when $N_\varphi$ = 32.

Upon determine the normal velocity and the pressure across a surface, the average energy flux Π through the surface is,

$$\Pi = \iint_S \left( \int_0^T \frac{p(t) \cdot v(t)}{T} dt \right) dS \tag{3.1.12}$$

For a system under harmonic oscillation, the average power take off is,

$$\Pi = \frac{1}{2} \iint_S \mathrm{Re}(p \cdot v) dS \tag{3.1.13}$$

The energy flux of a propagating wave of infinite water depth per meter is,

$$\Pi_w = \frac{\rho g^2 A_w^2}{16\omega} \tag{3.1.14}$$

The capture width is defined by,

$$C_W = \frac{PTO}{\Pi_W} \tag{3.1.15}$$

Figure 3.6 provides the finite element mesh for Anaconda.

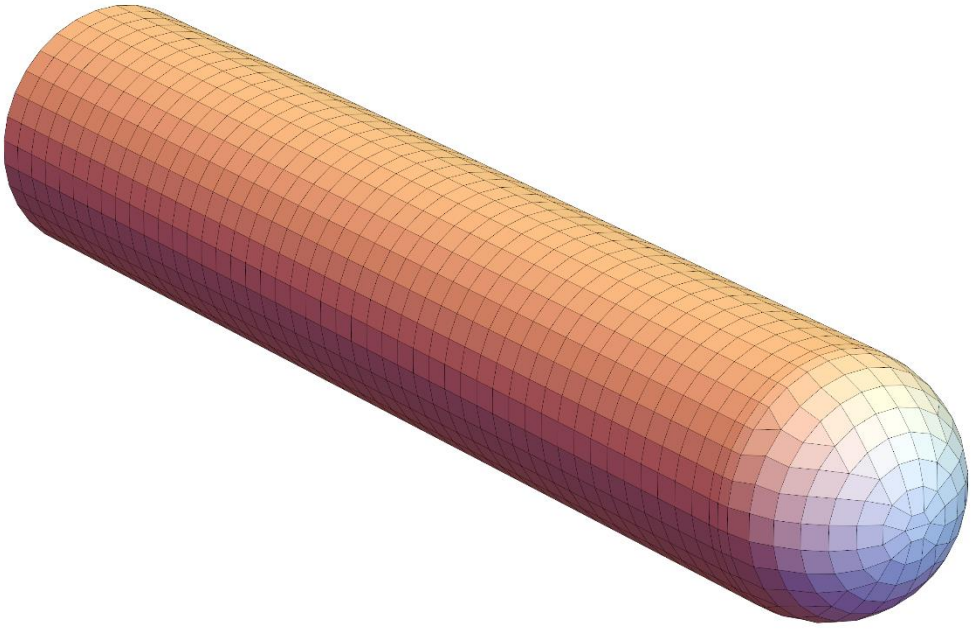

Figure 3.6 The finite elements at the ends of the Anaconda model. There are 4836 boundary elements in a single model of diameter d = 7 m and length $L_0$ = 94.2 m when $N_\varphi$ = 32.

Since the flexible end impede the flow passing through the last cross section, we delete the end cap when analysing the energy flux passing through the measuring plane.

Instead, a fictional impedance is uniformly attributed over the last cross section to simulate the turbine resistance. From previous studies, the impedance in a bulge wave is,

$$Z = \frac{\rho c_w}{A_s} \tag{3.1.16}$$

This corresponds to when unit flux is passing through the cross section. The value of the artificial impedance Z' to be introduced should be of this order.

When impedance is zero, the problem reduces to a half-closed problem introduced in Section 2.4.3. The zero trace in the dynamic matrix of Equation 2.4.13 needs to be replaced by $Z'A_s$ to address the pressure generated by unit normal velocity through the boundary.

### 3.1.5 Induced Profile

To have a clear sense of resulting diffraction and radiation waves, water surface profiles induce by the influenced of the body are calculated and visualised in this study. There are two ways for determining the wave profile.

From Equation 2.1.6, the time-independent profile can be determined from the wave potential $\phi$ according to,

$$\eta = \frac{i\omega\phi}{g} \tag{3.1.17}$$

Hence, whether considering diffraction or radiation, one needs to derive $\phi$ at the free surface according to the results we have solved on the boundary of a rigid body. For an arbitrary point P lying in the fluid domain, the value of $\phi$ at that point according to the second identity of Green is.

$$\phi(P) = \frac{1}{4\pi}\iint_{S_W}(\phi\frac{\partial G(P)}{\partial n} - G(P)\frac{\partial \phi}{\partial n})dS \tag{3.1.18}$$

where G(P) denotes evaluation of the Green function sourced at P. Since we have discretised the wetted surface $S_W$ into N boundary elements, we can calculate $\phi$(P) approximately according to,

$$\phi(P) = \frac{1}{4\pi}\sum_{j=1}^{N}\phi_j \iint_{S_{Wj}} \frac{\partial G(P)}{\partial n} dS - \frac{1}{4\pi}\sum_{j=1}^{N}\left(\frac{\partial \phi}{\partial n}\right)_j \iint_{S_{W_j}} G(P) dS \qquad (3.1.19)$$

Here j refers to the corresponding number of the element. If we let P be infinitesimally close to the free surface, the calculated value of water profile will be sufficiently accurate.

This procedure is straightforward as $\phi$ and its normal derivative on each element are already determined in the previous steps. Alternatively if we discretise a region of free surface of interest into M elements, the workload to draw the profile will be of the order of O(N·M).

The other method assumes that the resulting diffraction or radiation potential field is a result of 1st order free surface multipole (free surface Green function) spreading over the wetted surface. The source strength is expressed by a density function $\sigma$ and the value of $\phi(P)$ is calculated according to

$$\phi(P) = \iint_{S_W} \sigma G(P) dS \qquad (3.1.20)$$

By assuming $\sigma$ is uniform over a single element, $\phi(P)$ can be derived by,

$$\phi(P) = \sum_{j=1}^{N} \sigma_j \iint_{S_W} G(P) dS \qquad (3.1.21)$$

The unknown in this procedure is the value of $\sigma_j$ and this is determinable from known values of $\phi(P)$ obtained on the wetted surface of the selected structure. By setting such relationship over each element, one will be able to set up N linear equations with N unknowns and to solve this set of equations through matrix inversion. The matrix set up for solving $\phi(P)$ will be exactly the same as the matrix **B** we obtained in Equation 2.2.25. However, this matrix must be inverted and be multiplied by the list vector of $\phi$. The workload of these steps would be in $o(N^3)$ order plus an o(N·M) workload to draw the profile.

The results generated from these two methods are very close. The first method is applied because it is effective and appears to be more accurate at the far field.

## 3.2 Programming

### 3.2.1 Special Functions

Principal value integration in Equation 2.2.6 is not trivial because it involves calculation near singularities and the upper limit of integration is infinite. An alternative expression for this integration, denoted as $I_g$ in the following section, is required to avoid overflow and low efficiency evaluation.

According to Hearn [52], $I_g$ is mathematically transformable to the following expression,

$$I_g = \nu e^{\nu(z+c)}\{\frac{1}{\nu R} - \pi[H_0(\nu R) - Y_0(\nu R)] - \int_0^{-\nu(z+c)} \frac{se^s ds}{(s^2+\nu^2R^2)^{3/2}} - \int_0^{-\nu(z+c)} \frac{e^s ds}{(s^2+\nu^2R^2)^{1/2}}\} \quad (3.2.1)$$

in which $H_0(x)$ is the Struve function of $0^{th}$ order. Hearn also provides the x, y and z partial derivatives. The Struve function derivatives involve the $1^{st}$ order Struve functions designated $H_1(x)$.

To simulate the Struve function, Newman [74] suggested Chebyshev polynomial expansions. The accuracy of this approximation is to an order of $10^{-8}$ decimal. It takes less computing time compared with other approximation methods.

Two special cases also considered when calculating the numerical results of $I_g$, that is, when $\nu = 0$ & $R = 0$.

For $\nu = 0$, note that $I_g$ reduces to,

$$I_g = PV\int_0^{\infty} e^{k(z+c)} J_0(kR)dk \quad (3.2.2)$$

As (z + c) is negative throughout the fluid domain, this expression is equivalent to a Laplace transform of $J_0(kR)$ dependent on the variable (z + c), that is,

$$I_g = \frac{1}{\sqrt{(z+c)^2+R^2}} = \frac{1}{r_1} \quad (3.2.3)$$

This corresponds to a contribution from an image source. It is also clear that the imaginary part of free surface Green function is zero when $\nu = 0$. Hence, this result shows that the free surface should reduce to a rigid wall when the frequency of the

oscillation goes to zero in infinite depth water. It is physically realistic as the velocity under such condition should be very slow.

For R = 0, the original integral formulation becomes,

$$I_g = PV\int_0^\infty \frac{k+\nu}{k-\nu} e^{k(z+c)} dk \tag{3.2.4}$$

By introducing exponential integral,

$$\mathrm{Ei}(x) = \int_{-x}^{\infty} \frac{e^{-t}}{t} dt \tag{3.2.5}$$

$I_g$ assumes the form,

$$I_g = -\frac{1}{z+c} - 2\nu e^{\nu(z+c)} Ei[-\nu(z+c)] \tag{3.2.6}$$

Its partial derivative in the z direction can be readily deduced whereas the R-direction derivative requires differentiation of the Bessel function $J_0(\nu R)$ with respect to R first. This will result in $J_1(x)$ in the integration and this is zero when x = 0. Hence, we have $\partial I_g/\partial R = 0$ when R = 0.

The function of Ei(x) is not generally implemented in many compilers. Therefore the Boost Package of the C++ language is used to evaluate this function.

In the real implementation of codes, a regular value of Ig is numerically difficult when $\nu R < 0.005$. To solve this challenge, linear interpolation between $\nu R = 0$ point (solved by Equation 3.2.6) and $\nu R = 0.005$ point (solved by Equation 3.2.1) is undertaken.

For the imaginary parts of the free surface Green function, Bessel functions are readily evaluated via the Visual Basic compiler.

By applying the appropriate evaluations described, we can assign the integration of regular parts of G on each boundary element by first calculating the corresponding values at the centroid of the facet and then multiply it with the area of the associated boundary element. The value of $I_g$ is directly calculable whilst $\partial I_g/\partial n$ is determined in accordance with,

$$\frac{\partial I_g}{\partial n} = \vec{n} \cdot (\frac{\partial I_g}{\partial x}, \frac{\partial I_g}{\partial y}, \frac{\partial I_g}{\partial z}) \tag{3.2.7}$$

where $\vec{n}$ is the normal vector on the surface pointing into the body.

The surface integration of singular parts 1/r & $\partial(1/r)/\partial n$ can be determined from the analytical proposals of Hess & Smith [75] and Garrison & Chow [76] respectively.

### 3.2.2 Computation

Besides application of the Boost Package for special functions, the Armadillo library by Sanderson & Curtin [77] provides efficient operation of complex matrices. The operation of regular complex numbers are also under this package.

For a non-sparse matrix of 1,000 by 1,000 size, it takes about 20 s to derive its inverse, which is efficient enough for the direct coupling method. It is even more efficient when Visual Studio 2017 compiler's OpenMP parallel computing is applied.

The most challenging computational problem is the heavy occupation of memory when large matrices require large storage and calculation. The available 24 G memory is usually insufficient or running 8 thread simultaneously.

# 4 Result for General Problems

Having indicated different fluid-structure interaction scenarios and their modelling in the previous chapter, results are presented of the analysis of each.

## 4.1 Internal Free Surface Flow

I t is necessary to properly demonstrate its validation through simulation of internal free surface flows through application of the boundary element analysis proposed in Section 3.2.2, before presenting results demonstrating the full t coupling. In particular, verification of the prediction of free surface flow in a cylindrical container.

### 4.1.1 Analysis on Cylindrical Container

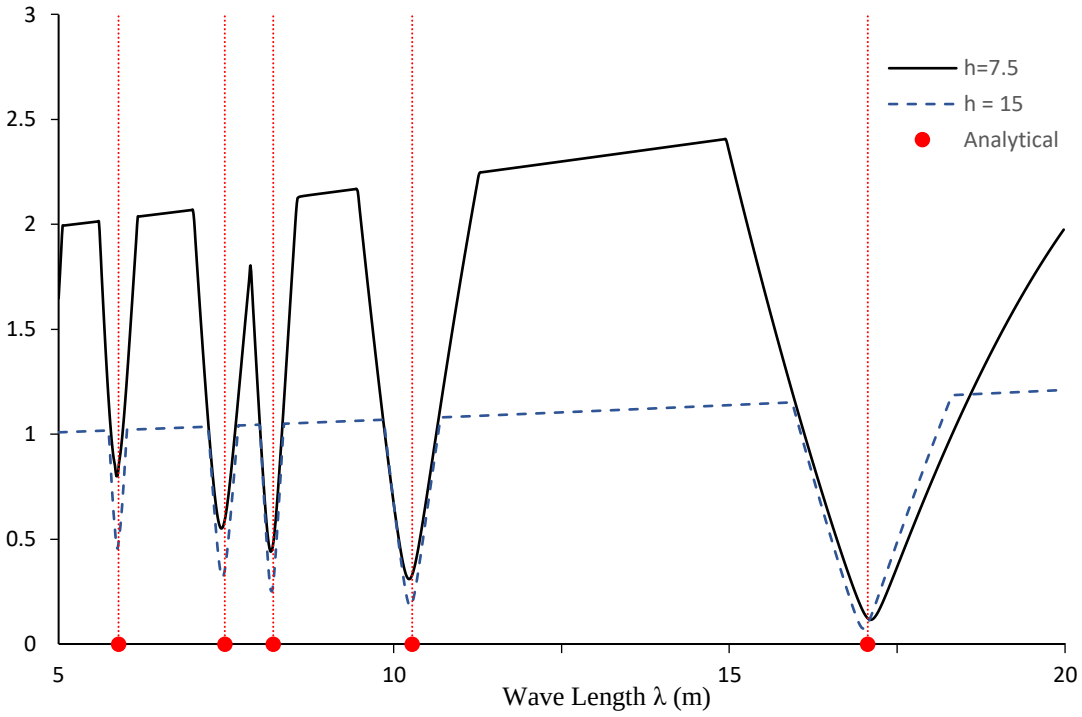


Figure 4.1 Minimum singular values of matrix $\tilde{\mathbf{A}}$ as a function of wavelength λ for two cylindrical fluid filled containers. The dots on the λ axis are the analytical determined resonant wavelengths.

The minimum singular value of $\tilde{\mathbf{A}}$ of Section 3.1.2 is investigated for wavelengths between 5 m and 20m in wavelength increments of 0.02 m, Totalling 750 wavelength

values they address the full range of analytical resonant natural frequencies of Equation 3.1.1 identified in Table 3.1. Figure 4.1 presents the numerically identified minimum singular values of $\tilde{\mathbf{A}}$ for both container heights.

As Figure 4.1 indicates, the minimum singular value of $\tilde{\mathbf{A}}$ drops significantly around the analytical frequencies predicted in Table 3.1 for both container depths. This means that $\tilde{\mathbf{A}}$ set up for an internal fluid analysis is capable of identifying the resonant wavelengths determined analytically and it is feasibility to model the internal fluid physically when the system is subjected to regular wave frequency. Near resonance, the linearized free surface condition breaches and high order analysis of the fluid motion is required.

### 4.1.2 Analysis on Hemispherical Container

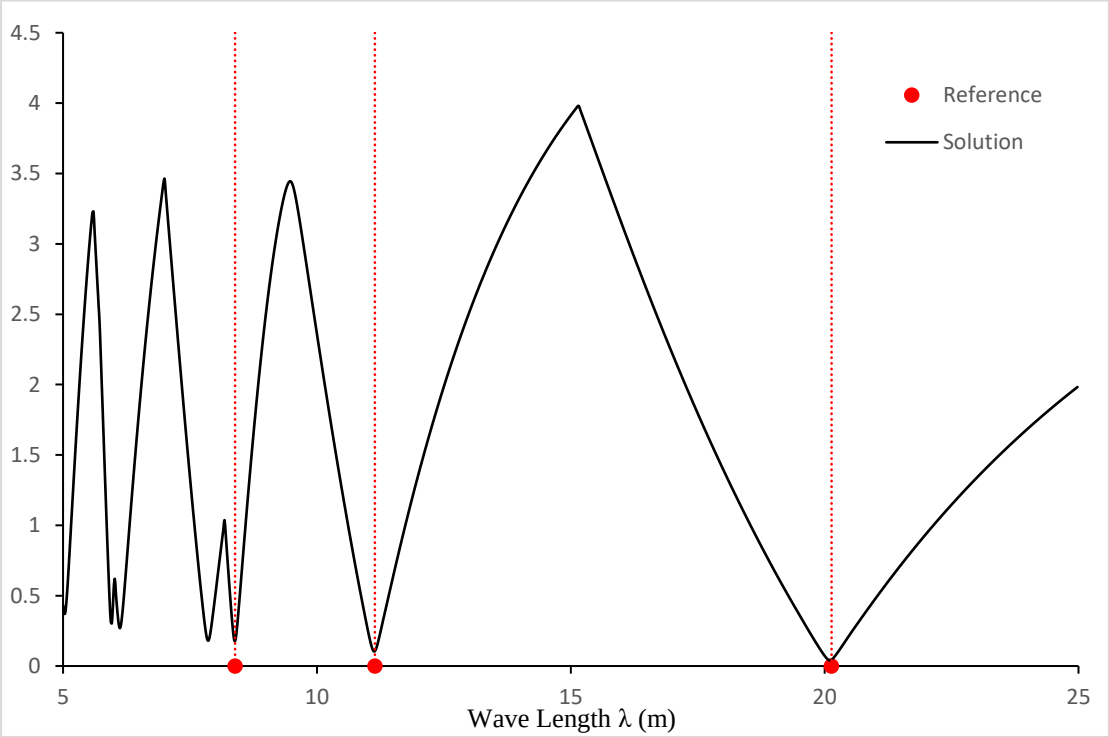


Figure 4.2 The hemispherical container's singular values of matrix $\mathbf{f_I}$ as a function of λ. Dots indicates the solution by Evans & Linton [78], in which only the first 3 resonant wave length are able to be included in the plot. Additional natural oscillation frequencies are predicted.

A half-filled hemispherical container of radius 5 m replaces the fluid filled cylinder of Section 2.3.2. The predictions of Evans & Linton [78], who analysed the same

hemispherical model through an expansion method for the first three azimuthal modes, provide verification of the minimum singular value based predictions. Meshing of the hemisphere leads to 828 boundary elements, 36 elements circumferentially model the internal free surface circumference.

Again, the singular values of $\mathbf{f}_I$ are sought for a range of wavelengths. The singular values identified from Figure 4.2 correspond to wavelengths (λ) of 8.38, 11.12 and 20.10 m. These in turn provide non-dimensional wavenumbers $\nu_n R_s$ equal to 3.749, 2.825 and 1.563.

Table 4.1 The first three non-dimensional resonant wavenumbers of half-full spherical container predicted by Evans and Linton and the authors' boundary element analysis.

| Order | n | 1 | 2 | 3 |
|---|---|---|---|---|
| Non-dimensional natural wavenumbers $\nu_n R_s$ | Expansion Method | 1.560 | 2.820 | 3.745 |
| | Boundary Analysis | 1.563 | 2.825 | 3.749 |

Comparing Figures 4.1 and 4.2, the singular nature of $\mathbf{f}_I$ for cylinder and hemisphere is quite distinct. The longer wavelength associated singular points for the hemisphere are obvious and in general, there is greater sensitivity to wavelength variation.

## 4.2 Coupling of Rigid Shell

This application provides verification of the direct coupling equation in the simplest form of Equation 2.4.1. A rigid floating container with internal free surface flow excited by external waves is analysed to demonstrate the proper coupling of hydrostatic force and hydrodynamic force.

### 4.2.1 Particle Motion

The simplest direct coupling model is a solid rigid sphere subjected to incident wave motion. Furthermore, for an extremely small sphere radius the sphere motion should

mimic that of a water particle.

Analytical expressions for the horizontal (x) and vertical (z) velocities of a fluid particle in an incident wave with infinite water depth satisfy:

$$|u_x| = |u_z| = \omega A_w \exp(vz) \ . \quad (4.2.1)$$

Table 4.2 The velocity of particles (very small spherical shells) solved through different method in certain depths and directions. Truncated error in the results are only shown as an order of magnitude

| Depth z (m) | Direction | Value | Direct Solution (m/s) | Solid Body Analysis (m/s) | Analytical Solution (m/s) |
|---|---|---|---|---|---|
| 0.5 | x | Real | $o(10^{-12})$ | $o(10^{-13})$ | 0 |
| | | Imaginary | 0.645000 | 0.642212 | 0.645438 |
| | z | Real | 0.643251 | 0.645438 | 0.645438 |
| | | Imaginary | $o(10^{-12})$ | $o(10^{-11})$ | 0 |
| 1.0 | x | Real | $o(10^{-11})$ | $o(10^{-13})$ | 0 |
| | | Imaginary | 0.580872 | 0.578361 | 0.581267 |
| | z | Real | 0.579297 | 0.581266 | 0.581267 |
| | | Imaginary | $o(10^{-11})$ | $o(10^{-12})$ | 0 |
| 2.0 | x | Real | $o(10^{-10})$ | $o(10^{-13})$ | 0 |
| | | Imaginary | 0.471110 | 0.469073 | 0.471430 |
| | z | Real | 0.469832 | 0.471429 | 0.471430 |
| | | Imaginary | $o(10^{-12})$ | $o(10^{-12})$ | 0 |

In the numerical analysis the sphere radius $R_s = 0.005$ m. Its behaviour is investigated at the submerged depths of z = 0.5, 1.0 & 2.0 m. The density of the sphere is equal to the water density so the sphere is at equilibrium suspension in still water.

The incident wave amplitude is $A_w = 0.5$ m and the selected wavelength is $\lambda = 30$ m. The direct numerical solutions of $u_x$ and $u_z$ are compared with the analytical results of

Equation 4.2.1 in Table 4.2.

Theoretically, fluid particles free of Stokes' higher order effect move in exact circular loci of depth dependent radii in a large depth water wave. Table 4.2 indicates that the direct coupling method presents accurate velocity magnitudes when compared to the analytical results generated from Equation 4.2.1. Figure 4.3 confirms the phase shift is physically correct when particle motion is visualised with the variation of the free surface waves.

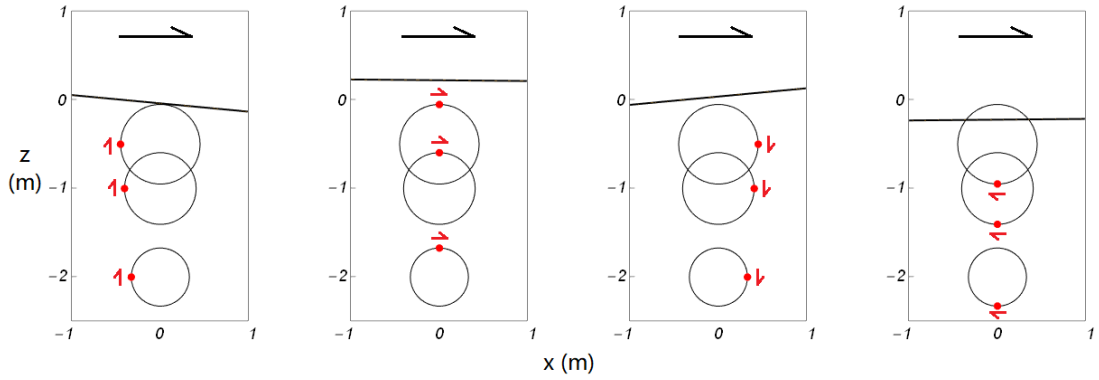


Figure 4.3 Locations of particle models (red points) at different phases. Circles are the tracks of the particle and arrows indicate the direction of velocities. ($\varphi = 0, \pi/4, \pi/2, 3\pi/4$ from left to right)

### 4.2.2 Rigid Container

Here we present comparison of three distinct sets of heave and surge response predictions of a sphere with internal and external free surfaces.

Initially an externally progressing incident wave of amplitude 0.5 m and varying frequency excites a half-full spherical container. Infinite external water depth applies.

In a comparative situation a rigid spherical shell of thickness $t_s = 0.01$ m has the same density as the internal and external water ($\rho_w = 1000$ kg/m$^3$). The sphere is half- filled with fluid and its equatorial circumference is essentially coincident with the undisturbed free surface. The fluid-structure interaction formulation utilizes Equations 2.3.8.

The third scenario has a half-floating solid sphere with same radius and structural density $\rho_s = 500$ kg/m$^3$. Application of Equation 2.4.22a models this scenario. Newman

[13] uses 3-dimensional classical radiation-diffraction analysis for infinite water depth and wave numbers less than 3.

Figure 4.4 provides predicted heave motion amplitude made non-dimensional with respect to incident wave amplitude. Figure 4.4 indicates resonance occurrence for the wavenumber $\nu_n R_s$ approaching unity in all three analyses. All three transfer-functions are in close agreement, indicating that the internal fluid generally has relatively no influence upon the heave response.

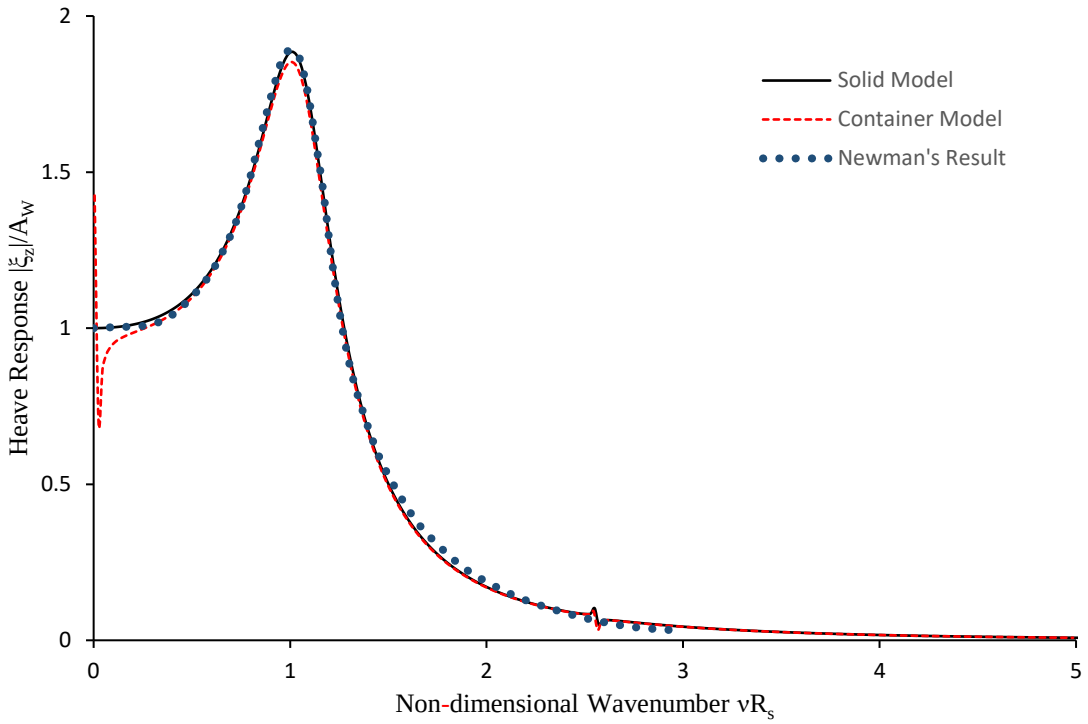


Figure 4.4 Heave responses of half-floating hemispherical models.

For low frequency (low wavenumber) excitation, the internal fluid seems responsible for the solution not satisfying the physically expected $|\xi_z|/A_W \rightarrow 1$ illustrated in the standard Newman analysis. At low frequencies (wavenumber), the internal fluid model will be highly sensitive to the evaluation resolution of the regular part of the Green function $G_r$. Thus, influencing the sensitivity / accuracy of matrix $\mathbf{f_E}$. The slight blip in heave response at $\nu R_s = 2.59$ is not a result of analysis failure but an occurrence of an irregular frequency. Irregular frequencies are a frequent occurrence in the boundary element analysis for floating structures [79, 80]. Newman's result has avoided its

influence by applying corrected added mass and damping coefficients in the analysis. The peak heave amplitude of 1.89 times wave height is acceptable for a half-floating sphere model. Heave, like pitch, has a resonant response controlled by structural mass and the hydrostatic restoration influenced. The latter influenced here by the large horizontal circular water plane at the undisturbed free surface.

Figure 4.5 indicates that the surge response of the half-floating spherical container is significantly different from the solid sphere.

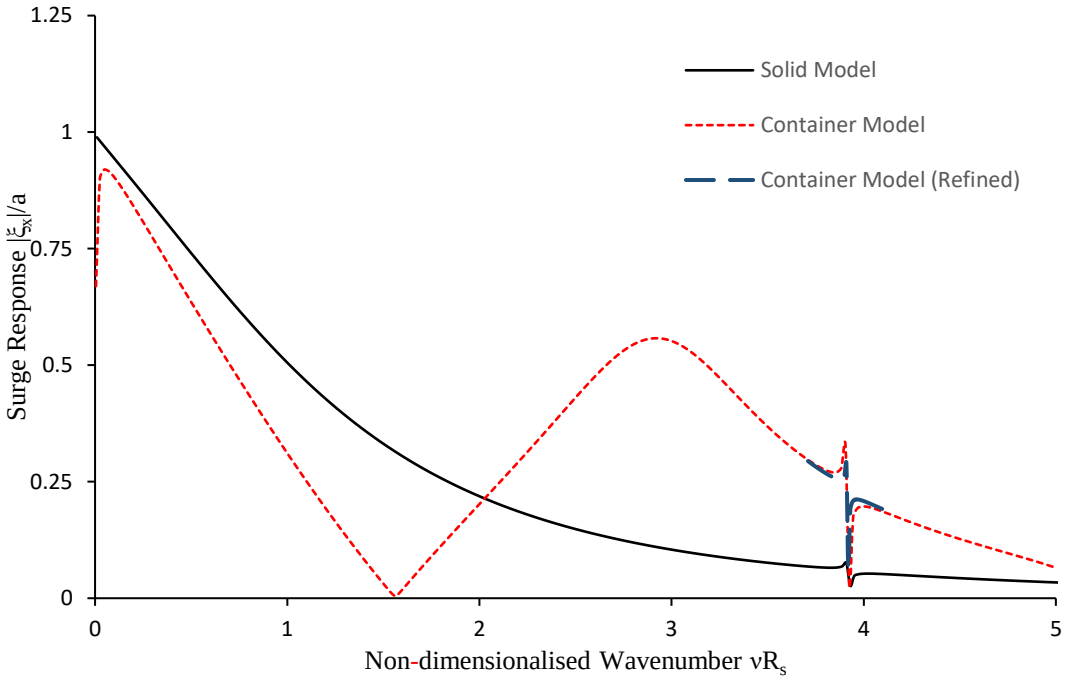


Figure 4.5 Surge responses of half-floating hemispherical models.

When the sphere heaved, the internal fluid could oscillate vertically too. However, here the sphere moves back and forth in the horizontal plane and Figure 4.5 shows the significant influence of the behaviour of the internal fluid. The internal fluid, rather than the spherical shell, changes the centre of mass when external forces act on the structure. When the internal fluid reaches resonance at $\nu R_s = 1.56$ (a value identified in Table 4.1), the internal reaction force becomes arbitrarily large since matrix $F_E$ is now singular and the motion of the structure is stopped. The reaction is physical provided the linear assumption holds.

Like heave, the surge model is irregular when wave frequency (wavenumber) approaches zero. Furthermore, an irregular frequency appears at about $\nu R_s = 3.92$ in the surge motion. Its impact on the solid model is less significant than the impact on the container model.

Unlike multipole approaches, based on meeting specified boundary conditions via a collocation process, the Fredholm integral equation formulation, underpinning the standard rigid body radiation-diffraction boundary element analysis at zero and forward speed, often exhibit irregular frequencies. Irregular frequencies in radiation analysis often affect the added mass / inertia and fluid damping coefficients and hence motion responses. A pragmatic engineering analysis usually removes their negative impact by judicious smoothing each coefficient curve to remove the unnatural spikes in the predicted values.

### 4.2.3 Visualised Phenomenon

Newman's analysis treats the internal mass as part of the total mass-inertia characteristics of the spherical structure. The coupled analysis allows the investigators to examine the relative motion of both internal and external free surface motions relative to the structural motion.

This application was completed for wavelengths of 60m, 30m and 15m, corresponding to $\nu R_s = 0.52$, 1.05 & 2.09 for phase $\omega t$ equal to 0, $\pi/2$, $\pi$ and $3\pi/2$ designated cases (a) to (d) respectively for each wave length. For the lower non-dimensional wavenumber, the internal & external free surfaces are completely in phase throughout a wave cycle, see Figure 4.6. For resonant heave at a non-dimensional wavenumber of 1.05, Figure 4.7 indicates there is a clear vertical shift between internal and external free surfaces. For non-dimensional wavenumber of 2.09, Figure 4.8 suggests the external wave is significantly diffracted and the internal free surface experiences higher order modes. Figure 4.9 provides 3D illustrations of the natural oscillation modes of the internal fluid excited by wavelengths of 60 m and 15 m. The first and second order modes dominate.

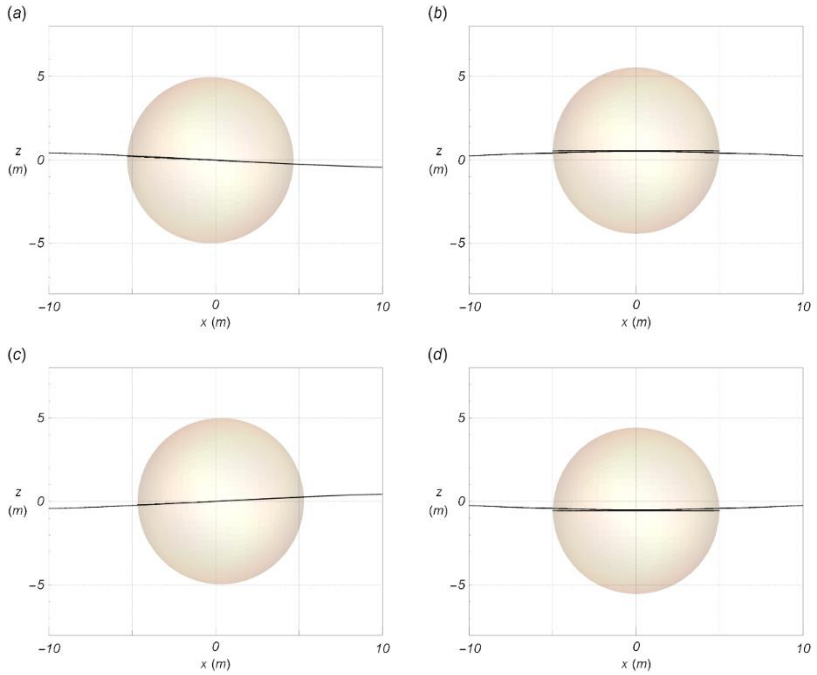


Figure 4.6 The side view (looking from - y axis) of a half-floating container model when the excitation wave frequency is low (λ = 60 m). The internal and external free surface are almost coincident throughout.

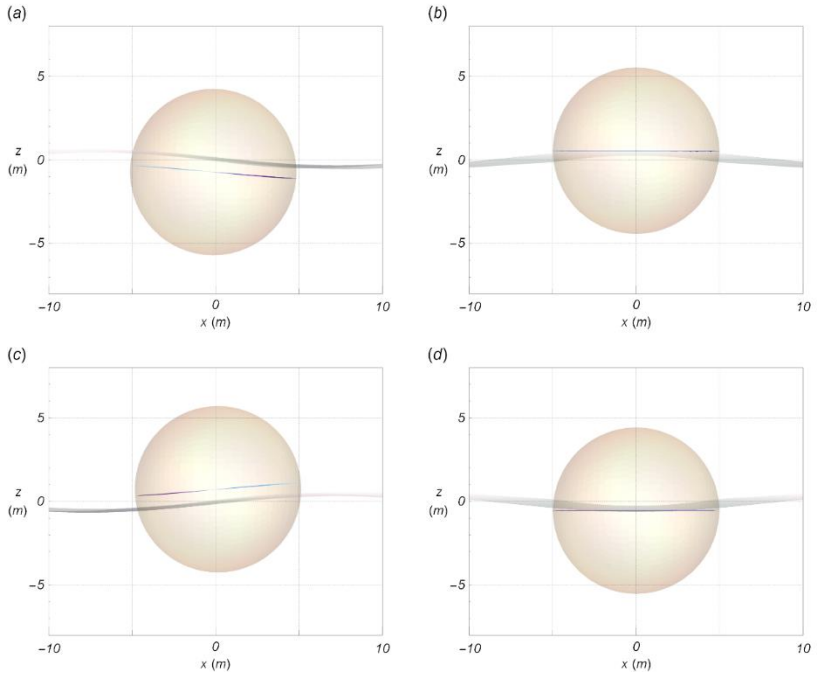


Figure 4.7 The side view of a half-floating container model when the excitation wave frequency is close to the natural oscillation frequency of heave motion (λ = 30 m). The internal free surface is distinct from external free surface due to heave resonance.

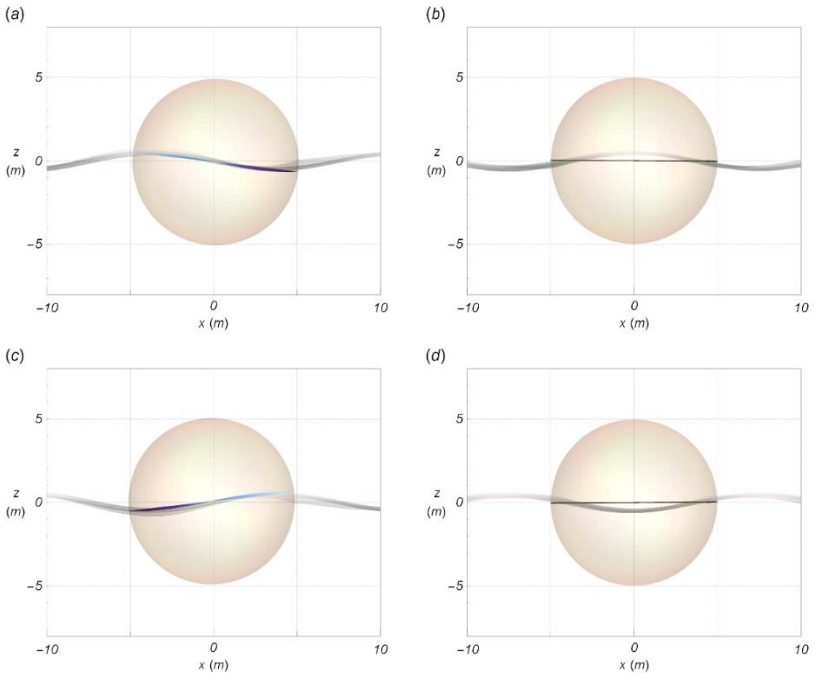


Figure 4.8 The side view of a half-floating container model when the excitation wave frequency is high (λ = 15 m). High order modes appear for the internal fluid while the external wave is diffracted significantly.

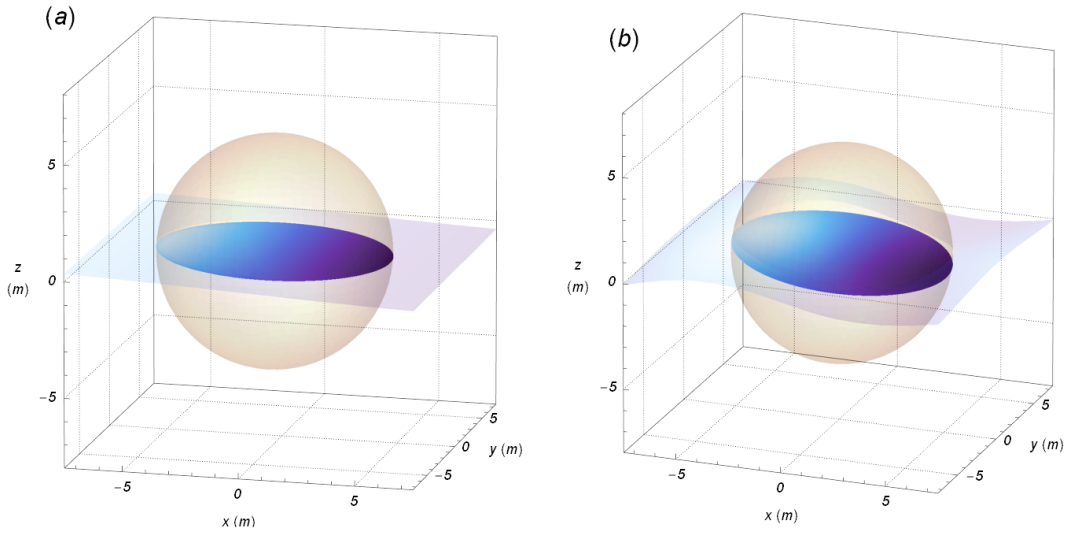


Figure 4.9 The internal free surface at time ωt = 0 when the half-floating spherical container experience in (a) an incoming wave length of λ = 60 m and (b) in λ = 15 m.

## 4.3 Coupling of Elastic Beam

We established our model through steps set out in Sections 2.3.3 & 3.1.3. The response of the structure in vacuum is first determined. (ω1 is the first order natural frequency of the beam.) The analysis considers in vacuum and in fluid acceleration amplitude at the top of the cylindrical beam.

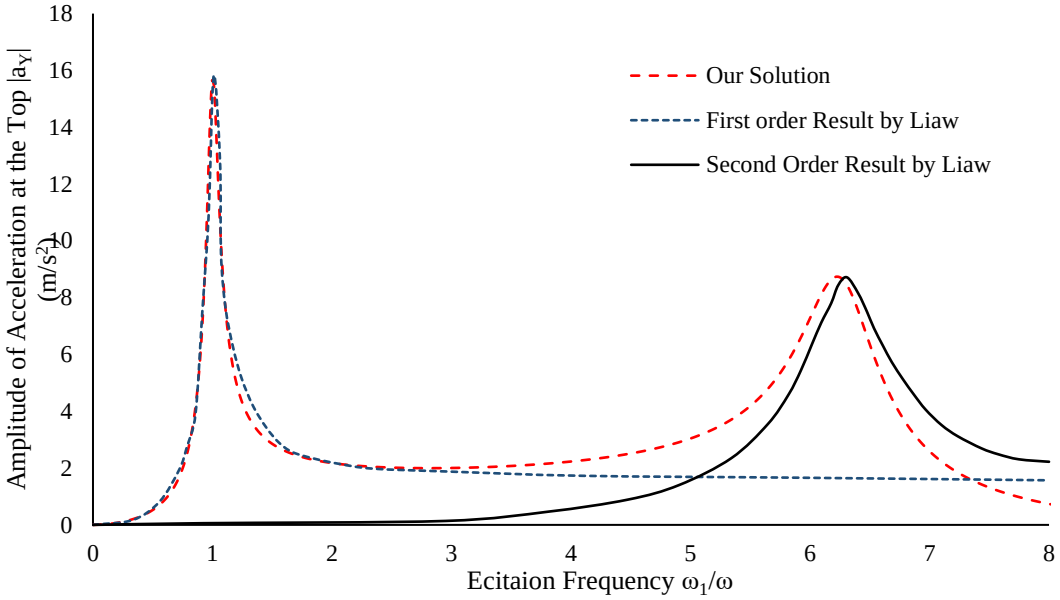


Figure 4.10 The amplitude of $a_Y$ when in vacuum.

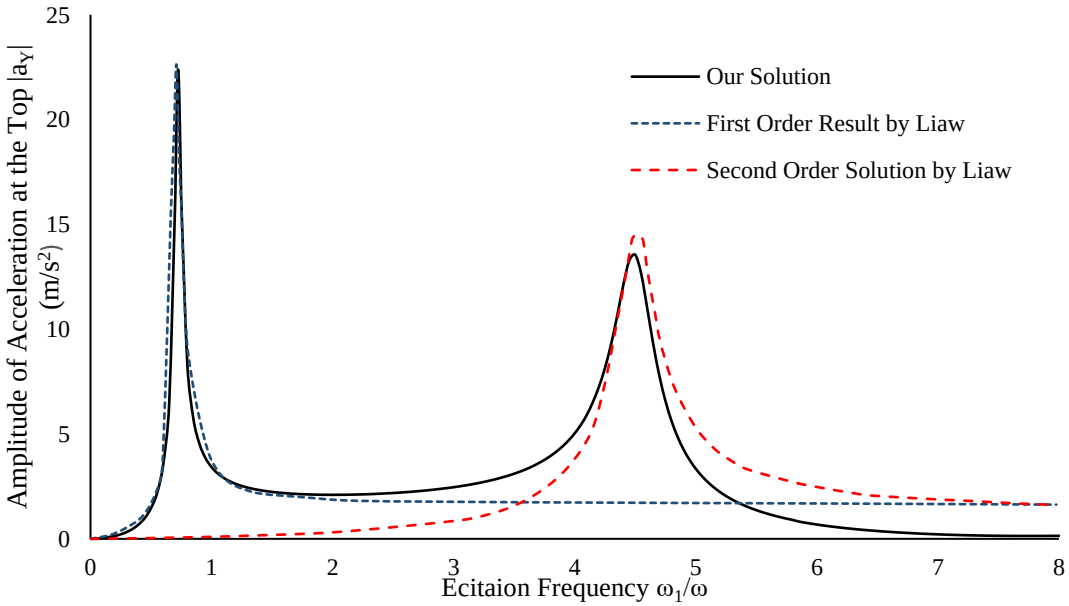


Figure 4.11 The amplitude of $a_Y$ when surrounded by water.

As we can see from the plots, the resonance frequencies are shifted to lower values due to the existence of fluid. This is because the hydrodynamic force has the effect of added mass on the vibrating structure. Our results match well at the first order frequency in terms of amplitude of and shifting, the difference around second order frequency is due to the phase shift between the two modes. If we take the values of phase shift given by Liaw [73] in to consideration, we will obtain the total result in Figure 4.12.

It is clear that the two curves match well with only a small differences around the 2nd order resonant frequency. This suggests our logic for solving fluid-structure interaction problems with boundary conditions unknown a' priori is correct for simple elastic structures and gives strong credence to our intended future analysis of Anaconda. Indeed, this model is insufficient for the Anaconda study as the material does not have the flexibility of rubber. Significant elastic vibration appears only when the excitation frequency is relatively high, which prevent us from analysing the behaviour of flexible structures under the effect of free surface. However, on the other hand, shows our methods is not limited for solving low frequency problems.

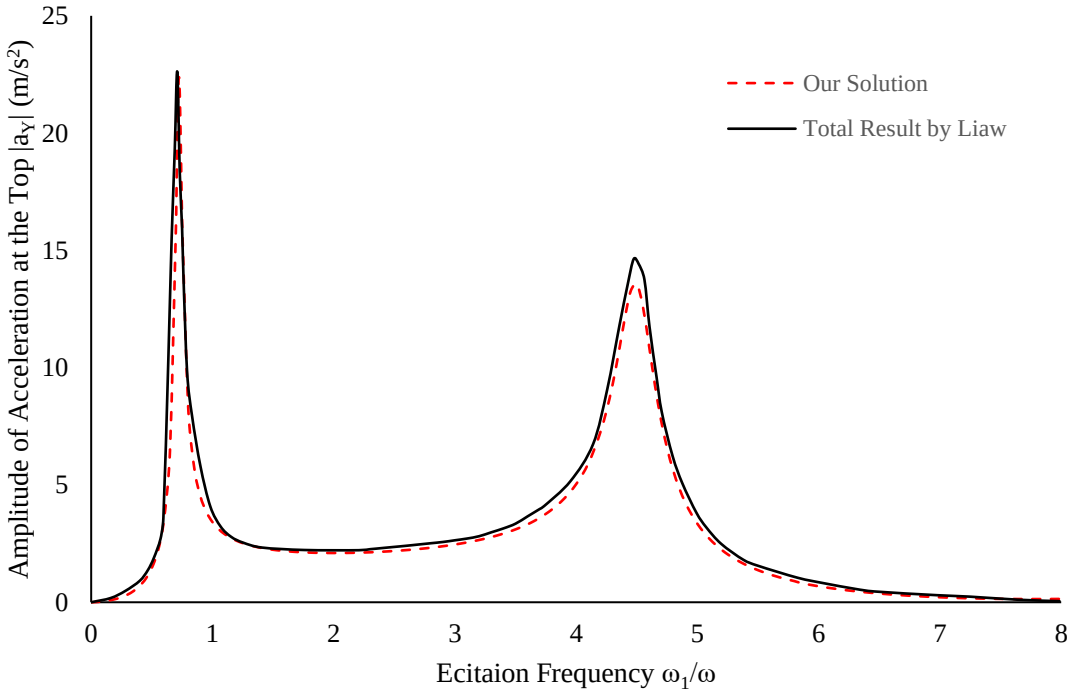


Figure 4.12 The comparison of total result of structural response.

# 5 Result for Closed boundary Problems

Having established some verification of the proposed method through comparison of results with public domain results, applications of the method that are more novel are presented.

## 5.1 Verification

An obvious verification of this method corresponds to making the body shell rigid.

### 5.1.1 Stiff Shell Verification

When the boundary is under rigid motion, the solution of the internal fluid will be uniform flow and hence, the whole structure will reduce to a solid body. There will be little discrepancies between the solutions of the solid model and the direct coupling model proposed when the shell stiffness is high under the otherwise same conditions.

The spheres simulated here have diameter D = 10 m and the distance of their centroid from the undisturbed free surface is d = 6 m. Wavenumber $\nu = 0.2\ m^{-1}$ & $N\varphi = 48$ for both cases. The stiffness of the shell is measured by $\varepsilon = 4Et_s/[d(1-\mu)]\cdot(1/\rho g A_w)$, where E is the Young's Modulus of the material, $t_s$ is the shell thickness, $\mu$ is the Poison ratio, $A_W$ is the excitation wave amplitude. The term $4Et_s/[d(1-\mu)]$ describes the stiffness of the shell relative to its scale. $\rho g A_w$ is the maximum hydrodynamic pressure generated by a propagating incident wave of infinite water depth. For an indication of magnitude, $\log(\varepsilon) = 5.38$ when E = 205 GPa, $t_s = 0.01$ m, $\mu = 0.3$, $\rho = 1000\ kg/m^3$, $g = 9.81\ m/s^2$ and $A_W = 0.5$ m.

An indication of the discrepancy between the two models is the maximum radial deformation of the shell boundary compared to the original shell radius. $|\delta max|$ denotes division of the maximum absolute difference between the two solutions of normal displacement by sphere radius.

Degeneration tendency is proved by plotting $|\delta_{max}|$ against $\log(\varepsilon)$ in Figure 5.1. The model clearly converges to a solid model when $\log(\varepsilon) > 2.20$. Elastic behaviour requires the material to be less stiff. Verification of the dynamic correctness of the system is achievable by means other than stiff model analysis

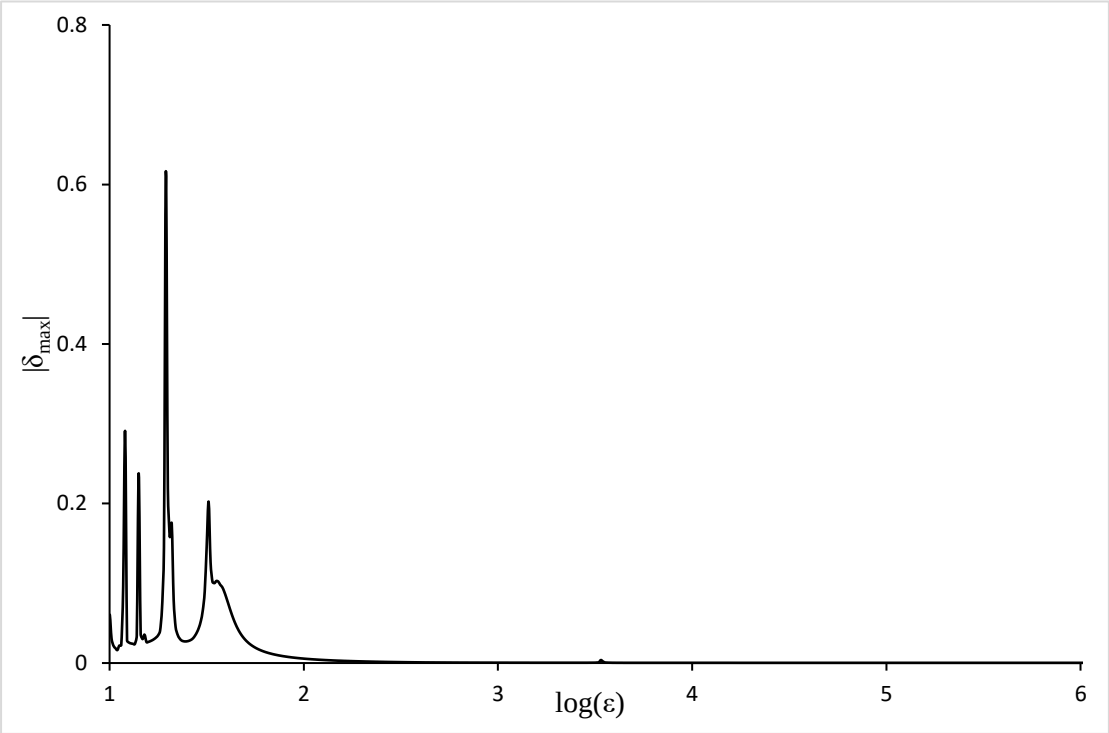


Figure 5.1 Variation of the maximum radial deformation of the spherical shell when the material is reduced to being rigid. Little discrepancy is observed when ε is high.

### 5.1.2 Extremely Flexible Shell Verification

Besides stiff model analysis that verifies the dynamic correctness of the system, we can apply another extreme analysis to show the hydrodynamic force solved is correct.

A more demanding analysis is necessary to demonstrate the hydrodynamic force is correctly solved. The body should exhibit a negligible scattering of the incident wave as the matrix $\widetilde{\mathbf{D}}$ of Equation 2.4.9 tends to 0. Furthermore, the internal hydrodynamic pressure will be continuous with the external excitation wave pressure. It can be directly proved mathematically that the solution of $\overrightarrow{p_I}$ equal to $\overrightarrow{p_0}$ in Equation 2.4.9 if we address that $\overrightarrow{p_A}$ satisfies relationship 2.4.8 with -$\overrightarrow{v_D}$ and $\overrightarrow{p_0} = \overrightarrow{p_A} + \overrightarrow{p_E}$.

For a model of log(ε) = -1, the discrepancy between internal and external hydrodynamic pressures is of ($o^{-3}$), continuity of pressure is also verified when E = 0 GPa.

## 5.2 Analysis

Four types of deformation exist for a loaded shell model: bending, stretching, transverse

shearing and torsion.

The last case is seldom investigated. Furthermore, it will not considered here since only normal the hydrodynamic forces are normal to the boundary. Transverse shearing is merged into bending, since the boundary is thin. Bending and stretching are significant, but the latter is less dominant since the volume of the container should not change due to the incompressibility of the internal fluid.

Existing analysis [81-83] for a torsion less empty spherical shell suggests two branches of vibration modes, representing bending & dominant dynamic stretching. Stretching frequencies are significantly larger than that those of bending. Such modes are not to be excited and, therefore, not presented in our hydrodynamic problems.

### 5.2.1 Natural Vibrations

When the shell thickness is assumed 0, the nondimensionalised vibration frequency $\omega R(\rho/E)^{1/2}$ converge to unity on the bending branch solution for high order modes [81]. This result (not the low order frequencies) is theoretically independent of Poison ratio. We take the same non-dimensional variable in our analysis.

The solution of high order frequencies will gradually diverge when shell thickness is considered. Validation requires analysis of the empty dry shell for $t_s$ = 0.01 m. A fully filled model in vacuum and in infinite water depth are designated Case I & II. Natural vibration frequencies are derived applying the method of Section 3.1.2. They are in Figure 5.2.

The dry model solutions are densely concentrated near $\omega R(\rho/E)^{1/2} = 1$ as predicted. The first order frequency is $\omega_1 R(\rho/E)^{1/2} = 0.722$ & 0.737 according to Reference [82] and our simulation respectively. The existence of shell thickness will result in higher natural frequencies for the dry model. Variation around a single solution exists since the element model is not perfectly spherical.

The first order natural frequencies for Case I & II are $\omega_1 R(\rho/E)^{1/2} = 0.0422$ & 0.0253. Recognising that natural frequency is inversely proportional to the square root of oscillating mass, and the total mass of the shell calculated is 1/1500 of the solid 10 m diameter sphere, the solution is of correct order ($\sqrt{1500} \approx 38.7$). The internal fluid takes

effect like added mass to the shell structure and it would degenerate to ‘mass’ when the shell is rigid.

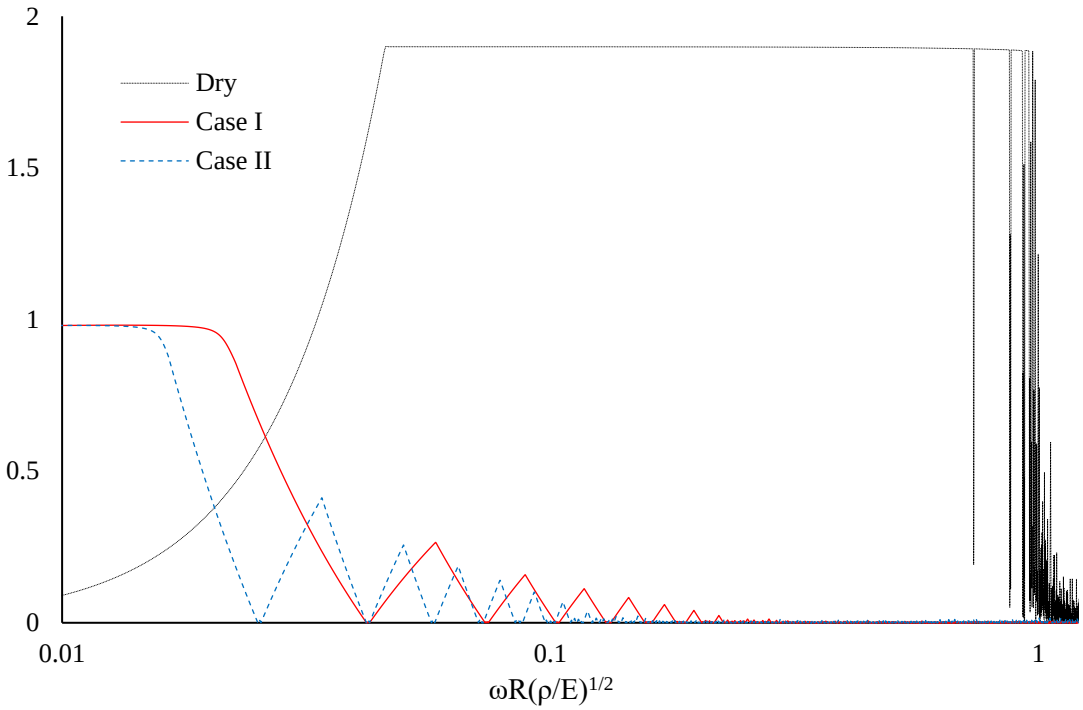


Figure 5.2 Minimum singular value of matrix **L** for different cases. Minimums of the curve indicate singular matrix at the corresponding frequencies, which is the natural vibration frequency solved. Horizontal axis is logarithmic and ends at $\omega R(\rho/E)^{1/2} = 1.2$.

Solutions in Case II are even lower than in Case I since external fluid inertia is added to the vibration. For the first order solution, the mass added is 2.78 times compare to the whole internal volume. It is significant larger than 0.5, which is the added ratio of an accelerating solid sphere, since the whole boundary is acting with fluid the in radial direction.

The intervals between the low order frequencies is larger when an incompressible fluid exists in the shell. Higher order frequencies distinctly distributed compared to the dry model solutions.

When E is low, the higher order modes are excited at lower frequencies and the solution may be singular under ocean wave conditions. However, the result in Section 3.3 suggests that the solution is smooth and physical. The procedure is stable under

extreme soft cases.

According to Nirodson [83], the bending-dominating modes of an zero-thickness dry spherical shell is $P_n^m(\cos\theta)\cos m\varphi$, where $P_n^m(x)$ is the associated Legendre polynomial. The modes are exactly spherical harmonics and the total internal volume is unchanged with such a boundary motion. One must have n ≥ 2 here since n = 0 refers to the 'breathing' mode, which has no physical solution on the bending branch, and n = 1 refers to rigid body oscillation. Considering m can be zero and m ≤ n, there exist n + 1 modes for the $n^{th}$ order vibration, degenerated under the same frequency. Modes of the same order can represent each other through a combination of simple rotation and linear summation, therefore, they are not different modes.

Due to the harmonic nature of an incompressible and irrotational fluid, the vibration mode of Case I has little difference with the empty one, despite numerical error and imperfection of mesh symmetry. There exist n + 1 zero eigenvalues and their corresponding mode shapes for matrix **L** when analysing $n^{th}$ order vibration.

Figure 5.3 illustrates the visualised axisymmetric modes shapes (m = 0) of order n = 2 ~ 5. The results are similar those of a dry sphere for both m = 0 and m ≠ 0 cases (see Figures 3 & 4 of reference [83]).

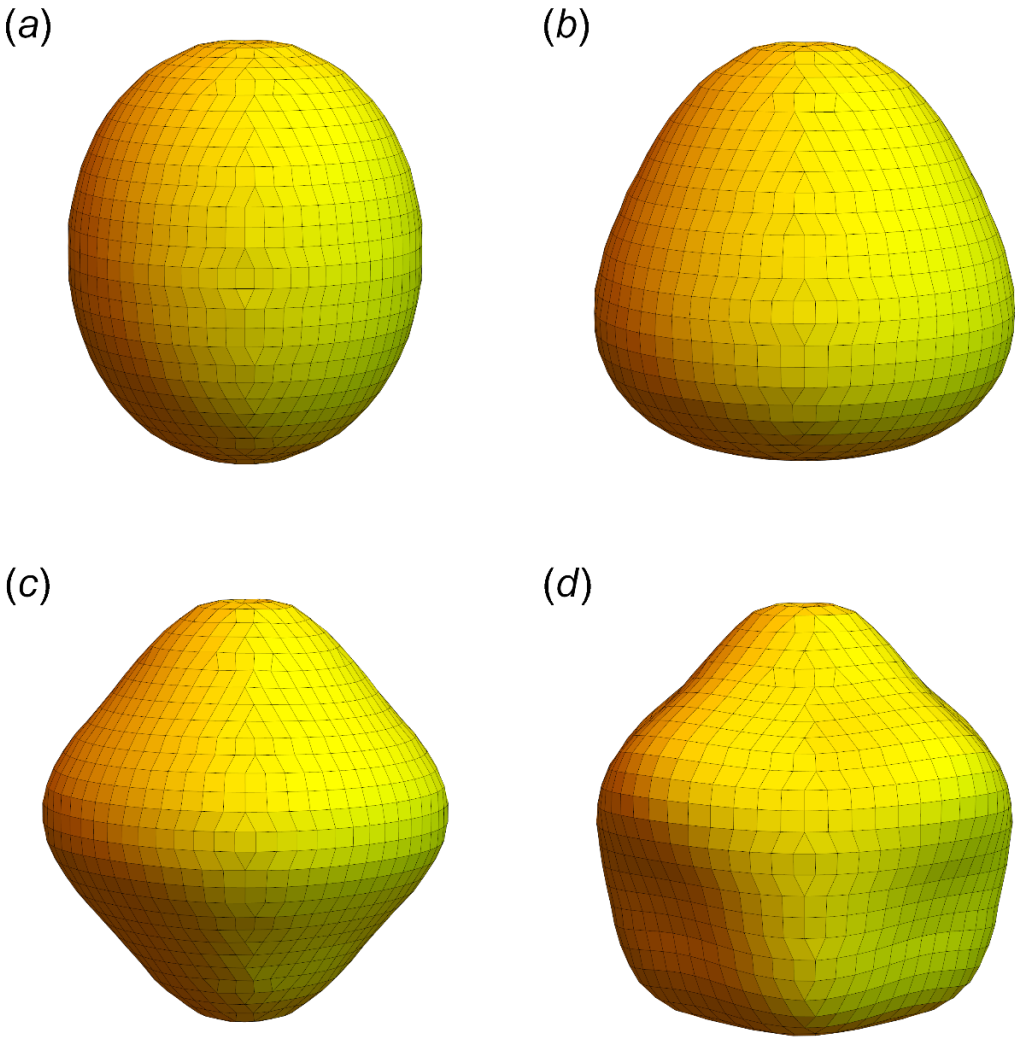


Figure 5.3 The axisymmetric natural vibration modes of an elastic shell filled fully with incompressible fluid.

### 5.2.2 Wave Body interaction

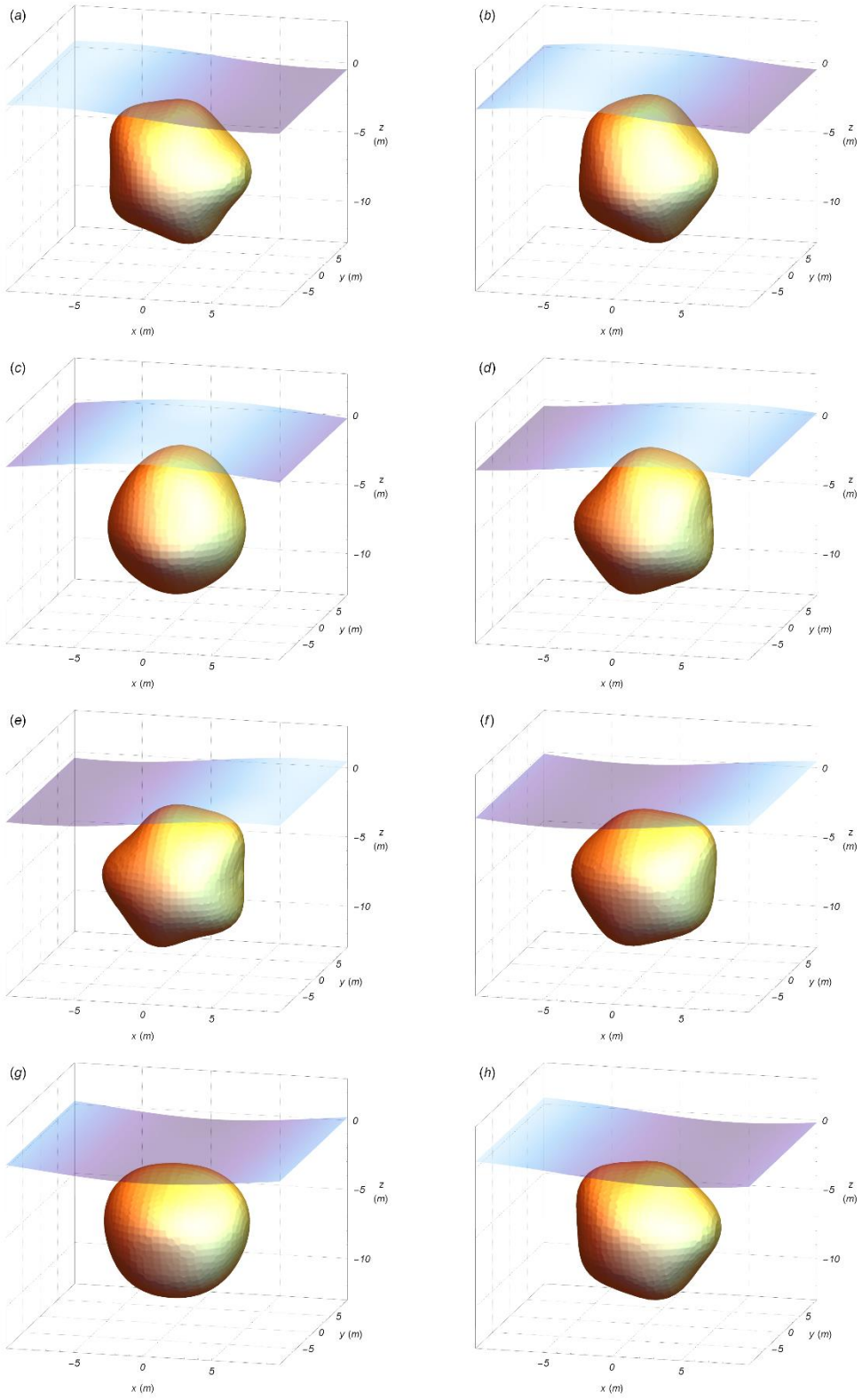


Figure 5.4 The structural response when order n = 5 mode is excited. Wave frequency here is ν = 0.209. Subfigures (a) ~ (h) are captured with π/4 phase shift intervals.

Having studied both rigid and extremely soft body behaviour studied previously, the elastic response of the spherical shell of intermediate stiffness is investigated. Since we are essentially investigating different orders of modes under excitation, it is equivalent to either changing the external excitation frequencies or the shell stiffness. The geometry studied here is consistent with those introduced in the previous section. Young's modulus of the spherical shell is now fixed at $E = 10^{-2}$ GPa ($\log(\varepsilon) = 1.07$) whilst the external wave frequency is changing for different modal responses.

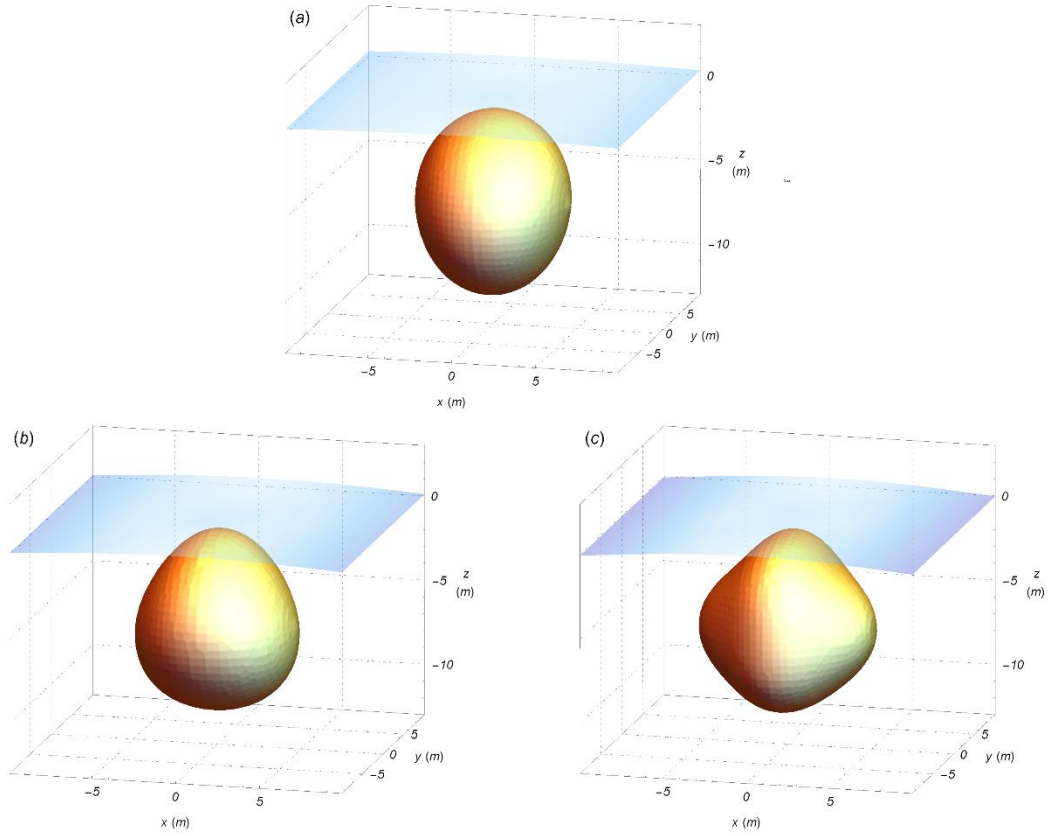


Figure 5.5 Modes of order n = 2, 3, 4 excited by incident waves are presented in (a) ~ (c). The excitation frequencies are $\nu = 0.097, 0.140$ & $0.170$. Phase is when wave crest passes over the sphere.

Solutions close to resonance are nonphysical as the infinitesimally small response assumption is breached. Such solutions are only of mathematical interests as boundary material will be damaged under large loads. The results presented here are the ones present indicate clear modal responses but of regular amplitudes. Matrix **L** will not be

ill-conditioned due to the existence of the external free surface (complex elements in matrix $\mathbf{T}_E$). The resonant frequencies are different with those of Case I & II.

Figure 5.4 illustrates order n = 5 modal response of a sphere. Modal effect is significant on the deeper part of the body, whereas the body boundary close to the free surface experiences the higher wave induced hydrodynamic loads. The top of the structure moves along with the crest and the trough of the progressing wave, as shown in subfigures (c) & (g). This result is reasonable as hydrodynamic pressure decreases exponentially with water depth so that the upper part of the sphere is under forced oscillation whilst the lower part is relatively free. Figure 5.5 illustrates other modes for the case of wave crest coincident with the top of the sphere.

Between the two modal responses, there exist a transition region where no mode is dominant while the behaviour is still elastic. The response is similar with that of an extremely soft model and externally excited wave shell motion. Such intervals can be observed in Figure 5.1 as well for log(ε) between 1 ~ 1.5. Figure 5.6 provides visualisations of the responses.

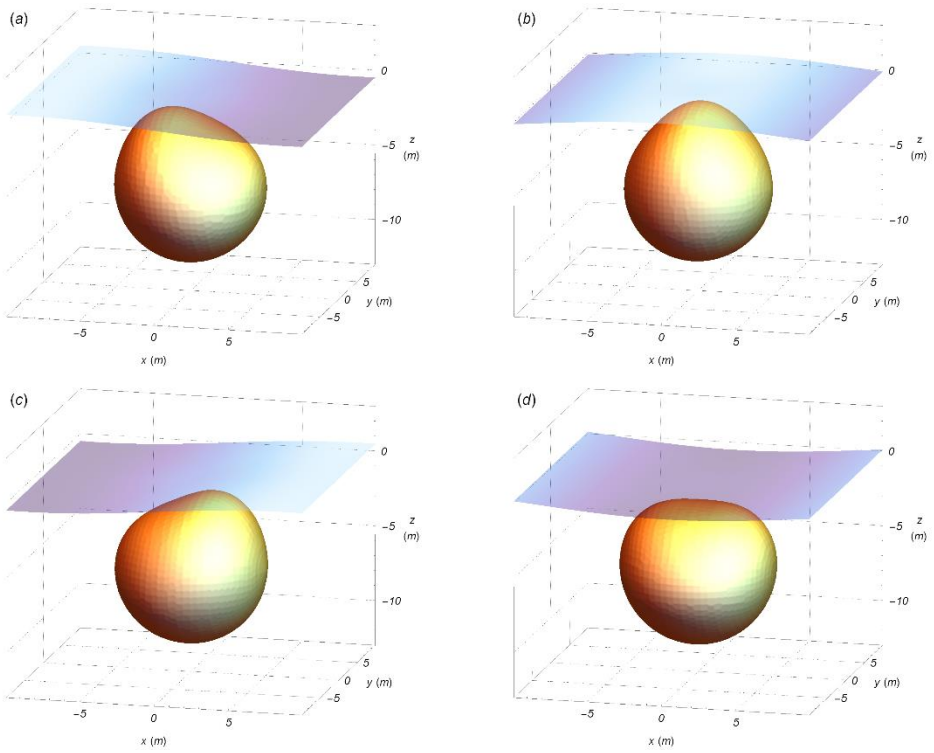


Figure 5.6 Transition state when wave frequency ν = 0.185. Subfigures (a) ~ (d) are captured with π/2 phase shift intervals.

# 6 The Study of Anaconda

The Anaconda analysis undertaken looks at natural frequencies, the effect of impedance, variation of tube length and depth, and tube slenderness.

## 6.1 Closed model

As per Chapman et al. [52] the Anaconda model has a length $L_0 = 30\pi$ m (caps not included) and a radius $R_s = 3.5$ m. The incident wave amplitude $A_W = 0.5$ m with a wavenumber $\nu = 0.2$ corresponding to a wavelength $\lambda = 10\pi$ m and a wave velocity $c_w$ =7.0 m/s. The effective length of the rubber tube is 3 times that of the wavelength and the top of the tube is located 1.0 m below the undisturbed free surface.

### 6.1.1 Resonant Frequency

Tube resonance changes with tube wall elasticity. A key parameter of resonance is the ratio of external wave velocity $c_w$ and bulge wave velocity $c_b$ determined according to Equation 1.2.1.Additionally, comparison is made of the maximum pressure within the tube with the maximum external wave hydrodynamic pressure $\rho g A_W$.

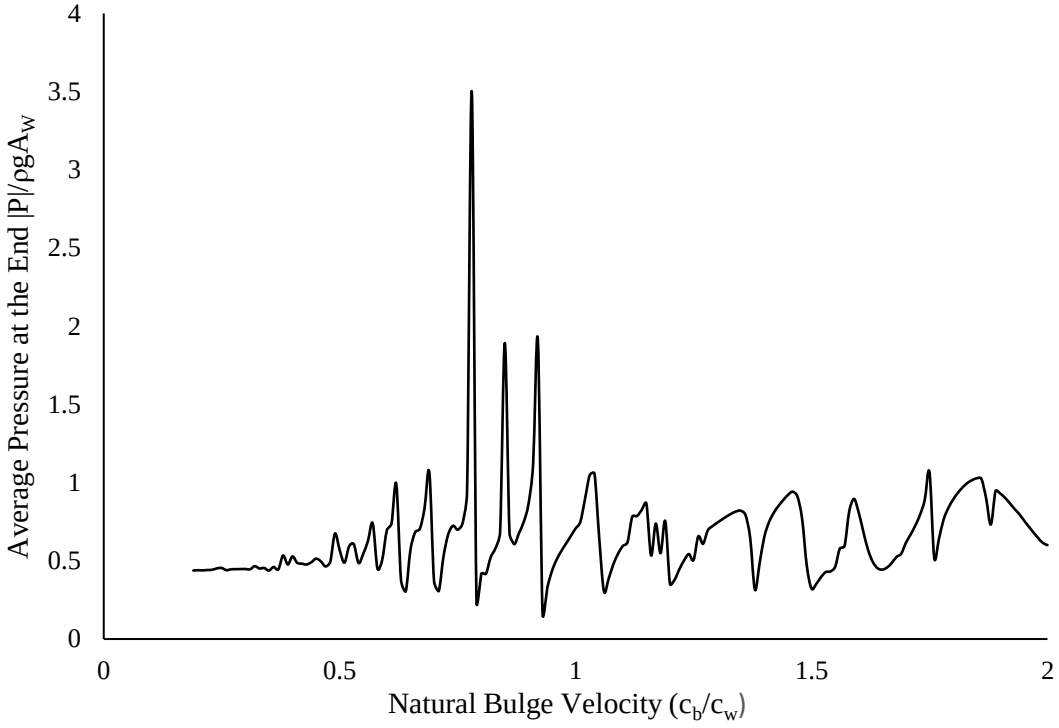


Figure 6.1 The average pressure measured at the end cross section

Figure 6.1 shows that the resonance of the internal hydrodynamic pressure appears at 0.78 $c_w$ rather than exactly 1 $c_w$. This is a reasonable result, considering the 3-dimensional nature of the model and the end effects of the tube. Chapman et al. [52] in their experimental study noted that a maximum pressure appears when $c_w$ was slightly larger than $c_b$.

Another important observation is the sensitivity of the internal pressure to variation in tube distensibility, as it may drop dramatically near the resonance frequency. This situation may arise due to the induced wave hydrodynamic pressure decreasing exponentially water depth. According to Equation 2.1.15, the hydrodynamic pressure at the tube top is 4.06 times larger than that induced at the tube bottom. Therefore, uniform stretching of the tube does not occur implying the 1-dimensional predictions of the device is misleading.

### 6.1.2 Visualised Phenomenon

The model under resonant state is visualised as follow

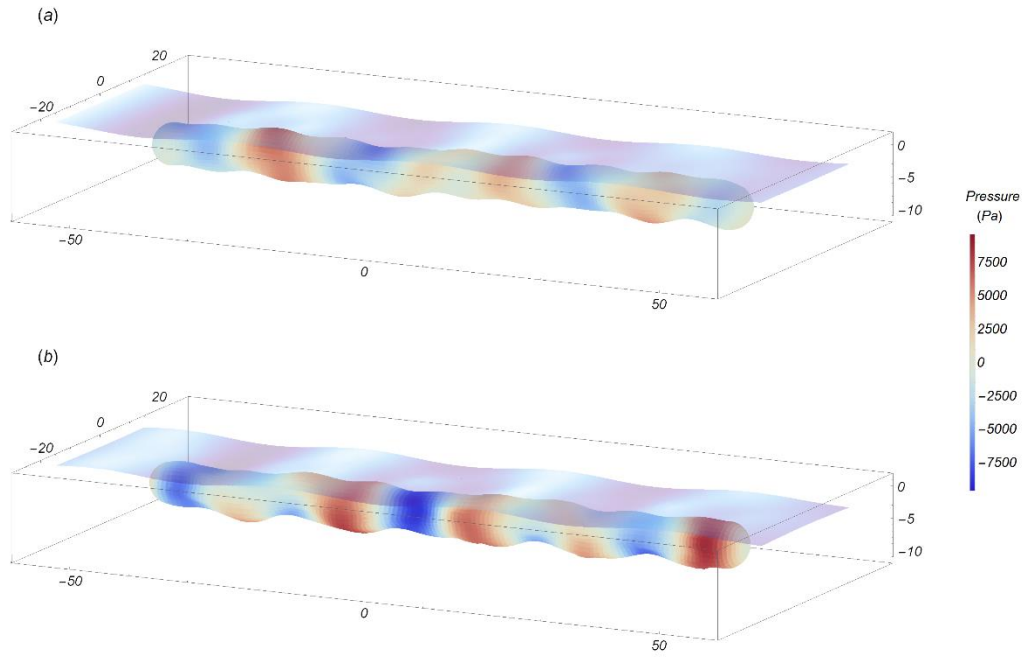


Figure 6.2 Internal pressure on closed Anaconda tube under resonant condition. Subfigure (a) is the system at phase $\varphi = 2\pi/3$. Subfigure (b) is at $\varphi = 7\pi/6$ when the bulge strikes the tube end, the phase is $\pi/2$ ahead of that in subfigure (a). Internal pressure acting on the tube wall is visualised with cold and warm colour.

Clear bulge behaviour is observable in Figure 6.2 without any significant bending along the tube. The distribution of pressure is clearly not uniform over a cross section; as assumed in 1-dimensional wave theory. However, the pressure over the tube end does show uniform behaviour.

## 6.2 Power Take off

### 6.2.1 Effect of Impedance

Following the derived resonant condition the next task is to predict the capture width of the device for the same structural property and wave conditions but different levels of impedance. The only difference in tube modelling is the removal of the flexible end cap.

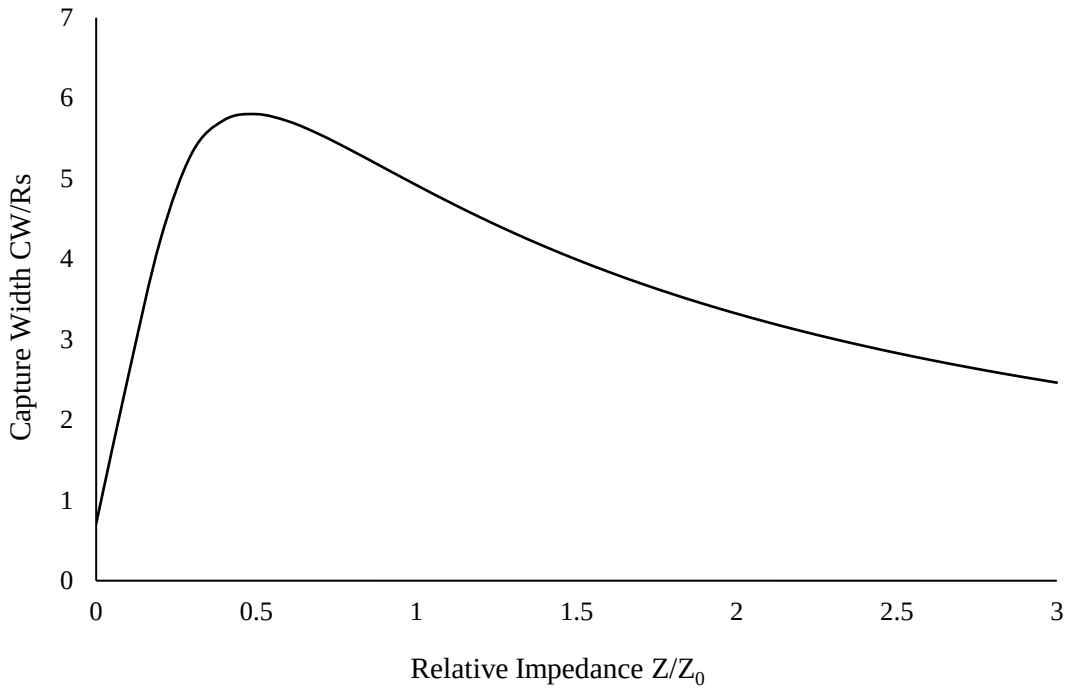


Figure 6.3 The capture width relative to the diameter of the tube with the change of impedance at the end cross section.

The natural impedance of the tube under this condition is $Z_0$ = 258.3 kg·s$^{-2}$·m$^{-4}$. Figure 6.3 suggest the maximum power occurs at around $Z/Z_0$ equals 0.5, with a corresponding capture width 5.8 times tube diameter. When no artificial impedance is

imposed the energy flux is close to the power of the incident wave passing through the circular cross section.

When impedance tends to infinity, the power take-off slowly approaches zero as the end flow tends to zero. Such an effect is not significant as the induced end tube resistant force is only 2.1 times the excitation force as Figure 6.4 shows.

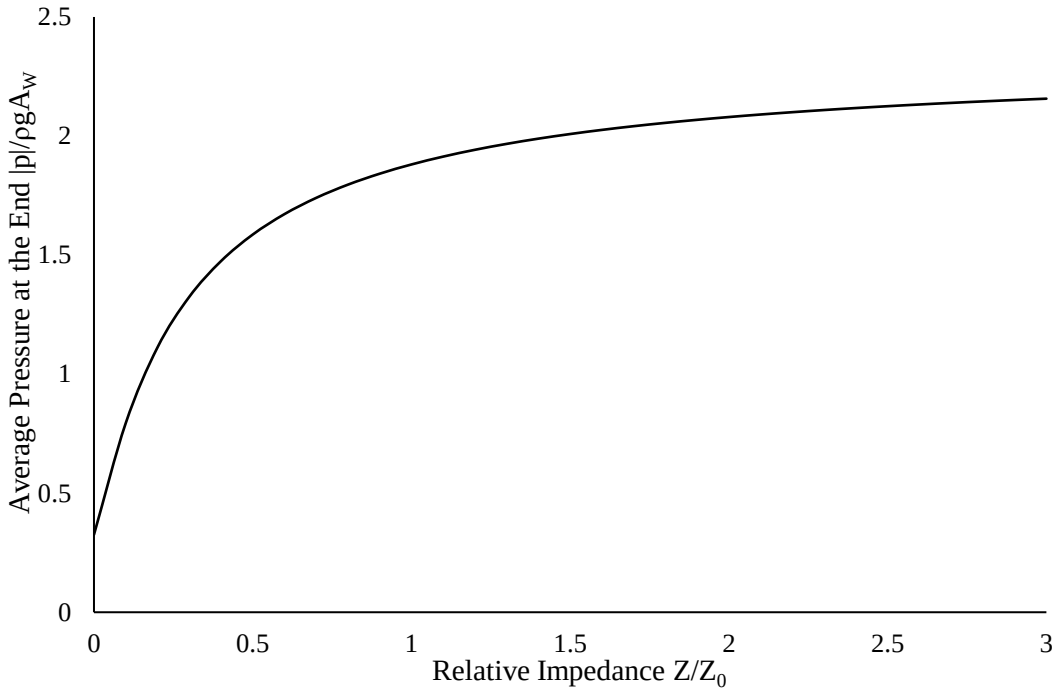


Figure 6.4 Predicted tube-end average pressure measured at the end cross section for impedance model

The growth of the pressure at the tube end is physically correct, since it will converge to a fixed value as the end plate becomes 'rigid'. The average pressure at the initial point is lower than the hydrodynamic pressure induced at the free surface because of the decreasing nature of wave pressure with depth

### 6.2.2 Response along the Length

According to Farley & Rainey [51] and Mei [56] predictions, the amplitude and pressure of bulge waves should increase in the propagating direction when at resonance. When off resonance, such growth will be repressed and fluctuate along the length. The next investigation tries to verify this prediction. The only available numerical predictions of Anaconda with both capture width and radial extension are those of Mei

[56].

The geometry is unchanged with model impedance of 0.5 for maximum power take-off. Comparison is made of the new predictions with the 1-dimensional calculations of Mei [56]. Since the model studied here is 3-dimensional, use of average radial deflection removes the influence of shifting tube centre.

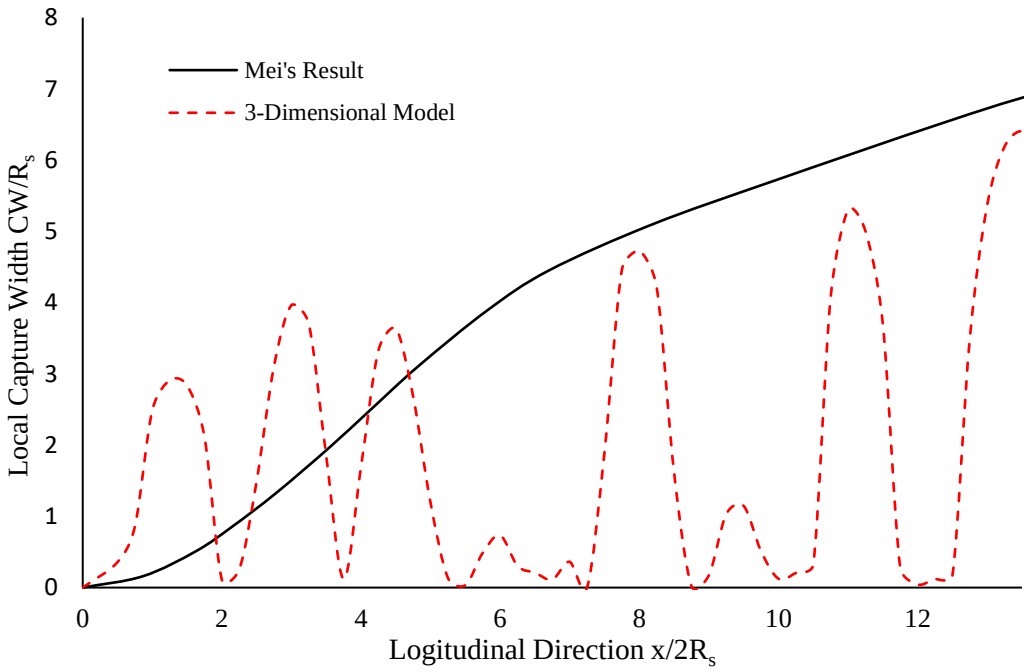


Figure 6.5 Local capture width along the length of the tube for 3-dimensional direct coupling model and 1-dimensional analysis by Mei [56].

Figure 6.5 indicates a significant difference between results generated by the 3-dimisional direct coupling method and the 1-dimensional analysis of Mei [56]. The local capture width does not increase monotonically as predicted, but fluctuates dramatically with the wave propagation. The capture width drops close to zero at several locations, but generally increases along the tube as the local maximum is becoming larger. The magnitude of capture width is of the same order with the Mei prediction, which suggests the result generated here is regular.

The relative radial extension in the propagating wave direction in Figure 6.6 exhibits similar characteristic with the local capture width curve. However, the magnitude is

significantly smaller than the 1-dimensional predictions and is not strictly in accordance with the variation of capture width.

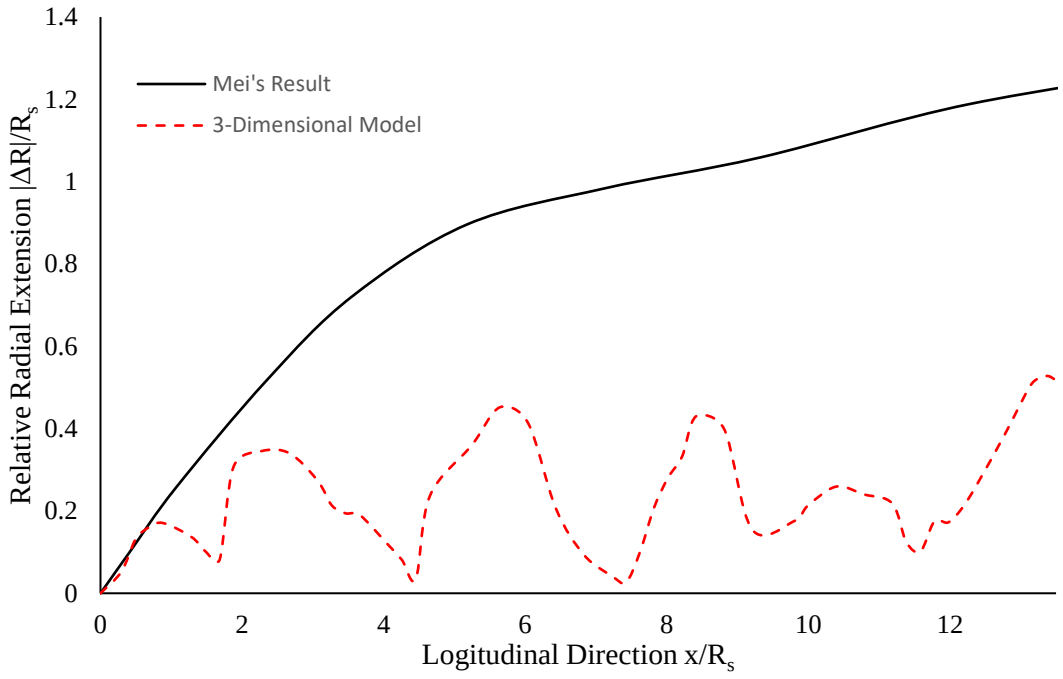


Figure 6.6 Comparison of new 3-dimensional direct coupling model and 1-dimensional analysis of average longitudinal radial expansion of tube.

According to Mei [56], the radial expansion of the tube is zero within the hydrodynamic field and is only effective when analysing bulge wave propagation. Meanwhile, the excitation pressure equals the wave dynamic pressure at the free surface. That is, it is as if the tube is floating without any thickness or radial dimension. This raises significant model defects since both non-uniform distribution of the hydrodynamic pressure and the 3-dimensioinal effect of the shell is crucial to the behaviour of the system. Fluctuated distribution may be a consequence of different responses in different phases across the top and bottom of the tube. This also gives rise to the sensitivity of the tube stiffness of Figure 6.1.

### 6.2.3 Effect of Tube Length and Depth

Tube models of different length and depth location are investigated. The longer tube has $L_0 = 40\pi$ m with all other parameters unchanged..

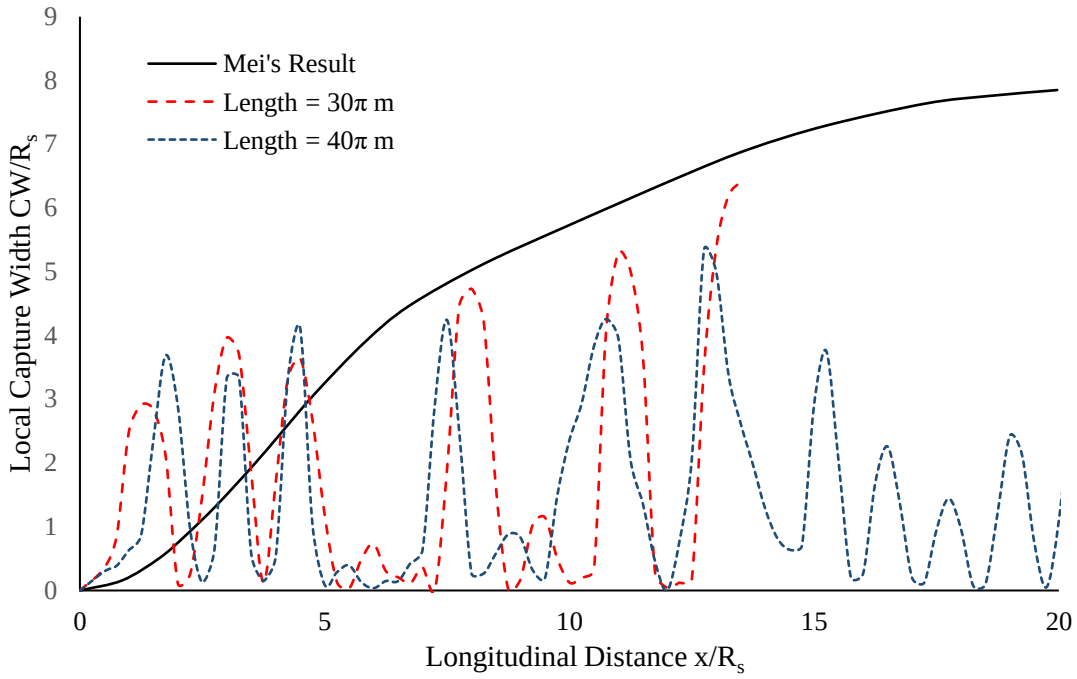


Figure 6.7 Local capture width along the length of the tube for 3-dimensional direct coupling model of tube length $L_0 = 30\pi$ m and $40\pi$ m.

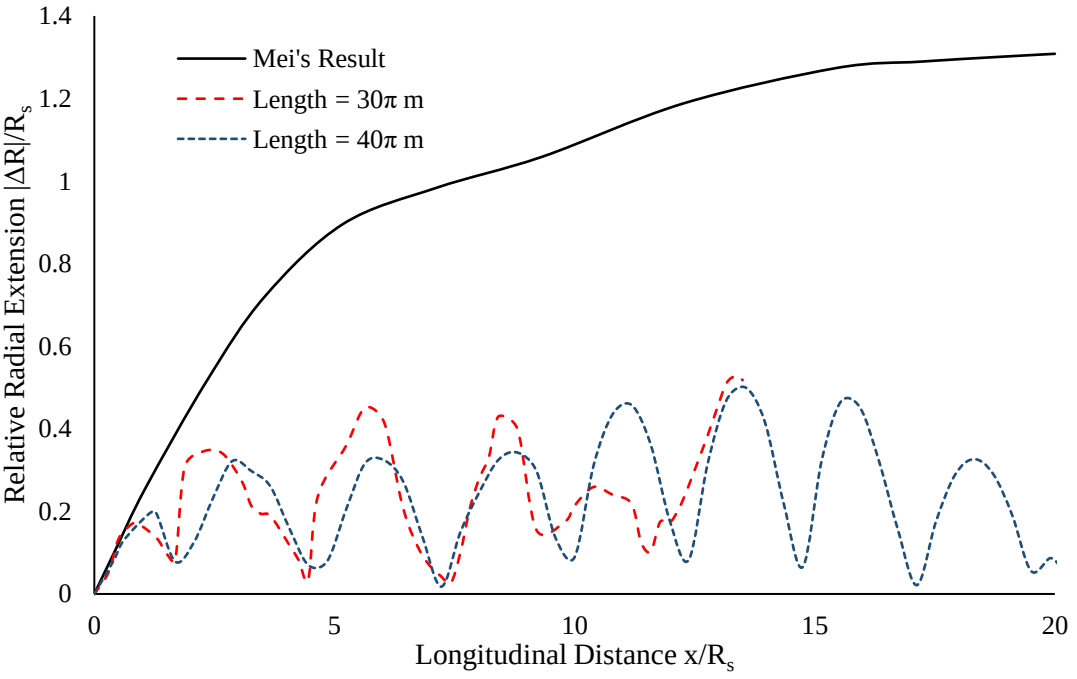


Figure 6.8 Local average radial expansion along the length of the tube for 3-dimensional direct coupling model of tube length $L_0 = 30\pi$ m and $40\pi$ m.

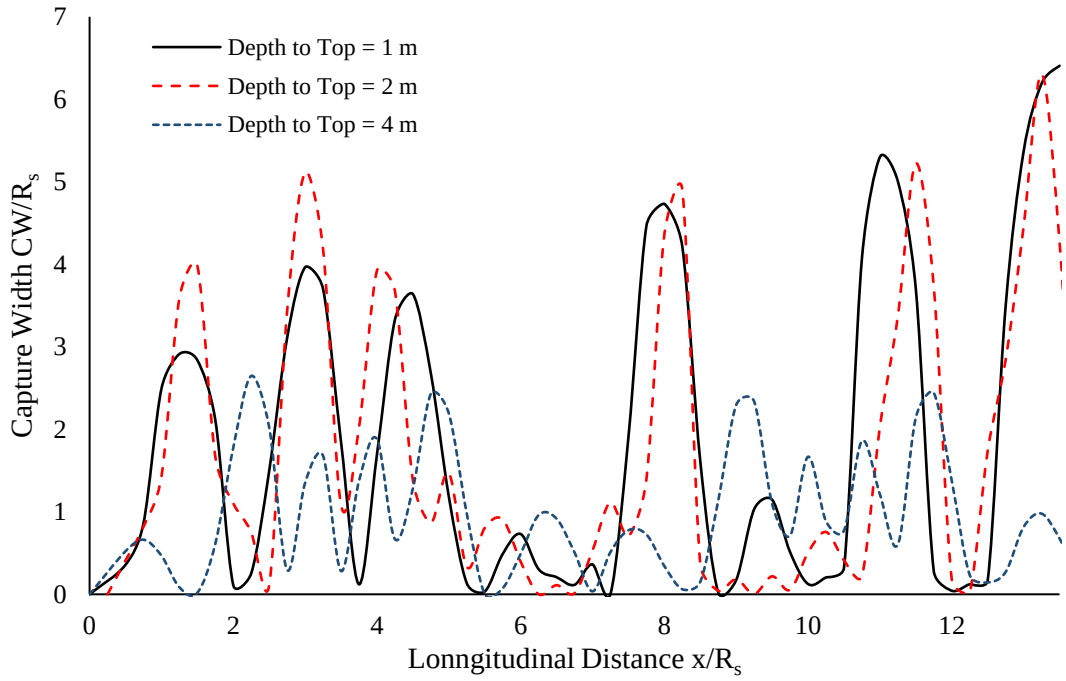


Figure 6.9 Local capture width along the length of the tube for 3-dimensional direct coupling model when the tube is located at 1 m, 2m and 4 m from its top to the free surface.

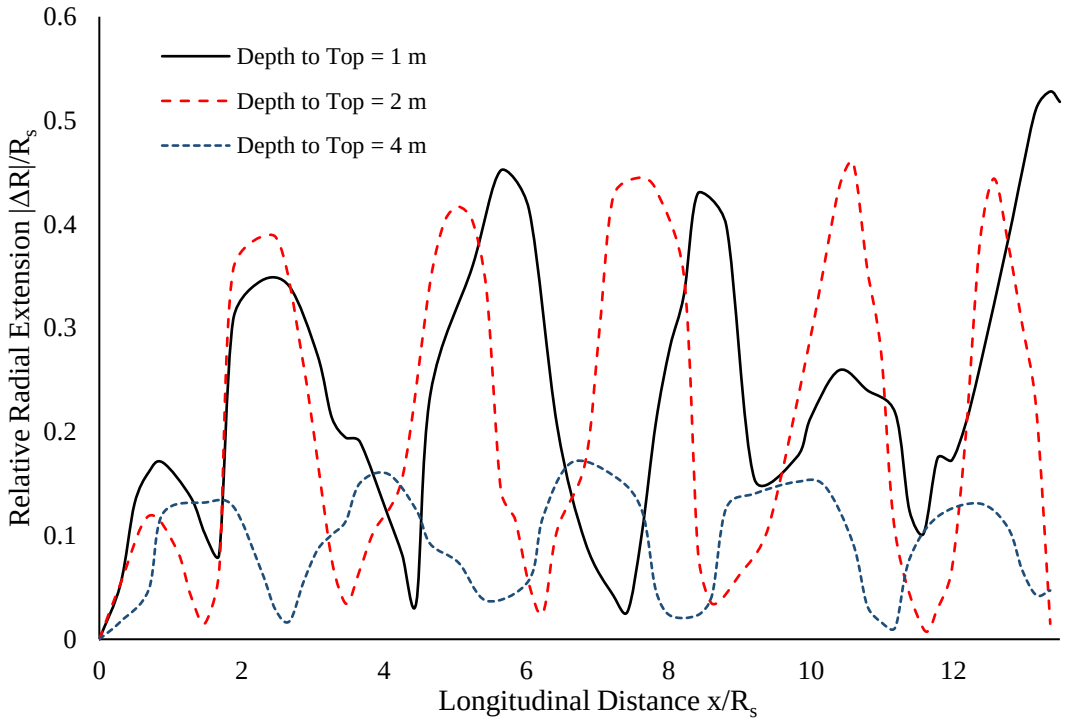


Figure 6.10 Local average radial expansion along the length of the tube for 3-dimensional direct coupling model when the tube is located at 1 m, 2m and 4 m from its top to the free surface.

Figure 6.7 provides local capture width results for both tube lengths with the predictions of Mei. The 3-dimensional predictions of maxima and minima occur at similar locations with similar magnitude for both tube lengths. However, the relative shifting of the curves implies there are significant differences at each longitudinal tube location. That is, the device is numerically sensitive to its length. Furthermore, for the longer tube the maximum value of capture width no longer increases further along the tube, indicating there is a length limit for a resonating 3-dimensional tube. Figure 6.8 provides comparison of radial expansion variation. This figure too reinforces the conclusion of limited length benefit.

For the depth sensitivity analysis, the top of the tube is located at depths of 2 m and 4 m from the free surface. The original depth was 1m. The tube length is the original length of 30π m with the rest of the geometry and parameters unchanged. Comparisons are provided of capture width and radial extension for all three location depths.

Figures 6.9 & 6.10 show that the device is as very sensitive to located depth. For the shallower cases the distribution of responses are similar, but with non-negligible phase shifts. The magnitude of the 1m and 2m depth models are close. The slightly deeper tube model (h' = 2 m) even exhibits a larger response at the incident wave end of the tube. The 4m deep model behaves entirely different. Response magnitudes are essentially halved for the very deep tube. According to Equation 2.1.15 the hydrodynamic wave pressure for the 1 m, 2 m and 4 m depth tubes are 0.81, 0.67, 0.45 times of the free surface pressure.

The results of Figures 6.7 to 6.10 reveal significant challenges for designing an Anaconda WEC. The response is too sensitive to external wave excitation and geometry to obtain steady power take-off, even though the numerical inputs are regular. In addition, tubes do not have to be very long to obtain an 'efficient' working condition, as responses can reach a large enough magnitude in a relatively short distance.

### 6.2.4 Effect of slenderness

Here we attempt to remove the sensitivity of the Anaconda device by making the tube slenderer. This is so the pressure distribution over the circular cross-section will be relatively uniform and less longitudinal stress within the structure may take effect.

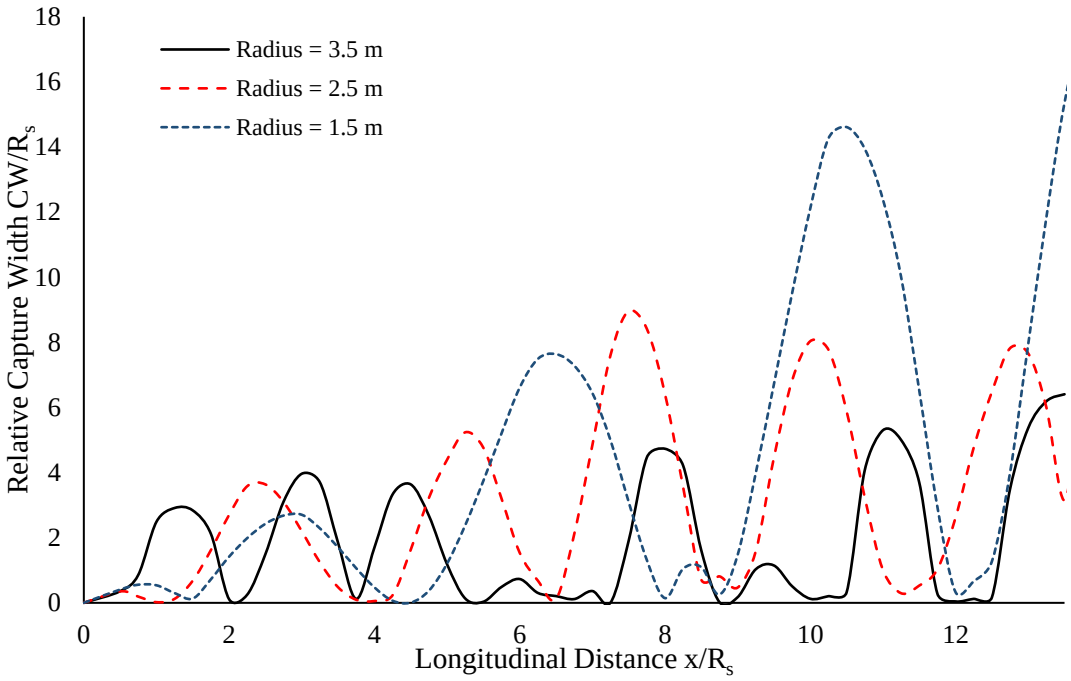


Figure 6.11 Local longitudinal relative capture width of tube from 3-dimensional direct coupling model. Radius $R_s$ = 3.5 m, 2.5 m and 1.5 m.

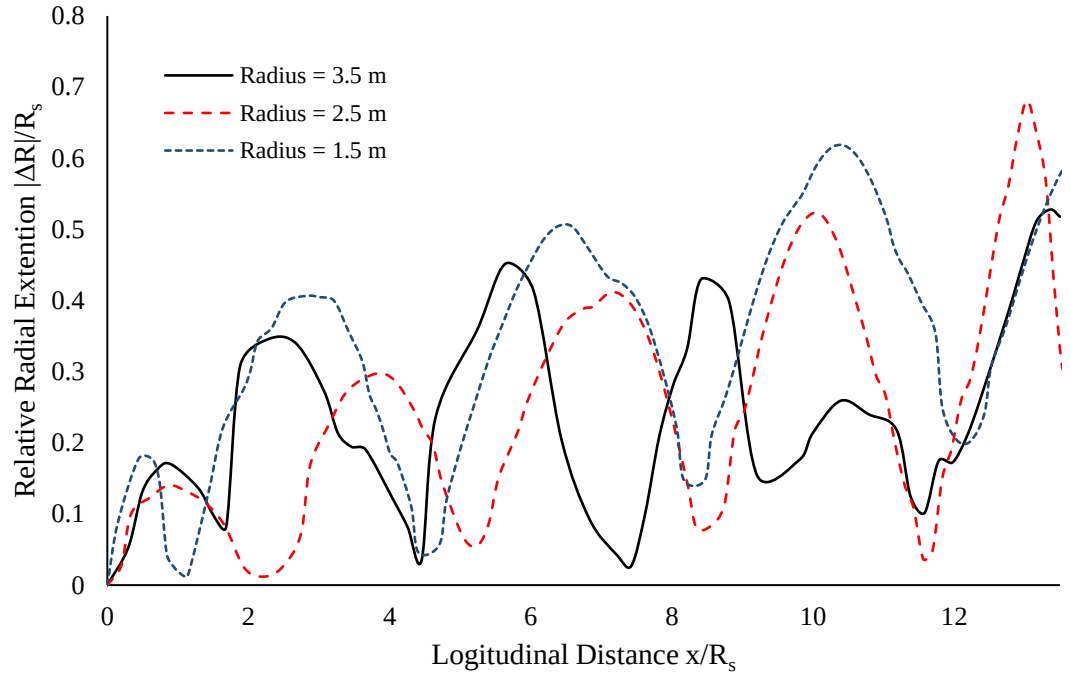


Figure 6.12 Local longitudinal relative radial extension of tube for 3-dimensional direct coupling model. Radius $R_s$ = 3.5 m, 2.5 m and 1.5 m.

Tube radii of 2.5 m and 1.5 m (originally 3.5 m) are modelled with their tube centre

depths of their centres unchanged at 4.5 m. Young's modulus altered whilst tube distensibility remains unaltered as tube diameter is amended appropriately (see Equation 1.2.3)

Figures 6.11 & 6.12 provide the slenderer tube responses. The radial divider in the non-dimensional capture width parameter corresponds to the model radius. The fluctuated behaviour of power take-off and radial expansion remains. However, the fluctuated 'period' is becoming more regular for the slenderer tubes and the growth along the propagation direction is more significant. Thus, the device is also sensitive to tube slenderness.

The larger relative capture width on the slenderer model implies that to almost the same amount of energy take-off occurs given the device radius is relatively smaller. This means the work done by the hydrodynamic forces at the bottom of the device are small and it is advantageous to construct a slenderer device for optimal efficiency.

# 7 Conclusion & Further Works

Careful reviews were provided of earlier Multipole and Boundary Element analyses for wave-body interaction subject to excitation by an external fluid together with deduction of the associated mathematical details

The necessity .for developing the concept of direct coupling method within the context of marine hydrodynamics arose from the complexities of the Anaconda wave energy device. The necessity also arises for any fully closed boundary problem. Various alternative forms of the direct coupling method were discussed to illustrate the high flexibility of the method.

The idea of using of a Rankine source within the internal fluid problem highlighted a non-uniqueness problem within the closed boundary of an incompressible fluid was discussed. The non-uniqueness of the Neumann boundary condition problem was overcome by a reversal of the normal process and changing the unknown boundary variable.

A boundary element analysis for internal flow with free surface was proposed. Correct natural frequencies were predicted by identifying the singularities of the associated matrix formulation. The numerical predictions agreed well with analytical predictions for a cylindrical geometry.

Verification of the proposed direct coupling was achieved for regular open domains. The solutions matched well with the published results and were physically meaningful. Implemented cases of fully closed boundary problems were successfully solved. The natural vibration frequencies and mode shapes of a closed spherical shell containing an incompressible fluid is first determined in this study. Wave-body interaction studies also generated reasonable results. As well, the method proposed for analysing such models is valid.

The proposed direct method successfully analysed the Anaconda wave energy convertor by considering the tube material to be of linear elastic. Resonant frequencies of the device agreed with the trends of published theoretical values. The bulge wave

phenomenon is observable from the graphical visualisations of the predicted solution. The predicted pressure is reasonable compared to the hydrodynamic pressure of excitation wave.

Power take off is roughly calculated through an imaginary impedance plane. The growing and decreasing tendency of the Anaconda capture width and pressure are generally physical. The predicted responses fluctuate along the propagating direction. This results in high sensitivity of the device to structural stiffness and geometrical changes. This phenomenon is not removed by making the tube slenderer. Establishing sensible length, diameter and depth location of the device is vital for the design and feasible operation of Anaconda under real sea conditions.

Only direct head waves to the device have been analysed. Given the structure in practice would be constrained by appropriate mooring and tensioning devices at each end weathervaning of the device would be limited. Hence, wave headings up to ± 150 would be required in a fuller analysis of the eventual design. The mooring system is likely to make the device behave as an inverted complex pendulum. Hence, the design of the mooring system would require taking into account low frequency damping influences. In published offshore analyses of offshore structures low frequency accounting led to significant reduction in the costs of the associated mooring system.

Survivability of the .Anaconda device, rather power take performance, would require beam seas to be analysed since this could lead to excessive stretching of the tube. Avoidance of aneurysm has suggested the use of a partial longitudinal stiffening. A phenomenon associated with pressurisation of the tube. .

Further work should focus on advanced finite element analysis. This is necessary since the structural behaviour is much different from the linear assumption when the tube is pressurised. For example, an inflated tube is free from buckling compared to a hollow one. Furthermore, a proper method is required to determine the initial state of tube equilibrium.

It would be sensible to consider hyperplastic material based finite elements. However, frequency domain analysis would be inappropriate due to system nonlinearity.

A new necessity would be to solve the problem of non-uniqueness for incompressible

in the time domain.

The structures studied are not translating. Analogous direct coupling procedures for a slowly advancing structure with internal fluids is required. This might also resurrect interest in large-scale water and fuel transport in flexible Dracone barges.

# References

[1] MacCamy, R. and Fuchs, R. (1954). Wave forces on piles. pp.1-14.

[2] Dean, W. (1948). On the reflexion of surface waves by a submerged circular cylinder. Mathematical Proceedings of the Cambridge Philosophical Society, 44(04), p.483.

[3] Ursell, F. and Dean, W. (1950). Surface waves on deep water in the presence of a submerged circular cylinder. I. Mathematical Proceedings of the Cambridge Philosophical Society, 46(01), p.141.

[4] Ogilvie, T. F., & Shin, Y. S. (1978). Integral-Equation Solutions for Time-Dependent Free-Surface Problems. Journal of the Society of Naval Architects of Japan, 1978(143), 41-51.

[5] Ursell, F. (1949). On the heaving motion of a circular cylinder on the surface of a fluid. The Quarterly Journal of Mechanics and Applied Mathematics, 2(2), 218-231.

[6] Ursell, F. (1949). On the rolling motion of cylinders in the surface of a fluid. The Quarterly Journal of Mechanics and Applied Mathematics, 2(3), 335-353.

[7] Tasai, F. (1959). On the damping force and added mass of ships heaving and pitching. Journal of Zosen Kiokai, 1959(105), 47-56.

[8] Havelock, T. (1955). Waves due to a Floating Sphere Making Periodic Heaving Oscillations. Proceedings of the Royal Society A: Mathematical, Physical and Engineering Sciences, 231(1184), pp.1-7.

[9] Hulme, A. (1982). The wave forces acting on a floating hemisphere undergoing forced periodic oscillations. Journal of Fluid Mechanics, 121(-1), p.443.

[10] Wang, S. (1986). Motions of a spherical submarine in waves. Ocean Engineering, 13(3), pp.249-271.

[11] Frank, W. (1967). Oscillation of cylinders in or below the free surface of deep fluids. DAVID W TAYLOR NAVAL SHIP RESEARCH AND DEVELOPMENT CENTER BETHESDA MD DEPT OF HYDROMECHANICS.

[12] Chen, Z. M. (2015). Regular wave integral approach to numerical simulation of radiation and diffraction of surface waves. Wave Motion, 52, 171-182.

[13] Newman, J. (1999). Marine Hydrodynamics. Cambridge: The MIT Press, p.300.

[14] Mei, C. C., Stiassnie, M. A., & Yue, D. K. P. (2005). Theory and Applications of Ocean Surface Waves: Part 1: Linear Aspects.

[15] Hou, G., Wang, J., & Layton, A. (2012). Numerical methods for fluid-structure interaction—a review. Communications in Computational Physics, 12(2), 337-377.

[16] Iii, J. N., Newman, P. A., Iii, A. T., & Hou, G. W. (1999). Efficient nonlinear static aeroelastic wing analysis. Computers & fluids, 28(4-5), 615-628.

[17] Moran, H. J. –P., Ohayon, R., (1999). Fluid-Structure Interaction: Applied Numerical Methods, Wiley

[18] Dowell, E. H., & Hall, K. C. (2001). Modeling of fluid-structure interaction. Annual review of fluid mechanics, 33(1), 445-490.

[19] Chakrabarti, S. K. (Ed.) (2005), Numerical Models in Fluid Structure Interaction, Advances in Fluid Mechanics, Vol. 42, WIT Press.

[20] Heller, S. and Abramson, H. (1959). Hydroelasticity: a new naval science. Journal of the American Society for Naval Engineers, 71(2), pp.205-209.

[21] Heller Jr, S. R., & ABRAMSON, H. N. (1959). Hydroelasticity: a new naval science. Journal of the American Society for Naval Engineers, 71(2), 205-209.

[22] Hirdaris, S. and Temarel, P. (2009). Hydroelasticity of ships: recent advances and future trends. Proceedings of the Institution of Mechanical Engineers, Part M: Journal of Engineering for the Maritime Environment, 223(3), pp.305-330.

[23] Bishop, R. E. D. and Price, W. G. (1979). Hydroelasticity of Ships, Cambridge University Press, Cambridge.

[24] Bishop, R. E. D., Price, W. G., & Temarel, P. (1979). A unified dynamical analysis of antisymmetric ship response to waves (No. Paper No. W15).

[25] Bishop, R. E., Chalmers, D. W., & Price, W. G. (1986). The dynamic characteristics of unsymmetrical ship structures. Royal Institution of Naval Architects Transactions, 128.

[26] Belik, Ö., & Price, W. G. (1982). Comparison of slamming theories in the time simulation of ship responses in irregular waves. International Shipbuilding Progress, 29(335), 173-187.

[27] Belik, O., Bishop, R. E., & Price, W. G. (1988). Influence of bottom and flare slamming on structural responses. Royal Institution of Naval Architects Transactions, 130.

[28] Bishop, R. E., Clarke, J. D., & Price, W. G. (1984). Comparison of full scale and predicted responses of two frigates in a severe weather trial. Royal Institution of Naval Architects Transactions, 126.

[29] Aksu, S., Price, W. G., & Temarel, P. (1991). A comparison of two-dimensional and three-dimensional hydroelasticity theories including the effect of slamming. Proceedings of the Institution of Mechanical Engineers, Part C: Mechanical Engineering Science, 205(1), 3-15.

[30] Bishop, R. E. D., Price, W. G., & Wu, Y. (1986). A general linear hydroelasticity theory of floating structures moving in a seaway. Philosophical Transactions of the Royal Society of London. Series A, Mathematical and Physical Sciences, 316(1538), 375-426.

[31] Lundgren, J., Price, W. G., & Wu, Y. (1989). A hydroelastic investigation into the behaviour of a floating'dry'dock in waves. Royal Institution of Naval Architects Transactions, 131.

[32] Fu, Y., Price, W. G., & Temarel, P. (1987). The' dry and wet' towage of a jack-up in regular and irregular waves. Royal Institution of Naval Architects Transactions, 129.

[33] Du, S. X., Wu, Y. S., and Price, W. G. (1998). Forward speed effect on the structural responses of a ship travelling in waves. In Proceedings of the 2nd International Conference on Hydroelasticity in marine technology, Fukuoka, Japan, pp.401–410.

[34] Ergin, A., & Temarel, P. (2002). Free vibration of a partially liquid-filled and submerged, horizontal cylindrical shell. Journal of Sound and vibration, 254(5), 951-965.

[35] Kashiwagi, M. (2000). Research on hydroelastic responses of VLFS: recent progress and future work. International Journal of Offshore and Polar Engineering, 10(02).

[36] Wu, Y., Wang, D., Riggs, H. R., & Ertekin, R. C. (1993). Composite singularity distribution method with application to hydroelasticity. Marine Structures, 6(2-3), 143-

163.

[37] Bai, K. J., Yoo, B. S., & Kim, J. W. (2001). A localized finite-element analysis of a floating runway in a harbor. Marine structures, 14(1-2), 89-102.

[38] Jensen, J. J. (1978). Wave-Induced Bending Moments in Ships--A Quadratic Theory (No. Report No. 136).

[39] Wu, Y. S., Maeda, H., Kinoshita, T., 1997. The second order hydrodynamic actions on a flexible body. Journal of Institute of Industrial Science, University of Tokyo 49 (4), 8–19.

[40] Chen, X. J., Jensen, J. J., Cui, W. C., & Fu, S. X. (2003). Hydroelasticity of a floating plate in multidirectional waves. Ocean Engineering, 30(15), 1997-2017.

[41] Chen, X. J., Wu, Y. S., Cui, W. C., & Jensen, J. J. (2006). Review of hydroelasticity theories for global response of marine structures. Ocean Engineering, 33(3-4), 439-457.

[42] Harding, R. D., Hirdaris, S. E., Miao, S. H., Pittilo, M., & Temarel, P. (2006, September). Use of hydroelasticity analysis in design. In Proceedings of the 4th International Conference on Hydroelasticity in marine technology, China (pp. 1-12).

[43] Zienkiewicz, O. C., Kelly, D. W., & Bettess, P. (1977). The coupling of the finite element method and boundary solution procedures. International journal for numerical methods in engineering, 11(2), pp.355-375.

[44] Wilton, D. T. (1978). Acoustic radiation and scattering from elastic structures. International journal for numerical methods in engineering, 13(1), pp.123-138.

[45] Mathews, I. C. (1986). Numerical techniques for three-dimensional steady-state fluid–structure interaction. The Journal of the Acoustical Society of America, 79(5), pp.1317-1325

[46] Kim, K. T., Lee, P. S., & Park, K. C. (2013). A direct coupling method for 3D hydroelastic analysis of floating structures. International Journal for Numerical Methods in Engineering, 96(13), pp.842-866.

[47] Lee, K. H., Cho, S., Kim, K. T., Kim, J. G., & Lee, P. S. (2015). Hydroelastic analysis of floating structures with liquid tanks and comparison with experimental tests. Applied Ocean Research, 52, 167-187.

[48] Energy.soton.ac.uk. (2016). Anaconda Wave Energy Converter Concept |

Sustainable Energy Research Group. [online] Available at: http://www.energy.soton.ac.uk/anaconda-wave-energy-converter-concept/

[49] Lighthill, M. (1978). Waves in fluids. Cambridge [England]: Cambridge University Press.

[50] Chaplin J., Farley F., Prentice M., Rainey R., et al. (2007). Development of the Anaconda all-rubber WEC. In: 7th European Wave and Tidal Conference. Lisbon, pp.1-13.

[51] Farley, F., and Rainey, R. (2006). Anaconda the bulge wave sea energy converter. Maritime Energy Development Ltd., pp.1-12.

[52] Chaplin, J., Heller, V., Farley, F., Hearn, G. and Rainey, R. (2011). Laboratory testing the Anaconda. Philosophical Transactions of the Royal Society A: Mathematical, Physical and Engineering Sciences, 370(1959), pp.403-424.

[53] Heller, V., Chaplin, J. and Farley, F. (2010). Physical model tests of the Anaconda wave energy converter. In: Proc. 1st IAHR European Congress., pp.1-6.

[54] Chaplin, J., Farley, F. and Rainey, R. (2007). Power conversion in the Anaconda WEC. In: Proc 22nd Intl. Workshop on Water Waves and Floating Bodies., pp.29-32.

[55] Farley, F. J. M., Rainey, R. C. T., & Chaplin, J. R. (2012). Rubber tubes in the sea. Philosophical Transactions of the Royal Society A: Mathematical, Physical and Engineering Sciences, 370(1959), 381-402.

[56] Mei, C. (2014). Nonlinear resonance in Anaconda. J. Fluid Mech., 750, pp.507-517.

[57] Bucchi, A. and Hearn, G. (2013). Delay or removal of aneurysm formation in the Anaconda wave energy extraction device. Renewable Energy, 55, pp.104-119.

[58] Bucchi, A., & Hearn, G. E. (2013). Predictions of aneurysm formation in distensible tubes: part A—theoretical background to alternative approaches. International Journal of Mechanical Sciences, 71, 1-20.

[59] Bucchi, A., & Hearn, G. E. (2013). Predictions of aneurysm formation in distensible tubes: part B—application and comparison of alternative approaches. International Journal of Mechanical Sciences, 70, 155-170.

[60] Sommerfeld, A. (1949). Partial differential equations in physics (Vol. 1). Academic

press, pp.44-51.

[61] Wehausen, J. and Laitone, E. (1960). Surface waves. Berlin: Springer.

[62] Hearn, G. E. (1977). Alternative methods of evaluating Green's function in three-dimensional ship-wave problems. Journal of Ship Research, 21(2), pp.89-93.

[63] Newman, J. N. (1985). Algorithms for the free-surface Green function. Journal of engineering mathematics, 19(1), 57-67.

[64] Newman, J. N. (1992). The approximation of free-surface Green functions. Wave asymptotics, 107-135.

[65] Noblesse, F. (1982). The Green function in the theory of radiation and diffraction of regular water waves by a body. Journal of Engineering Mathematics, 16(2), 137-169.

[66] Newman, J. N. (1992). The Green function for potential flow in a rectangular channel. Journal of engineering mathematics, 26(1), 51-59.

[67] Sommerfeld, A. (1949). Partial differential equations in physics. New York: Academic Press, pp.188-200.

[68] Thorne, R. and Ursell, F. (1953). Multipole expansions in the theory of surface waves. Mathematical Proceedings of the Cambridge Philosophical Society, 49(04), p.707.

[69] Meirovitch, L. (2010). Fundamentals of vibrations. Long Grove, Illinois: Waveland Press.

[70] Bathe, K. (1996). Finite element procedure. Englewood Cliffs, N.J.: Prentice Hall.

[71] Lee, P. S., & Bathe, K. J. (2004). Development of MITC isotropic triangular shell finite elements. Computers & Structures, 82(11-12), 945-962.

[72] Ko, Y., Lee, P. S., & Bathe, K. J. (2017). A new MITC4+ shell element. Computers & Structures, 182, 404-418.

[73] Liaw, C. and Chopra, A. (1974). Dynamics of towers surrounded by water. Earthquake Engineering & Structural Dynamics, 3(1), pp.33-49.

[74] Newman, J. (1984). Approximations for the Bessel and Struve functions. Mathematics of Computation, 43(168), pp.551-556.

[75] Hess, J. and Smith, A. (1967). Calculation of potential flow about arbitrary bodies. Progress in Aerospace Sciences, 8, pp.1-138.

[76] Garrison, C., & CHOW, P. (1972). Wave forces on submerged bodies. Journal of Waterways, Harbors & Coast Eng Div, 98(WW3), pp.1-5.

[77] Sanderson, C. and Curtin, R. (2016). Armadillo: a template-based C++ library for linear algebra. The Journal of Open Source Software, 1(2), p.26.

[78] Evans, D. and Linton, C. (1993). Sloshing Frequencies. The Quarterly Journal of Mechanics and Applied Mathematics, 46(1), pp.71-87.

[79] John, F. (1950). On the motion of floating bodies II. Simple harmonic motions. Communications on Pure and Applied Mathematics, 3(1), pp.45-101.

[80] Ursell, F. (1981). Irregular frequencies and the motion of floating bodies. Journal of Fluid Mechanics, 105(-1), p.143.

[81] Baker, W. E. (1961). Axisymmetric Modes of Vibration of Thin Spherical Shells, Journal of Acoustic Society of America, vol. 33, pp. 1749–1758.

[82] Wilkinson, J. P. (1965). Natural Frequencies of Closed Spherical Shells, The Journal of the Acoustical Society of America, vol. 38, issue 2, p. 367.

[83] Niordson, F. I. (1984). Free vibrations of thin elastic spherical shells. International journal of solids and structures, 20(7), 667-687.

# Appendix A

The Laplace equation in cylindrical coordinate form is,

$$\frac{\partial^2\phi}{\partial R^2}+\frac{1}{R}\frac{\partial\phi}{\partial R}+\frac{1}{R^2}\frac{\partial^2\phi}{\partial\varphi^2}+\frac{\partial^2\phi}{\partial z^2}=0\,. \tag{A.1}$$

where φ is the azimuth angle and R is the projected distance in the x-y plane. In a variable separation solution ϕ is partitioned as

$$\phi(R,z,\varphi)=\Lambda(R)Z(z)F(\varphi)\,. \tag{A.2}$$

Substitution into Equation A.1 yields

$$\left[\frac{\Lambda''}{\Lambda}+\frac{1}{R}\frac{\Lambda'}{\Lambda}\right]+\left[\frac{1}{R^2}\frac{F''}{F}\right]+\left[\frac{Z''}{Z}\right]=0\,. \tag{A.3}$$

Satisfaction of this equation requires each bracketed term to be a constant. Let the z term be equal to a real constant $p^2$ then,

$$\frac{Z''}{Z}=p^2 \tag{A.4}$$

has the general solution,

$$Z=C_1e^{pz}+C_2e^{-pz}\,. \tag{A.5}$$

Our appreciation of the derivation of incident wave velocity potential suggest

$$p=\nu \tag{A.5}$$

It follows that for infinite and finite water depth respectively Z satisfies.

$$Z=Ce^{\nu z} \tag{A.6}$$

$$Z=C\cosh[\nu(h+z)]\,. \tag{A.7}$$

C is an arbitrary constant,

Physically, the azimuth function F should be periodic and hence the functional relationship for F is constant in Equation A.3 and must satisfy,

$$\frac{F''}{F}=-n^2 \tag{A.8}$$

for n an integer. Equation A.8 implies F is proportional to cos[n(φ + α)], given the

symmetry of a cylindrical geometry.

Finally the first term of Equation A.3 becomes

$$R^2\Lambda'' + R\Lambda' + (\nu^2 R^2 - n^2)\Lambda = 0\,. \tag{A.9}$$

This is a Bessel partial differential equation and has a general solution of the form,

$$\Lambda = C_1 J_n(\nu R) + C_2 Y_n(\nu R) \tag{A.10}$$

$J_n(\nu R)$ and $Y_n(\nu R)$ are Bessel functions of the first and second kind respectively. If R assumes the value 0 then $Y_n(\nu R)$ is an unacceptable solution since it is singular at R = 0.

Hence, the characteristic solution of a 3-dimensional fluid under cylindrical coordinate system without any singularity is,

$$\phi = J_n(\nu R) e^{-\nu z} \cos[n(\varphi + \alpha)] \tag{A.11}$$

for infinite water depth, whereas for finite water depth it follows that,

$$\phi = J_n(\nu R) \cosh[\nu(h + z)] \cos[n(\varphi + \alpha)] \tag{A.12}$$

Since $e^{-\nu z}$, $\cosh[\nu(h + z)]$ and $\cos[n(\varphi + \alpha)]$ are not constantly zero on $R = R_0$, it is required that $\partial\phi/\partial R = 0$ is required for the resonant state of a fluid within a cylindrical container.